DOCTORATE THESIS

On the phase-space distribution of heavy particles in turbulence

JAN MEIBOHM

Department of Physics
University of Gothenburg
Göteborg, Sweden 2020

On the phase-space distribution of heavy particles in turbulence
Jan Meibohm

ISBN 978-91-7833-759-0 (PRINT)
ISBN 978-91-7833-758-3 (PDF)

This thesis is electronically published, available at
http://hdl.handle.net/2077/62604
Department of Physics
University of Gothenburg
SE-412 96 Göteborg
Sweden
Telephone: +46 (0)31-786 00 00

Front cover: A initially homogeneous spatial distribution of heavy particles in a random fluid-velocity field, evolved for finite times. The figure shows the spatial particle distribution obtained from 10^7 particles evolved for the (dimensionless) times $\Delta t = t - t_0 = 5, 10, 20$, respectively.

Printed by BrandFactory AB
Göteborg, Sweden 2020

ABSTRACT

Turbulent fluids laden with small, heavy particles are common in nature. Prominent examples of such turbulent suspensions are water droplets in warm clouds, as well as particulate matter or living organisms in the turbulent upper layer of oceans. Because of their inertia, heavy particles tend to distribute inhomogeneously over phase-space, and over configuration space. This phenomenon is referred to as clustering, and it is believed to have a strong impact on the rate of collisions between particles. The collision dynamics, in turn, is crucial for the time evolution of turbulent suspensions, as collisions enable the particles to grow in size.

In this thesis, I study the phase-space distribution of heavy particles in turbulence in terms of a simplified, statistical model that qualitatively captures the particle dynamics on the smallest length scales of turbulence. I use methods from dynamical systems theory, and the theory of large deviations, to describe the long-time behaviour of the particle distribution. In most parts of the thesis, I investigate suspensions of identical particles, and study statistical observables that characterise clustering in phase-space, and in configuration space.

For these ‘mono-disperse’ suspensions I analyse phase-space clustering in a one-dimensional limit by computing the large-deviation statistics of phase-space finite-time Lyapunov exponents, and the phase-space Renyi dimensions. Spatial clustering is studied by projecting the phase-space dynamics to configuration space. I show how the large-deviation statistics of spatial finite-time Lyapunov exponents is affected by this projection, and the effects it has on the spatial correlation dimension.

Finally, I extend the analysis to particle suspensions of two different sizes. I show that this ‘poly-dispersity’ has a strong effect on the phase-space distribution of particles, where it leads to a plateau in the distribution of separations and relative velocities.

LIST OF PAPERS

This thesis consists of an introductory text and the following three appended papers:

Paper A

MEIBOHM, J., PISTONE, L., GUSTAVSSON, K., & MEHLIG, B. 2017 Relative velocities in bidisperse turbulent suspensions. *Physical Review E* **96** (6), 061102(R).

Paper B

MEIBOHM, J.,& MEHLIG, B. 2019 Heavy particles in a persistent random flow with traps. *Physical Review E* **100** (2), 023102.

Paper C

MEIBOHM, J., GUSTAVSSON, K., BEC, J., & MEHLIG, B. 2019 Fractal catastrophes. *to appear in New Journal of Physics, arXiv preprint 1905.08490*

MY CONTRIBUTIONS

My contributions to the appended publications are:

Paper A

I devised and performed the calculations of the one-dimensional statistical model, including the calculation of the correlation dimension. BM and I wrote the paper together.

Paper B

I devised and performed all analytical calculations and computed the statistical model simulations. I wrote the paper, with help of BM.

Paper C

I had the idea for the project, and made all calculations. I wrote the paper, with help of BM.

EARLIER WORK

The following publications were part of my Licentiate thesis [1] and are not included here:

MEIBOHM, J., CANDELIER, F., ROSEN, T., EINARSSON, J., LUNDELL, F. & MEHLIG, B. 2016 Angular velocity of a spheroid log rolling in a simple shear at small Reynolds number. *Physical Review Fluids* **1** (8), 084203.

DUBEY, A., MEIBOHM, J., GUSTAVSSON, K., & MEHLIG, B. 2018 Fractal dimensions and trajectory crossings in correlated random walks. *Physical Review E* **98** (6), 062117.

CONTENTS

I Introduction 1

1 What this thesis is about 2

2 Modelling heavy particles in turbulence 5
2.1 Turbulence 5
2.2 Navier-Stokes equations 7
2.3 Stokes law 8
2.4 Gaussian fluid-velocity fields 10
2.5 Statistical model 13

II Background 19

3 Suspensions of identical particles 19
3.1 Phase-space density 20
3.2 Local phase-space dynamics 23

4 Observables 31
4.1 Phase-space Renyi dimensions 31
4.2 Phase-space (finite-time) Lyapunov exponents 35
4.3 Relations between Renyi dimensions and FTLEs 40

III My work 45

5 Phase-space Renyi dimensions 46
5.1 Phase-space rate function 46
5.2 Renyi dimensions 50
5.3 Implications of the results 54

6 Fractal catastrophes 55
6.1 Spatial density 56
6.2 Projection formula for spatial Renyi dimension 58
6.3 Spatial particle neighbourhoods and their collapse 59
6.4 Neighbourhoods in one spatial dimension 61
6.5 Large deviations of spatial FTLE 63
6.6 Implications of the results and generalisations 65

7 Persistent limit **66**
7.1 Particle trapping 66
7.2 Observables in one spatial dimension 67
7.3 Implications for simulations and experiments 70

8 Suspensions of particles of different sizes **72**
8.1 Bi-disperse particle distribution 72
8.2 Heuristic description of relative dynamics 74
8.3 Model for relative dynamics 75
8.4 Implications for simulations and experiments 81

IV Conclusions and outlook **83**

9 Conclusions **83**

10 Outlook **84**

V Research papers **101**

PART I

INTRODUCTION

Fluids often carry small particles that are much denser than the fluid itself. The air in clouds, for instance, carries large amounts of water, in the form of small water droplets [2, 3, 4]. Furthermore, the water of rivers, lakes and the oceans are full of small impurities, such as particulate soil, but also living organisms [5, 6].

Most fluids are in a state of complicated motion, called turbulence, in which the fluid velocity and pressure fluctuate chaotically as functions of space and time. In fluids with low viscosity, gases in particular, turbulent motion is rather the rule than the exception. The fluid motion accelerates the particles, and enables them to detach from the flow. This detachment is believed to play an important role in cloud physics [2, 3, 4, 7] because it increases the probability of collisions [8, 9, 10, 11, 12, 13] between the water droplets, thus facilitating the formation of rain. The same effect is relevant in the turbulent water of the upper layers of oceans where it is believed to enhance collisions of solid particulate matter, making it stick together and sink as marine snow [14]. Detachment is a result of particle inertia, that arises because the particles are denser (or 'heavier') than the fluid [15, 16, 17].

Mathematically, the dynamics of heavy particles takes place in the higher-dimensional phase space, which consists of both the positions and the velocities of the particles. Viscous friction between the particles and the fluid makes the dynamics dissipative [18, 19, 20] meaning that phase-space volumes of particles must contract over time [17]. This has important implications for the physics of these systems. Dissipation in chaotic dynamics leads to particle aggregation, so-called clustering [17]. Clustering increases the probability of particles to come close together, and thus to interact with each other [8].

1 What this thesis is about

This thesis is concerned with the phase-space distribution of heavy particles in turbulence. Due to clustering, heavy particles tend to distribute inhomogeneously over phase-space so that large regions of phase space are entirely void of particles while other regions show large particle concentration.

For many practical purposes, however, the spatial particle distribution is of interest, too. The reason is that most kinds of particle interactions, collisions [9, 10, 11, 12, 13] for example, require spatial proximity to take place. In order to obtain the spatial particle distribution from the phase-space distribution we must project the phase-space distribution to the lower-dimensional configuration space, the space of positions. This projection has mathematical singularities that lead to interesting and physically relevant effects. We call these singularities caustics [21, 22, 23, 24], because of their similarity with partial focusing of light in optics [25].

Caustics have two important effects. First, they result in divergencies in the spatial probability distribution (density) of particles [17, 22], which is the direct analogue of the diverging light intensity due to partial focusing in optics. Therefore, it is expected that inhomogeneities in the spatial distribution of particles may be even larger than those of the phase-space distribution. Second, caustics allow spatially close particles to approach each other, and thus collide, at high relative velocities [13, 23, 24]. This effect has no direct analogue in optics, but it is not less important. The relative velocity in particle collisions affects collision rates and collision outcomes [8, 9].

The phase-space particle distribution is the main object of study in this thesis, and in the appended research papers. To understand how this distribution evolves as a function of time, I consider a simplified model. This is necessary, since heavy particles in turbulence are a non-linear, multi-scale system, whose general analysis poses formidable challenges [17]. The simplified model is intended to explain the most important physical effects of the particle system. The first main simplification that I employ in this thesis is to mimic the turbulent fluctuations of the fluid velocity, and of the pressure, by a simpler, random fluid-velocity field [17]. Secondly, I assume an effective equation of motion for the particles, known as Stokes law [26, 27]. Stokes law models the force on the particles for a given fluid-velocity field. It neglects the complex back-reaction of the particles onto the fluid, as well as other effects, e.g., due to the finite size of the particles or the history of their motion. The third major simplification that I apply in most of the thesis, is to consider suspensions of identical particles. This approximation is relaxed in the last part of this thesis, when I discuss the relative particle dynamics of suspensions of particles of different sizes [11, 28]. Finally, whenever possible, I reduce the dimensionality of the system to one spatial dimension, and thus to a two-dimensional phase space.

By construction, the models I study are only caricatures, and we do not expect them to quantitatively describe droplets in clouds or algae in the ocean. Their strength is their simplicity, which allows us to mathematically quantify their phase-space dynamics, and, more importantly, to *understand* why they behave the way they do. To assess the value of the models, we must compare their predictions with the results of numerical simulations [11, 28, 29, 30, 31, 32, 33, 34, 35, 36, 37], and with experiments [38, 39, 40, 41, 42, 43, 44, 45].

As I show in this thesis, the mathematical analysis of these 'statistical models' is by no means simple but requires advanced methods of non-equilibrium statistical physics. More importantly, the models explain, albeit their simplicity, important properties of the particle dynamics such as clustering in phase-space and in configuration space, and the formation of caustics [17]. As simplified models do, the statistical models fail sometimes [17]. When and how they fail is of no less interest, as it enables us to critically evaluate our assumptions, and thus to improve our understanding of the physically relevant mechanisms.

Outline

The remainder of my thesis is divided into five parts. You are now reading part one which consists of two chapters, a general introduction and a chapter about the statistical model that I use in the rest of my work. The second part is about the mathematical methods that I employ to study the model. In this part I define the phase-space density of particles (Chapter 3), and explain how to extract measurable numbers, so-called observables from it (Chapter 4). In part three I discuss my own work, and the contents of the papers A-C (Chapters 5-8). In the fourth part I draw conclusions and outline how the studies described in part three could be extended (Chapters 9-10). Part five contains the three research papers A-C.

2 Modelling heavy particles in turbulence

The basis of all further investigations in this thesis is a statistical model [17] for the dynamics of heavy particles in turbulence. This simplified model intends to mimic important aspects of the dynamics of both the turbulent fluid and of the particles, and to combine them in a set of equations of motion. To arrive at the final model in Section 2.5, a number of modelling assumptions are required that I motivate in the first sections of this chapter.

2.1 Turbulence

There is no general definition of turbulence that everybody agrees on. Turbulence does, however have characteristic properties that enable us to distinguish a fluid that is turbulent from one that is not. First of all, turbulence describes the state of a fluid. Hence, it would be wrong to say, “Water is turbulent”, because it can be found in both turbulent and non-turbulent states. What people usually mean when they say that a fluid is turbulent, is that the fluid motion is complicated, and seems unpredictable. This complicated fluid motion is accompanied by excellent mixing properties [46, 47, 48]. Everybody who enjoys milk in their coffee likes to stir after adding the milk, and to let the resulting turbulence complete the work of mixing the two fluids. As a working definition, I will call a fluid turbulent if it is strongly mixing, and moves in a complicated way.

A simple way to think about turbulence is as a composition of eddies of different sizes. When we stir the coffee-milk mixture in our cup, we bring energy into the fluid by generating eddies of the size of the spoon. If we now remove the spoon again and let the fluid move by itself, the larger eddies partly disintegrate and are soon accompanied by smaller eddies of different sizes. The fluid motion acquires a finer and finer spatial structure until it eventually comes to rest.

Scientists call this process a cascade [46, 47, 48] that transports energy from large length scales (size of the spoon) to small scales. A cartoon of this energy cascade is shown in Fig. 2.1. Energy is injected at rate $\epsilon_{\rm in}$ into the large eddies of size ℓ by, for instance, mechanical stirring. Due to fluid-mechanical instabilities [48], larger eddies are unstable and disintegrate into many smaller ones. These smaller eddies, in turn, break up into an even

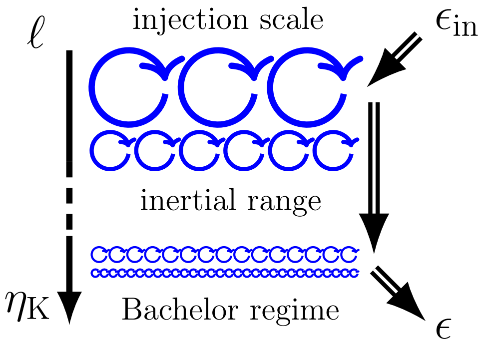

Figure 2.1: Cartoon of the energy cascade in turbulence. The different-size eddies are shown as the blue circles with arrows. Energy is injected into the largest eddies at rate $\epsilon_{\rm in}$ at length scales ℓ, and flows through the inertial range. At the Kolmogorov scale $\eta_{\rm K}$, the energy is dissipated at rate ϵ.

larger number of still smaller ones, and so on. The cascade stops eventually at a small scale $\eta_{\rm K}$, the Kolmogorov scale [49]. Eddies of size $\eta_{\rm K}$ are so small that they dissipate their kinetic energy into heat rather than generating even smaller eddies. We call the rate of energy dissipation ϵ. At scales much smaller than $\eta_{\rm K}$, there is no eddy structure and the fluid-velocity field is spatially smooth. This regime is called the dissipation range or Batchelor regime [50]. Through energy dissipation at the smallest scales, the fluid transforms the energy that we injected at the largest scales in to thermal energy. This explains why the fluid comes to rest after some time when we stop stirring.

If we do not stop stirring, on the other hand, we sustain a non-equilibrium stationary state in which energy is constantly injected at scale ℓ, flows through the energy cascade, and dissipates at scale $\eta_{\rm K}$. In this stationary state, the rate of energy injection must equal the rate of energy dissipation $\epsilon_{\rm in} = \epsilon$. This kind of sustained turbulence is present in clouds [2] where large-scale temperature and pressure gradients constantly feet energy into the large eddies.

An important question is: when does a fluid become turbulent? The answer depends on the typical velocity u_0 of the fluid at the length scale L of the fluid disturbance, and upon the kinematic viscosity ν of the fluid. The kinematic viscosity determines the 'thickness' of a fluid, compared to its density. For most gases and many liquids, the kinematic viscosity ν is small, while it is large for viscous fluids such as honey or tar. From u_0, L and ν, we can define a single dimensionless number

$$\mathrm{Re} = \frac{u_0 L}{\nu}, \tag{2.1}$$

called the Reynolds number. The size of the Reynolds number is an indicator of whether or not the fluid motion is turbulent. If Re is much smaller than unity, $\mathrm{Re} \ll 1$, the fluid is typically not turbulent [26, 27]. Turbulent fluid motion requires Reynolds numbers that are much larger than unity [46, 47, 48]. It is an easy task to estimate the Reynolds number for our coffee cup example. The kinematic viscosity of water is of the order of $\nu \sim 10^{-6}\, m^2/s$. The typical velocity u_0 of stirring is roughly $0.1\, m/s$, and as length scale L we take the diameter of the cup, say $0.1\, m$. Eq. (2.1) then gives the estimate $\mathrm{Re} \approx 10^4$, which is much larger than one. Hence, this simple estimation of the Reynolds number Re makes a strong prediction (turbulence in the coffee cup) that is verified by the result of our (gedanken-)experiment.

2.2 Navier-Stokes equations

The motion of a fluid is described by a fluid-velocity field $\boldsymbol{u}(\boldsymbol{x},t)$ and a pressure field $p(\boldsymbol{x},t)$. The fluid-velocity field $\boldsymbol{u}(\boldsymbol{x},t)$ assigns a velocity vector $\boldsymbol{u}$ to each point $(\boldsymbol{x},t)$ in space and time. Given $\boldsymbol{u}(\boldsymbol{x},t)$, we know how fast and in which direction the fluid moves at position $\boldsymbol{x}$ and at time t. The fluid-velocity field and the pressure field can, in principle, be calculated by solving a set of non-linear differential equations, the Navier-Stokes equations [46, 47, 48]. For an incompressible, Newtonian fluid with $\boldsymbol{\nabla} \cdot \boldsymbol{u}(\boldsymbol{x},t) = 0$ and constant density ρ_f, the Navier-Stokes equations read

$$\rho_\mathrm{f}\{\partial_t \boldsymbol{u}(\boldsymbol{x},t) + [\boldsymbol{u}(\boldsymbol{x},t)\cdot\boldsymbol{\nabla}]\boldsymbol{u}(\boldsymbol{x},t)\} = -\boldsymbol{\nabla} p + \rho_\mathrm{f}\nu\Delta\boldsymbol{u}(\boldsymbol{x},t) + \boldsymbol{f}(\boldsymbol{x},t), \tag{2.2}$$

Equipped with appropriate initial and boundary conditions, the Navier-Stokes equations are believed to describe every aspect of fluid motion, including turbulence.

Equation (2.2) describes the conservation of momentum of a small fluid element. Neighbouring fluid elements collide with each other inelastically, meaning that although momentum is conserved, energy is not. This is a consequence of the viscosity of the fluid, and is described by the viscous term

$\rho_{\rm f}\nu\Delta\boldsymbol{u}(\boldsymbol{x},t)$. The external force density $\boldsymbol{f}(\boldsymbol{x},t)$ corresponds to the stirring on large scales, and thus keeps the fluid in motion.

In order to see how the Reynolds number arises in the Navier-Stokes equations, we de-dimensionalise Eqs. (2.2) according to $t \to (L/u_0)t$, $\boldsymbol{x} \to L\boldsymbol{x}$, $\boldsymbol{u} \to u_0\boldsymbol{u}$, $p \to (\rho_{\rm f}u_0\nu/L)p$ and $\boldsymbol{f} \to (\rho_{\rm f}u_0\nu/L^2)\boldsymbol{f}$. We obtain the dimensionless equation

$$\mathrm{Re}\{\partial_t\boldsymbol{u}(\boldsymbol{x},t)+[\boldsymbol{u}(\boldsymbol{x},t)\cdot\boldsymbol{\nabla}]\boldsymbol{u}(\boldsymbol{x},t)\}=-\boldsymbol{\nabla}p+\Delta\boldsymbol{u}(\boldsymbol{x},t)+\boldsymbol{f}(\boldsymbol{x},t)\,. \qquad (2.3)$$

The Reynolds number appears of the left-hand side of Eq. (2.3). It controls the size of the inertial terms $\partial_t\boldsymbol{u}(\boldsymbol{x},t)+[\boldsymbol{u}(\boldsymbol{x},t)\cdot\boldsymbol{\nabla}]\boldsymbol{u}(\boldsymbol{x},t)$. These terms, in particular the non-linear term $[\boldsymbol{u}(\boldsymbol{x},t)\cdot\boldsymbol{\nabla}]\boldsymbol{u}(\boldsymbol{x},t)$, are responsible for the interaction between different-sized eddies in the fluid, and thus for its turbulent motion. When the Reynolds number is small enough, one can neglect the left-hand side of Eq. (2.3), so that the fluid motion is not turbulent. For $\mathrm{Re}\gg 1$ the non-linearity in the equations leads to chaotic fluctuations of the solutions in space and time.

2.3 Stokes law

Heavy particles immersed in the turbulent fluid are the central objects of our study. The turbulent motion of the fluid leads to forces that accelerate the particles. The correct way of calculating these forces is to solve the Navier-Stokes equation with appropriate (no-slip) boundary conditions on the particle surface. Even on today's largest computers this is in general impractical for suspensions of many particles. In our model, we simplify the problem drastically by using a solution of Eqs. (2.2) that is valid only in a strict, limiting case. The price we pay is that the corresponding effective equation for the forces on the particles is valid only under strong assumptions on the particle shape, size, density and velocity. The effective equation we use is called Stokes law [26, 27]. For a spherical particle of radius a it gives the force

$$\boldsymbol{F}=6\pi\nu\rho_{\rm f}a\,[\boldsymbol{u}(\boldsymbol{x}_t,t)-\boldsymbol{v}_t]\,. \qquad (2.4)$$

Here $\rho_{\rm f}$ is the density of the fluid and ν its kinematic viscosity. The fluid-velocity field $\boldsymbol{u}(\boldsymbol{x}_t,t)$ is that of the undisturbed fluid evaluated at the position $\boldsymbol{x}_t$ of the particle. Water droplets in turbulent clouds or particulate matter in the ocean are subject to not only forces from the turbulent fluid, but also gravitational forces that cause the particles to settle. In particular for the larger particles, the relative settling speed compared to smaller particles is believed to be a main driving force for particle collisions [2, 8]. We neglect these contributions in our model which can be justified in regions of intense turbulence, where settling is negligible.

Stokes law (2.4) is derived from the so-called Stokes equation [26, 27] which neglects the left-hand side of Eqs. (2.2), and which is valid when the fluid disturbance caused by the particle can be disregarded. Therefore, corrections to Eq. (2.4) may arise when either of the two inertia terms $\partial_t \boldsymbol{u}$ (unsteady fluid inertia) and $(\boldsymbol{u}\cdot\nabla)\boldsymbol{u}$ (convective fluid inertia) are of the same order as the terms on right-hand side of Eqs. (2.2). In order for Stokes law to be a valid approximation of the particle dynamics, we require that the particle is small, so that $a \ll \eta_{\rm K}$, and that the particle Reynolds number ${\rm Re}_{\rm p} = u_0 a/\nu$ is much smaller than unity. Here, u_0 is the typical relative ('slip') velocity [26, 27] between the particle and the fluid [17]. Furthermore, the density ratio $\rho_{\rm p}/\rho_{\rm f}$ must be large, so that buoyancy effects can be neglected. This is why, for our model, we need to assume that the particles are heavy.

Eq. (2.4) is a so-called one-way coupling [51], which means that the fluid motion is modelled to act upon the particle, but not the other way round. This means in particular that when we consider suspensions of many particles in the same fluid, hydrodynamical interactions are neglected. This assumption requires that the suspensions that we consider are dilute.

For clouds, the radii of the droplets are of the order of $a \approx 10^{-6}m$, and the Kolmogorov length scale is about a millimeter $\eta_{\rm K}$, so that $a \ll \eta_{\rm K}$ [2]. The density ratio of water to air is about one thousand $\rho_{\rm p}/\rho_{\rm f} \approx 10^3$, and thus much larger than one. The density of droplets is about 10^8 per cubic meter [2], so there is on average less than one droplet per $\eta_{\rm K}^3$. This would suggest that the use of Stokes law is a good approximation for raindrops in clouds, as long as individual droplet pairs do not come too close and the particle Reynolds number ${\rm Re}_{\rm p}$ stays small.

Stokes law leads to the following equation for the velocity $\boldsymbol{v}_t$ for a particle of mass $m_{\rm p}$

$$\tfrac{\rm d}{{\rm d}t}\boldsymbol{v}_t = \boldsymbol{F}/m_{\rm p} = \gamma[\boldsymbol{u}(\boldsymbol{x}_t,t)-\boldsymbol{v}_t]\,. \tag{2.5}$$

From Eq. (2.4) the damping coefficient γ is given by $\gamma = 9\nu\rho_{\rm f}/(2\rho_{\rm p}a^2)$. For a steady fluid-velocity field $\boldsymbol{u}(\boldsymbol{x},t) = \boldsymbol{u}$, Eq. (2.5) has the solution $\boldsymbol{v}_t = \boldsymbol{u} +$

$e^{-\gamma t}\boldsymbol{v}_{t=0}$. Hence, Stokes law describes an exponential relaxation of the particle velocity to the fluid velocity $\boldsymbol{u}$. The characteristic damping time γ^{-1} is also called 'Stokes time', and it is denoted by $\tau_{\rm p}$.

2.4 Gaussian fluid-velocity fields

The use of Stokes law (2.4) for the force on a particle requires a spatially smooth fluid-velocity field $\boldsymbol{u}(\boldsymbol{x},t)$. In turbulence, $\boldsymbol{u}(\boldsymbol{x},t)$ is smooth up to scales of about ten times the Kolmogorov length scale $\eta_{\rm K}$ [17]. Particles that are much smaller than $\eta_{\rm K}$ are advected by the larger eddies, so that, as far as the particle dynamics is concerned, we expect only the turbulent fluctuations of $\boldsymbol{u}(\boldsymbol{x},t)$ at scales of the order of $\eta_{\rm K}$ to matter [17].

The transport of energy through the inertial range destroys most of the information contained in the forcing (or stirring) that excites the turbulence [47]. When the turbulence is strong, this implies that we can assume the statistics of the fluid-velocity field in at scales of the order of $\eta_{\rm K}$ and below to be statistically homogeneous and isotropic [47]. Furthermore, under steady forcing, turbulence reaches a non-equilibrium steady state, so that $\boldsymbol{u}(\boldsymbol{x},t)$ is statistically homogeneous in time.

The statistical properties of homogenous and isotropic turbulence on small scales put strong constraints on the mean and the correlation function of $\boldsymbol{u}(\boldsymbol{x},t)$. We mimic these statistical properties of turbulence with a Gaussian fluid-velocity field. The underlying assumption is that the most important aspect of the turbulent flow $\boldsymbol{u}(\boldsymbol{x},t)$ for the particle dynamics are the correlation functions $\langle u_i(\boldsymbol{x},t)u_j(\boldsymbol{x}',t')\rangle$, and, in particular, the spatial smoothness of the turbulent fluid-velocity field on small scales. That $\boldsymbol{u}(\boldsymbol{x},t)$ is turbulent, and a solution to Eqs. (2.2), is disregarded.

A particularly simple choice of random flow is to model $\boldsymbol{u}(\boldsymbol{x},t)$ by a spatially smooth, Gaussian random function. Gaussian random functions have the advantage that their mean and correlation function determine all higher moments. For instance, for a Gaussian distributed field $\boldsymbol{u}(\boldsymbol{x},t)$ with zero mean, all odd moments vanish. The higher even moments are expressed in terms of sums over correlation functions using Wick's rule [47, 52]. In turbulence, the statistics of $\boldsymbol{u}(\boldsymbol{x},t)$ can be shown to have non-Gaussian tails at small scales [47]. The reason is that the Navier-Stokes equations give rise to intermittent outbursts of strong fluctuations that do not appear in a Gaussian model. We neglect these intermittency effects.

We generate the random fluid-velocity field $\boldsymbol{u}(\boldsymbol{x},t)$ from Gaussian random potentials. Although the turbulence in rain clouds or the oceans is incompressible, the fluid-velocity fields experienced by, for instance, particles floating on the surfaces of fluids may be compressible [53, 54]. Therefore, we allow for compressibility of the fluid-velocity field $\boldsymbol{u}(\boldsymbol{x},t)$ in our model. To this end, it is convenient to separate the fluid-velocity field $\boldsymbol{u}(\boldsymbol{x},t)$ into a solenoidal and a potential part. The solenoidal part is incompressible and is generated from a tensor potential. In d dimensions, the tensor potential is an antisymmetric tensor field of rank $d-2$ and, hence, a vector potential $\boldsymbol{A}(\boldsymbol{x},t)$ in $d=3$, a scalar potential $\psi(\boldsymbol{x},t)$ in $d=2$ and zero in $d=1$. The potential part of the random flow $\boldsymbol{u}(\boldsymbol{x},t)$ is compressible but rotation-free, and it is the gradient of a scalar potential $\phi(\boldsymbol{x},t)$. The flow field $\boldsymbol{u}(\boldsymbol{x},t)$ in $d=1,2,3$ reads in terms of the tensor and scalar potentials [17]

$$u(x,t)=\partial_x\phi(\boldsymbol{x},t), \tag{2.6a}$$

$$\boldsymbol{u}(\boldsymbol{x},t)=\big(1-\wp\big)^{1/2}\begin{pmatrix}\partial_x\psi(\boldsymbol{x},t),\\ -\partial_y\psi(\boldsymbol{x},t)\end{pmatrix}+\wp^{1/2}\begin{pmatrix}\partial_x\phi(\boldsymbol{x},t)\\ \partial_y\phi(\boldsymbol{x},t)\end{pmatrix}, \tag{2.6b}$$

$$\boldsymbol{u}(\boldsymbol{x},t)=\left(\frac{1-\wp}{2}\right)^{1/2}\boldsymbol{\nabla}\times\boldsymbol{A}(\boldsymbol{x},t)+\wp^{1/2}\boldsymbol{\nabla}\phi(\boldsymbol{x},t). \tag{2.6c}$$

In Eqs. (2.6), the solenoidal part of $\boldsymbol{u}(\boldsymbol{x},t)$ is generated by the vector potential $\boldsymbol{A}(\boldsymbol{x},t)$ in $d=3$, and by the scalar potential $\psi(\boldsymbol{x},t)$ in $d=2$. The potential part of $\boldsymbol{u}(\boldsymbol{x},t)$ is the gradient of a scalar potential, which we denote by $\phi(\boldsymbol{x},t)$. The relative magnitude of the solenoidal and potential parts of $\boldsymbol{u}(\boldsymbol{x},t)$ is determined by the compressibility degree $\wp$ [55]. Hence, $\boldsymbol{u}(\boldsymbol{x},t)$ is incompressible (solenoidal) for $\wp=0$, and fully compressible (potential) for $\wp=1$. In $d=1$, the flow field $\boldsymbol{u}(\boldsymbol{x},t)$ is scalar and thus always fully compressible. We take all individual components of the potential fields $\boldsymbol{A}(\boldsymbol{x},t)$, $\psi(\boldsymbol{x},t)$ and $\phi(x,t)$ to be statistically independent functions with zero mean and with identical correlation functions given by [17]

$$C(\boldsymbol{x},t;\boldsymbol{x}',t')=\frac{u_0^2\eta^2}{d}\exp\big(-|\boldsymbol{x}-\boldsymbol{x}'|^2/(2\eta^2)-|t-t'|/\tau_{\rm c}\big). \tag{2.7}$$

The parameters η and $\tau_{\rm c}$ are the correlation length and the correlation time, respectively, while u_0 determines the typical velocity of the fluid at the small scales. The correlation function (2.7) is stationary in time, as well as homogeneous, isotropic and smooth in space. This ensures that by Eq. (2.6), also the correlation function of $\boldsymbol{u}(\boldsymbol{x},t)$ has the desired statistical properties.

In numerical simulations, we equip the Gaussian random potentials with periodic boundary conditions in a box of edge length $L=10\eta$. The potentials can then be expressed as independent Fourier sums of the form

$$\frac{u_0\eta}{\sqrt{d}}\left(\frac{\sqrt{2\pi}}{L}\right)^{d/2}\sum_{\boldsymbol{k}} c_{\boldsymbol{k}}(t)\exp[i\boldsymbol{k}\cdot\boldsymbol{x}-k^2\eta^2/4]. \tag{2.8}$$

The sum is taken over the wave vectors $\boldsymbol{k}=(2\pi/L)\boldsymbol{n}$ with $\boldsymbol{n}\in\mathbb{Z}^d$ with Fourier components $c_{\boldsymbol{k}}$. The latter are independent, complex-valued Ornstein-Uhlenbeck processes, with zero mean and correlations [17, 56]

$$\langle c_{\boldsymbol{k}}(t)\bar{c}_{\boldsymbol{k}'}(t')\rangle=\delta_{\boldsymbol{k}\boldsymbol{k}'}\exp(-|t-t'|/\tau_{\mathrm{c}}). \tag{2.9}$$

We take independent Ornstein-Uhlenbeck processes for $c_{\boldsymbol{k}}$, because they are the simplest stationary Gaussian processes with finite correlation time [52]. The exponential time correlation in Eq. (2.9) leads to the exponential time correlation (2.7) of the random potentials. Since the smooth regime in turbulence extends to about ten times η_{K}, and because $\boldsymbol{u}(\boldsymbol{x},t)$ is smooth over the periodic box of length $L=10\eta$, we take the correlation length η to be of the order of η_{K}.

For $|\boldsymbol{x}-\boldsymbol{x}'|\ll\eta$, the Gaussian, random fluid-velocity field $\boldsymbol{u}(\boldsymbol{x},t)$ then has the correlation

$$\langle u_i(\boldsymbol{x},t)u_j(\boldsymbol{x}',t')\rangle\sim\frac{u_0^2}{d}\left[\delta_{ij}-K_{ij}\left(\boldsymbol{x}-\boldsymbol{x}'\right)\right]\exp\left(-|t-t'|/\tau_c\right), \tag{2.10}$$

where tensor $K_{ij}(\boldsymbol{x})$ in Eq. (2.10) reads

$$K_{ij}(\boldsymbol{x})=\left(\frac{d+1-2\wp}{d-1}\right)\frac{x^2}{2\eta^2}\delta_{ij}+\left(\frac{\wp d-1}{d-1}\right)\frac{x_ix_j}{\eta^2}. \tag{2.11}$$

The equations for the correlation functions (2.10) and (2.11) are valid for general dimension d. A little care must be taken when considering the case $d=1$. As one-dimensional flows are always fully compressible, one must first take the limit $\wp\to1$ before setting the dimensionality to unity.

2.5 Statistical model

We have now collected all the ingredients we need to put together the statistical model for heavy particles in turbulence. As the last step I replace the turbulent fluid-velocity field in Eq. (2.5) with our Gaussian model for $\boldsymbol{u}(\boldsymbol{x},t)$, and add the equation $\frac{\mathrm{d}}{\mathrm{d}t}\boldsymbol{x}_t = \boldsymbol{v}_t$ for the particle position. The equations of motion for a single particle at position $\boldsymbol{x}_t$ and with velocity $\boldsymbol{v}_t$ then read

$$\frac{\mathrm{d}}{\mathrm{d}t}\boldsymbol{x}_t = \boldsymbol{v}_t\,, \qquad \frac{\mathrm{d}}{\mathrm{d}t}\boldsymbol{v}_t = \gamma\,[\boldsymbol{u}(\boldsymbol{x}_t,t) - \boldsymbol{v}_t]\,. \tag{2.12}$$

Equations (2.12) complete the statistical model. Because the random fluid-velocity field $\boldsymbol{u}(\boldsymbol{x},t)$ is a non-linear function of $\boldsymbol{x}$, the equations of motion (2.12) are non-linear. The motion of the particles is therefore potentially chaotic, even though $\boldsymbol{u}(\boldsymbol{x},t)$ is not a turbulent solution to Eqs. (2.2).

In their present form, Eqs. (2.12) are dimensional. Different dimensionless formulations are convenient to better understand the behaviour of the dynamics in limiting cases. I describe the dimensionless parameters that are characteristic for the dynamics of the statistical model in the next section.

2.5.1 Dimensionless parameters

In systems that depend on several dimensional parameters, it is often convenient to construct dimensionless numbers that control the dynamics. The use of dimensionless coordinates reduces the number of quantities that need to be considered, and it reflects a kind of universality of the dynamics. That is, for all combinations of dimensional parameters that lead to the same dimensionless numbers, the statistical model should behave in the same way. We have already observed this for the Navier-Stokes equations, where the Reynolds number is the characteristic dimensionless number.

For the statistical model, the particle equations of motion (2.12) depend on a single time scale, the Stokes time $\tau_{\mathrm{p}} = \gamma^{-1}$, as mentioned in Section 2.3. Additionally, the random flow $\boldsymbol{u}(\boldsymbol{x},t)$ depends on one dimensionless parameter, the compressibility $\wp$, and three dimensional parameters: the correlation length η, the root-mean-square velocity u_0 and the correlation time τ_{c}. From η and u_0 we can construct another time scale, $\tau_{\mathrm{a}} = \eta/u_0$ which we call the advection time. The advection time τ_{a} is the typical time a fluid element takes to travel by one correlation length η. The statistical model therefore has three characteristic time scales, τ_{p}, τ_{c} and τ_{a}, and one characteristic length scale η. From the three time scales we can form three different dimensionless numbers, two of which are independent. We have

$$\mathrm{St} = \frac{\tau_\mathrm{p}}{\tau_\mathrm{c}}, \qquad \mathrm{Ku} = \frac{\tau_\mathrm{c}}{\tau_\mathrm{a}}, \qquad K = \frac{\tau_\mathrm{p}}{\tau_\mathrm{a}}. \tag{2.13}$$

The first dimensionless parameter, St, is called the Stokes number. It is the ratio of the particle relaxation time τ_p and the flow correlation time τ_c. Hence, it is a measure of the importance of particle inertia. The Kubo number, Ku, is the ratio of the two fluid time scales τ_c and τ_a, and a measure for the persistence of the flow. K is another inertia parameter, which measures how different the particle dynamics is from the dynamics of a fluid element. For historical reasons, K is the analogue of the Stokes number for particles in the turbulence literature. In turbulence, the only microscopic fluid time scale is the analogue of τ_a, the Kolmogorov time scale $\tau_\mathrm{K} = \sqrt{\nu/\epsilon}$. Hence, the only inertia parameter is $\tau_\mathrm{p}/\tau_\mathrm{K}$, called the Stokes number in the turbulence literature [17].

The three dimensionless parameters in Eq. (2.13) are not independent, but connected by the relation $\mathrm{St}\,\mathrm{Ku} = K$. This shows that, in fact, the statistical model depends on only two dimensionless numbers. Most frequently Ku and St are taken as the independent parameters [17]. When comparing to the results of the statistical model to numerical simulations of turbulence, on the other hand, one must consider the case $\tau_\mathrm{c} \gg \tau_\mathrm{a}$ so that the relevant parameter is K [17].

Let us now see how the dimensionless parameters in Eq. (2.13) enter the equations of motion. This depends on the way we de-dimensionalise the equations of motion (2.12) of the statistical model. I focus here on one particular de-dimensionalisation scheme and refer to Ref. [17] for a different one. The scheme I use in this thesis is

$$t \to \tau_\mathrm{p} t\,, \quad \boldsymbol{x}_t \to \eta \boldsymbol{x}_t\,, \quad \boldsymbol{v}_t \to \eta \tau_\mathrm{p}^{-1} \boldsymbol{v}_t, \quad \boldsymbol{u} \to \eta \tau_\mathrm{p}^{-1} \boldsymbol{u}\,. \tag{2.14}$$

Note that all variables on the right-hand sides of the arrows in Eq. (2.14) are dimensionless. In terms of these dimensionless variables the equations of motion (2.12) are parameter-free:

$$\tfrac{\mathrm{d}}{\mathrm{d}t} \boldsymbol{x}_t = \boldsymbol{v}_t\,, \qquad \tfrac{\mathrm{d}}{\mathrm{d}t} \boldsymbol{v}_t = \boldsymbol{u}(\boldsymbol{x}_t, t) - \boldsymbol{v}_t\,. \tag{2.15}$$

The dependence on the parameters Ku and St is contained in the flow correlation functions. The correlation function (2.7) of the de-dimensionalised potentials reads

$$C(\boldsymbol{x},t;\boldsymbol{x}',t') = \frac{\mathrm{Ku}^2\mathrm{St}^2}{d}\exp\big(-|\boldsymbol{x}-\boldsymbol{x}'|^2/2-\mathrm{St}|t-t'|\big)\,. \tag{2.16}$$

Accordingly, the correlation function for the dimensionless random flow $\boldsymbol{u}(\boldsymbol{x},t)$ is now given by

$$\langle u_i(\boldsymbol{x},t)u_j(\boldsymbol{x}',t')\rangle \sim \frac{\mathrm{Ku}^2\mathrm{St}^2}{d}\big[\delta_{ij}-K_{ij}\big(\boldsymbol{x}-\boldsymbol{x}'\big)\big]\exp\big(-\mathrm{St}|t-t'|\big)\,, \tag{2.17}$$

for $|\boldsymbol{x}-\boldsymbol{x}'|\ll 1$, with dimensionless $K_{ij}(\boldsymbol{x})$ given by

$$K_{ij}(\boldsymbol{x}) = \left(\frac{d+1-2\wp}{d-1}\right)\frac{x^2}{2}\delta_{ij} + \left(\frac{\wp d-1}{d-1}\right)x_i x_j\,. \tag{2.18}$$

Because of the inter-relation between the dimensionless numbers (2.13) one can, instead of expressing the equations in terms of Ku and St, use K together with either Ku or St. Fig. 2.2 shows a sketch of the Ku-St parameter space [17]. For fixed $\wp$, any combination of (Ku, St) defines a point in the plane and thus a different behaviour of the statistical model. The dimensionless numbers (2.13) are useful for constructing limiting cases, or for using perturbation theory [17] when one or both of the parameters are small. In the next two sections, I present two limiting cases of Ku and St in which the dynamics can be simplified. These limits are the white-noise limit and the persistent limit.

2.5.2 White-noise limit

In the so-called white-noise limit the fluid velocity field $\boldsymbol{u}(\boldsymbol{x},t)$ turns into a white-noise signal. This allows to use diffusion approximations for the equations of motion (2.15). The white-noise limit requires a separation between the time scales in which the Stokes time τ_p is the largest of all time scales, and the advection time τ_a is much larger than the correlation time τ_c, so that $\tau_\mathrm{p} \gg \tau_\mathrm{a} \gg \tau_\mathrm{c}$. In other words, the white-noise limit describes the dynamics of very heavy particles (τ_p is large) in a quickly fluctuating velocity field (τ_a and τ_c are small). In terms of Ku and St, the white-noise limit amounts to taking the following limit:

$$\mathrm{Ku}\to 0\,,\qquad \mathrm{St}\to\infty\,,\quad \text{so that}\quad \mathrm{Ku}^2\,\mathrm{St} = \text{constant}\,. \tag{2.19}$$

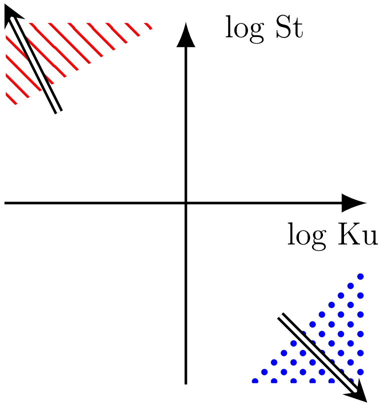

Figure 2.2: Sketch of the Ku-St parameter space. The red lines show the regime close to the white-noise limit. The blue dotted region is the regime close to the persistent limit. The double arrows indicate the direction along which the limits are approached.

In this limit, the time dependence in the correlation function (2.17) of $\boldsymbol{u}(\boldsymbol{x},t)$ tends to a delta function. To see this, we observe that

$$\lim_{\mathrm{St}\to\infty} \mathrm{St}\exp\big(-\mathrm{St}|t-t'|\big) = 2\delta(t-t')\,. \tag{2.20}$$

The constant in Eq. (2.19) can take any value. It determines the relative magnitude of St and Ku^{-2} when the limit is taken. We call this constant the 'white-noise parameter' ε, and define it as

$$\varepsilon^2 = \frac{\mathrm{Ku}^2\mathrm{St}}{d}\big(1+2\wp\big)\,. \tag{2.21}$$

This choice for ε in terms of Ku and St is convenient, since it makes the radial diffusion constant for the separation of particles identical to ε^2 [17]. The white-noise parameter ε is the inertia parameter in the white-noise limit, because it plays a similar role as the Stokes number when St and Ku are finite [17]. In Fig. 2.2 the regime where the dynamics can be approximated by the white-noise limit is shown by the red lines. The direction of approach of the white-noise limit, Eq. (2.19), is shown by the arrow.

The white-noise limit is convenient for analytical computations because the particle motion becomes a diffusion process. This allows to express the particle phase-space density as a solution of a Fokker-Planck equation. A second important simplification is that the single-particle dynamics decouples from the relative dynamics of several particles.

2.5.3 Persistent limit

Similarly to the white-noise limit, the persistent limit requires a separation of time scales. In the persistent limit, however, the correlation time is the *largest* of all time scales. The flow fields $\boldsymbol{u}(\boldsymbol{x},t)$ becomes persistent, compared to the dynamics of fluid elements and the dynamics of the particles. We require $\tau_\mathrm{c} \gg \tau_\mathrm{a}, \tau_\mathrm{p}$, where the ratio of τ_a and τ_p can take any value. In a sense, the persistent limit is opposite to the white-noise limit, where τ_c is the smallest of all time scales. The persistent limit describes inertial particles in a very persistent flow, and is obtained by letting

$$\mathrm{Ku} \to \infty\,, \qquad \mathrm{St} \to 0\,, \quad \text{so that} \quad K = \text{constant}\,. \tag{2.22}$$

The vicinity of this limit is shown as the blue, dotted region in Fig. 2.2, the arrow indicates the direction in which the persistent limit is approached. In the persistent limit, the correlation function (2.17) of the fluid-velocity field loses its time dependence, since

$$\lim_{\mathrm{St}\to 0} \exp\big(-\mathrm{St}|t-t'|\big) = 1\,. \tag{2.23}$$

This means that the flow field $\boldsymbol{u}(\boldsymbol{x},t)$ is constant in a fixed frame of reference, compared to particle dynamics, and to the dynamics of fluid elements. Therefore, we can approximate $\boldsymbol{u}(\boldsymbol{x},t)$ as stationary [57], $\boldsymbol{u}(\boldsymbol{x},t) \approx \boldsymbol{u}(\boldsymbol{x})$ for a single realisation. The inertial particles do, however, still move through the flow, and experience a changing fluid field $\boldsymbol{u}(\boldsymbol{x}_t)$ along their paths.

We denote the inertia parameter in the persistent limit as κ. The latter is typically defined in terms of the fluid-velocity gradient matrix $\mathbb{A}(\boldsymbol{x},t)$ with components $A_{ij} = \partial u_i(\boldsymbol{x},t)/\partial x_j$. In terms of Ku and St, we choose κ as [17]

$$\kappa^2 = \mathrm{Tr}\big\langle \mathbb{A}(\boldsymbol{x},t)\mathbb{A}(\boldsymbol{x},t)^\mathsf{T} \big\rangle = (d+2)\mathrm{Ku}^2\mathrm{St}^2\,. \tag{2.24}$$

The particle dynamics in the persistent limit becomes particularly simple when the flow field $\boldsymbol{u}(\boldsymbol{x},t)$ is sufficiently compressible. In this case, the particles are trapped in compressible flow regions for times $\approx \tau_\mathrm{c}$. I discuss this in more detail in Chapter 7, and in Paper B.

I close this chapter by briefly summarising and discussing the main points. I introduced the statistical model for heavy particles in turbulence, the topic of this work. The model mimics the particle dynamics of heavy particles in turbulence at the smallest scales. It is intended to be as simple as possible, but to still grasp the most important aspects of the particle dynamics. The arguably most drastic simplification is to replace the turbulent fluctuations by a Gaussian velocity field $\boldsymbol{u}(\boldsymbol{x}, t)$ with appropriate correlation functions (2.10). This Gaussian model neglects some characteristic aspects of actual turbulence, such as intermittency, as I mentioned in Section 2.4. Another important fact that we neglect is the dissipative nature of the Navier-Stokes equations, which leads to the time-irreversible stretching of vortices [48], and makes any solution of the Navier-Stokes equations (2.2) asymmetric under time-reversal. The Gaussian fluid-velocity field that we use in the model, on the other hand, is time-reversal symmetric [17, 58].

The great asset of the model is its simplicity, which makes the problem mathematically tractable, and even allows for analytical results in the white-noise limit and in the persistent limit. As I show in the next part of this thesis, however, the analysis of the model is by no means simple, and requires a wide range of tools from theoretical physics.

PART II
BACKGROUND

In the second part of my thesis, I describe the methods used to study the statistical model. These methods are required to analyse suspensions of many particles that are immersed in the same fluid-velocity field $\boldsymbol{u}(\boldsymbol{x},t)$. At this stage, we consider suspensions of identical particles. This assumption is relaxed in later, in Chapter 8.

The second part of the thesis is organised as follows. In Chapter 3, I define the phase-space (probability) density of particles, the main object of our further studies. This density is a function of the realisation of the random fluid-velocity field $\boldsymbol{u}(\boldsymbol{x},t)$. In Chapter 4, I explain how we extract fixed quantities, so called observables, from this density, by taking ensemble averages over realisations of $\boldsymbol{u}(\boldsymbol{x},t)$, or by averaging over long times.

3 Suspensions of identical particles

Physical systems such as water droplets in turbulent clouds, sprays, or fine dust in combustion engines contain not just a single particle, but typically a large number of them. In this chapter, I explain how we study suspensions of identical heavy particles, in which all particles have the same Stokes number. Suspensions of identical particles, so called ‘mono-disperse’ suspensions, are, of course, an idealisation. Particle suspensions in nature typically contain particles of a range of different sizes, which makes their study more complicated. The study of mono-disperse suspensions is, however, an important first step towards the modelling of more realistic systems. In order to study these systems mathematically I introduce here some methods and quantities that I refer to in Chapters 5-8.

In a dilute suspension of identical particles, we can assume that all individual particles obey the single-particle equations of motion (2.15), which I restate here in the dimensionless form

$$\frac{\mathrm{d}}{\mathrm{d}t}\big(\boldsymbol{x}_t,\boldsymbol{v}_t\big)=\boldsymbol{F}_t(\boldsymbol{x}_t,\boldsymbol{v}_t)\,,\quad \boldsymbol{F}_t(\boldsymbol{x},\boldsymbol{v})=\big(\boldsymbol{v},\boldsymbol{u}[\boldsymbol{x},t]-\boldsymbol{v}\big)\,. \tag{3.1}$$

I call $\boldsymbol{F}_t(\boldsymbol{x},\boldsymbol{v})$ the phase-space velocity field. It is a smooth function of the phase-space coordinates, so that Eq. (3.1) has a unique solution for a given (smooth) realisation $\boldsymbol{u}(\boldsymbol{x},t)$ and for a given set of initial conditions $(\boldsymbol{x}_{t_0},\boldsymbol{v}_{t_0})$ at initial time t_0. In other words, the trajectories of particles do not cross in phase space.

3.1 Phase-space density

Globally, the dynamics of Eq. (3.1) is described by the time evolution of the phase-space probability distribution (or density) $\varrho_{t,t_0}(\boldsymbol{x},\boldsymbol{v})$ of particles. The phase-space probability density determines the probability of finding a particle at $(\boldsymbol{x},\boldsymbol{v})$ at time t. As the number of particles is conserved, the density must be normalised,

$$\int_V \mathrm{d}\boldsymbol{x}\mathrm{d}\boldsymbol{v}\,\varrho_{t,t_0}(\boldsymbol{x},\boldsymbol{v})=1\,. \tag{3.2}$$

Here V denotes the entire of phase space, which we assume to be bounded, so that its total volume $\mathscr{V}=\mathrm{Vol}(V)<\infty$, is finite. At time t_0, we take as the initial condition for ϱ_{t,t_0} a homogeneous particle distribution in phase-space $\varrho_{t_0,t_0}(\boldsymbol{x},\boldsymbol{v})=1/\mathscr{V}$. Using the equations of motion (3.1), we can calculate ϱ_{t,t_0} numerically by evolving a fine grid of initial trajectories at time t_0, sampled from the initially homogeneous density, to time $t>t_0$. Figure 3.1 shows a snapshot of the particle density ϱ_{t,t_0} in $d=1$ at different $\Delta t=t-t_0$ in two-dimensional phase space. Fig. 3.1(a), (b) and (c) correspond to $\Delta t=1$, 3 and 5, respectively. The darker red colours in the figure correspond to regions where the phase-space density is larger. White regions correspond to low particle density. The colour coding is logarithmic to improve visibility. Already at $\Delta t=1$ [Fig. 3.1(a)], we observe that ϱ_{t,t_0} is inhomogeneous. As Δt increases [Figs. 3.1(b) and (c)], the density is concentrated onto a smaller and smaller subset of the phase space. The region where the particle density is non-zero attains a thin and curved shape.

This phenomenon is known as phase-space clustering [17]. The phase-space volume occupied by the particles decreases as a function of time, as a

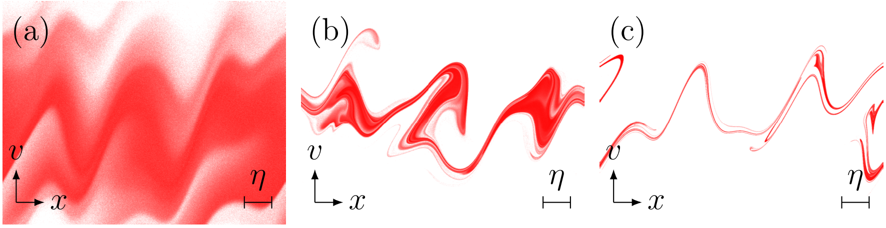

Figure 3.1: Evolution of the phase-space particle density ϱ_{t,t_0} for the one-dimension statistical model from a uniform distribution at finite times $\Delta t = t - t_0$. The particle density is simulated in the white-noise limit with $\varepsilon = 1.5$ using 10^7 particles. The position is plotted horizontally, the velocity vertically. The logarithmic colour coding shows the magnitude of ϱ_{t,t_0}. (a) $\Delta t = 1$. (b) $\Delta t = 3$. (c) $\Delta t = 5$.

consequence of the dissipative dynamics. Because the phase-space velocity field $\boldsymbol{F}_t(\boldsymbol{x},\boldsymbol{v})$ is compressible, $\operatorname{div} \boldsymbol{F}_t(\boldsymbol{x},\boldsymbol{v}) = -d$, the phase-space volume of particles decreases exponentially [59]

$$\mathscr{V}_t = \mathscr{V}_{t_0} \mathrm{e}^{-d(t-t_0)} . \tag{3.3}$$

For finite Δt, the phase-space contraction leads to a transient state, in which the phase-space volume approaches zero. The phase-space density ϱ_{t,t_0} within the volume $\mathscr{V}_t$, on the other hand, must diverge, due to the normalisation condition (3.2).

We define the infinite-time density $\bar{\varrho}_t(\boldsymbol{x},\boldsymbol{v})$ by taking the limit

$$\bar{\varrho}_t(\boldsymbol{x},\boldsymbol{v}) = \lim_{t_0 \to -\infty} \varrho_{t,t_0}(\boldsymbol{x},\boldsymbol{v}) . \tag{3.4}$$

The density $\bar{\varrho}_t(\boldsymbol{x},\boldsymbol{v})$ corresponds to the evolution of an initially uniform density in the infinite past, to finite time t. Fig. 3.2(a) shows ϱ_{t,t_0} for $\Delta t = 50$, and thus an approximation of $\bar{\varrho}_t$. The magnifications in Fig. 3.2(b) and (c) show that for large Δt, $\bar{\varrho}_t$ acquires a filamentary, small-scale structure. The filamentary structure structure extends to scales much smaller than the correlation length $\eta = 1$ of the fluid-velocity field $\boldsymbol{u}(\boldsymbol{x},t)$.

The set that particles approach in the long-time limit is called an ‘attractor’. In principle, attractors can be any subset of the phase-space. They can be points, lines or (hyper-surfaces), but also more complicated sets with fractal properties, sometimes called ‘strange attractors’ [18, 19, 20]. For our system,

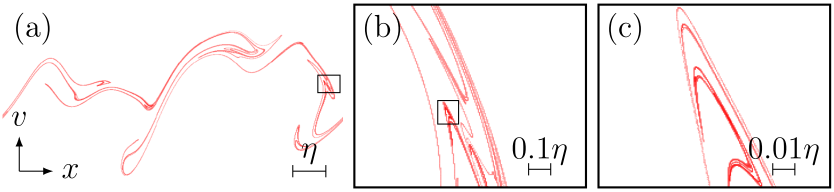

Figure 3.2: Fractal structure of the phase-space particle density ϱ_{t,t_0} for the one-dimension statistical model at $\Delta t = 50$, simulated in the white-noise limit with $\varepsilon = 1.5$ and 10^7 particles. (a) $\varrho_{t,t_0} \approx \bar{\varrho}_t$ without magnification. The position is plotted horizontally, the velocity vertically. The logarithmic colour coding shows the magnitude of $\bar{\varrho}_t$. (b) Magnification of the black box in subfigure (a). (c) Magnification of the black box in subfigure (b).

the red region in Fig. 3.2 is the finite-time approximation of a time-dependent attractor $\mathscr{F}_t$ of the dynamics (3.1). We define $\mathscr{F}_t$ as the set of points, where the infinite-time density is finite, $\bar{\varrho}_t(\boldsymbol{x},\boldsymbol{v}) > 0$:

$$\mathscr{F}_t = \{(\boldsymbol{x},\boldsymbol{v}) \in V | \bar{\varrho}_t(\boldsymbol{x},\boldsymbol{v}) > 0\}\,. \tag{3.5}$$

The density $\bar{\varrho}_t$ is time dependent because it is a function of the realisation of the time-dependent fluid-velocity field $\boldsymbol{u}(\boldsymbol{x},t)$. Therefore, also the attractor $\mathscr{F}_t$ changes a function of time, and its detailed shape depends on the entire history of the fluid-velocity field $\boldsymbol{u}(\boldsymbol{x},t)$. For this reason $\mathscr{F}_t$ is sometimes called a 'dynamically evolving attractor' [11, 17]. That the phase-space volume $\mathscr{V}_t$ along trajectories tends to zero in the long-time limit implies that the attractor $\mathscr{F}_t$ has zero phase-space volume $\int_{\mathscr{F}_t} \mathrm{d}\boldsymbol{x}\mathrm{d}\boldsymbol{v} = 0$. Hence, $\mathscr{F}_t$ can occupy at most a sub-volume of the phase space. Although $\mathscr{F}_t$ is a function of time, we can define fixed statistical quantities (fractal dimensions) that characterise the attractor, and the properties of the infinite-time density $\bar{\varrho}_t$, by averaging over realisations of $\boldsymbol{u}(\boldsymbol{x},t)$. I discuss these 'observables' in Section 4.1.

Fig. 3.2 shows that ϱ_{t,t_0} becomes a singular object for long times, so that the limit in Eq. (3.4) is possibly mathematically ill-defined. It is therefore useful to consider a so-called measure μ_t which gives the probability contained in arbitrary subset $\mathscr{S}$ of phase space. We define

$$\mu_t(\mathscr{S}) = \int_{\mathscr{S}} \mathrm{d}\mu_t(\boldsymbol{x},\boldsymbol{v}) \equiv \lim_{t_0\to-\infty} \int_{\mathscr{S}} \mathrm{d}\boldsymbol{x}\mathrm{d}\boldsymbol{v}\,\varrho_{t,t_0}(\boldsymbol{x},\boldsymbol{v})\,, \tag{3.6}$$

assuming that the limit exists. The differential of the measure, $\mathrm{d}\mu_t(\boldsymbol{x},\boldsymbol{v})$, gives the probability contained in an infinitesimal, $2d$-dimensional volume element $\mathrm{d}\boldsymbol{x}\mathrm{d}\boldsymbol{v}$ located at $(\boldsymbol{x},\boldsymbol{v})$. We write it as

$$\mathrm{d}\mu_t(\boldsymbol{x},\boldsymbol{v}) = \bar{\varrho}_t(\boldsymbol{x},\boldsymbol{v})\mathrm{d}\boldsymbol{x}\mathrm{d}\boldsymbol{v}\,, \tag{3.7}$$

so that $\bar{\varrho}_t$ is the density associated with measure μ_t. If the long-time limit is singular, the equality in Eq. (3.7) must be interpreted in a distributional sense and thus inside an integral as in Eq. (3.6). The measure μ_t, however, remains finite.

3.2 Local phase-space dynamics

The global evolution of the phase-space density ϱ_{t,t_0} is difficult to describe mathematically. Oftentimes, a local description based on the deformation of small neighbourhoods of particles around a reference trajectory is more appropriate. The phase-space velocity field $\boldsymbol{F}_t(\boldsymbol{x},\boldsymbol{v})$ stretches and contracts particle neighbourhoods as time evolves. The long-time statistics of these deformations allows us eventually to compute important properties of the global long-time phase-space density $\bar{\varrho}_t$.

The relative motion of particles in the neighbourhood around a trajectory is described by the so-called tangent flow [55]. The equation of motion for the tangent flow is derived by linearising the equation of motion (3.1). We consider the separation $\delta\boldsymbol{x}_t$ and relative velocity $\delta\boldsymbol{v}_t$ between a reference trajectory $(\boldsymbol{x}_t,\boldsymbol{v}_t)$, and a second trajectory $(\boldsymbol{x}'_t,\boldsymbol{v}'_t)$ that is infinitesimally close to the first one. We write $\boldsymbol{R}_t = (\delta\boldsymbol{x}_t,\delta\boldsymbol{v}_t)^{\mathsf{T}} = (\boldsymbol{x}_t-\boldsymbol{x}'_t,\boldsymbol{v}_t-\boldsymbol{v}'_t)^{\mathsf{T}}$. That the phase-space separation is infinitesimal requires that $\mathscr{R}_t = |\boldsymbol{R}_t| \ll 1$. The phase-space separation $\boldsymbol{R}_t = (\delta\boldsymbol{x}_t,\delta\boldsymbol{v}_t)^{\mathsf{T}}$ is then a tangent vector in the tangent space of the system at $(\boldsymbol{x}_t,\boldsymbol{v}_t)$. From Eq. (3.1) one obtains the equation of motion for $\boldsymbol{R}_t$, the tangent flow of $(\boldsymbol{x}_t,\boldsymbol{v}_t)$:

$$\tfrac{\mathrm{d}}{\mathrm{d}t}\boldsymbol{R}_t = \mathbb{W}_t(\boldsymbol{x}_t)\boldsymbol{R}_t\,, \qquad \mathbb{W}_t(\boldsymbol{x}_t) = \begin{pmatrix} 0_{d\times d} & \mathbb{1}_{d\times d} \\ \mathbb{A}(\boldsymbol{x}_t,t) & -\mathbb{1}_{d\times d}\end{pmatrix}. \tag{3.8}$$

Here $0_{d\times d}$ and $\mathbb{1}_{d\times d}$ are the d-dimensional zero and identity matrices, respectively. Furthermore, $\mathbb{A}(\boldsymbol{x},t)$ is the fluid-velocity gradient matrix with components $A_{ij} = \partial u_i(\boldsymbol{x},t)/\partial x_j$. The fluid-velocity gradient matrix is a random, matrix-valued function of $\boldsymbol{x}$ and t with zero mean. From Eqs. (2.17) and (2.18) it follows that $\mathbb{A}(\boldsymbol{x},t)$ has the correlation function [7, 17]

$$\langle A_{ik}(\boldsymbol{x},t)A_{jl}(\boldsymbol{x},t')\rangle = \frac{\mathrm{Ku}^2\mathrm{St}^2}{d} C_{ijkl}\exp(-\mathrm{St}|t-t'|)\,, \tag{3.9}$$

with

$$C_{ijkl} = \left(\frac{d+1-2\wp}{d-1}\right)\delta_{ij}\delta_{kl} + \left(\frac{\wp d-1}{d-1}\right)(\delta_{ik}\delta_{jl}+\delta_{il}\delta_{jk})\,. \tag{3.10}$$

The tangent flow (3.8) needs to be evaluated together with the equation of motion (3.1) of the reference trajectory.

Since Eq. (3.8) is linear in $\boldsymbol{R}_t$, its solution can be expressed as a Green function $\mathbb{J}_t$,

$$\boldsymbol{R}_t = \mathbb{J}_t \boldsymbol{R}_{t_0}\,, \quad \mathbb{J}_t = \mathscr{T}\exp\left(\int_{t_0}^{t} \mathrm{d}t'\,\mathbb{W}_{t'}(\boldsymbol{x}_{t'})\right)\,, \tag{3.11}$$

with initial condition $\mathbb{J}_{t_0} = \mathbb{1}_{2d\times 2d}$. The function $\mathscr{T}\exp(\ldots)$ is the time-ordered exponential. Time ordering is required, since the argument $\mathbb{W}_t$ in the integral is a matrix, which does not in general commute for different times. Note that $\mathbb{J}_t$ depends on the whole trajectory $(\boldsymbol{x}_{t'},\boldsymbol{v}_{t'})_{t_0\le t'\le t}$, which is a solution of the equation of motion (3.1) with initial condition $(\boldsymbol{x}_{t_0},\boldsymbol{v}_{t_0})$ at time t_0. The formal expression for $\mathbb{J}_t$ in Eq. (3.11) is therefore difficult to solve in general.

The Green function $\mathbb{J}_t$ determines how infinitesimal neighbourhoods are deformed and rotated by the phase-space velocity field $\boldsymbol{F}_t(\boldsymbol{x},\boldsymbol{v})$. Therefore, $\mathbb{J}_t$ is sometimes called ‘deformation matrix’ [17]. Important information about the dynamics of the neighbourhood around the reference trajectory at time t is contained in the eigenvalues of $\mathbb{J}_t$. By the polar decomposition theorem we can express $\mathbb{J}_t$ as the combination of a rotation $\mathbb{R}_t$ and a symmetric left or right stretch matrix, $\mathbb{V}_t$ or $\mathbb{U}_t$, respectively [19]:

$$\mathbb{J}_t = \mathbb{V}_t\mathbb{R}_t = \mathbb{R}_t\mathbb{U}_t\,. \tag{3.12}$$

Equation (3.12) says that a phase-space neighbourhood of particles, characterised by a $2d$-dimensional, orthonormal coordinate system at time t_0 is rotated by $\mathbb{R}_t$ and stretched along the eigendirections of $\mathbb{V}_t$ or $\mathbb{U}_t$. As a result, an orthogonal set of vectors is sheared under the action of $\mathbb{J}_t$, and

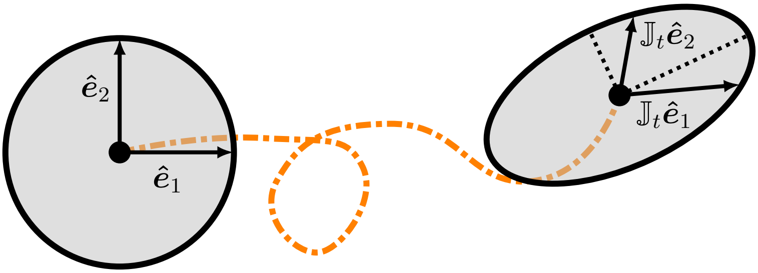

Figure 3.3: Illustration of the deformation and rotation of a phase-space neighbourhood by the deformation matrix $\mathbb{J}_t$. The orthogonal vectors $(\hat{\boldsymbol{e}}_1, \hat{\boldsymbol{e}}_2)$ at $(\boldsymbol{x}_{t_0}, \boldsymbol{v}_{t_0})$ are mapped to $(\mathbb{J}_t\hat{\boldsymbol{e}}_1, \mathbb{J}_t\hat{\boldsymbol{e}}_2)$ at $(\boldsymbol{x}_t, \boldsymbol{v}_t)$, and are not orthogonal any more. The dotted lines are the main axes of the deformed ellipse with lengths $\mathrm{e}^{\varrho_t^{(1)}} > \mathrm{e}^{\varrho_t^{(2)}}$. The yellow dash-dotted line shows the phase-space reference trajectory.

the orthogonality of the coordinate system is not in general conserved. The symmetric matrices $\mathbb{V}_t$ and $\mathbb{U}_t$ are given by the matrix square-roots

$$\mathbb{V}_t = (\mathbb{J}_t\mathbb{J}_t^{\mathsf{T}})^{1/2}, \qquad \mathbb{U}_t = (\mathbb{J}_t^{\mathsf{T}}\mathbb{J}_t)^{1/2}. \tag{3.13}$$

This implies that $\mathbb{V}_t$ and $\mathbb{U}_t$ have the same eigenvalues, but different eigenvectors. Because $\mathbb{J}_t$ can be written as the time-ordered exponential in Eq. (3.11), the eigenvalues of $\mathbb{V}_t$ and $\mathbb{U}_t$ typically grow or contract exponentially in time. Therefore, it is convenient to write the eigenvalues as $(\exp[\rho_t^{(1)}], \ldots, \exp[\rho_t^{(2d)}])$. The time-dependent exponents $\rho_t^{(1)}, \ldots, \rho_t^{(2d)}$ are called 'stretching exponents' [7, 55, 60]. We order the eigenvalues according to their magnitude so that

$$\rho_t^{(1)} \geq \rho_t^{(2)} \geq \ldots \geq \rho_t^{(2d)}. \tag{3.14}$$

How the deformation matrix maps tangent vectors is shown schematically for a two-dimensional phase space in Fig. 3.3: The initial tangent space at $(\boldsymbol{x}_{t_0}, \boldsymbol{v}_{t_0})$ is spanned by the two vectors $(\hat{\boldsymbol{e}}_1, \hat{\boldsymbol{e}}_2)$. The deformation matrix maps these vectors to the non-orthogonal vectors $(\mathbb{J}_t\hat{\boldsymbol{e}}_1, \mathbb{J}_t\hat{\boldsymbol{e}}_2)$ at $(\boldsymbol{x}_t, \boldsymbol{v}_t)$, spanning the tangent space at $(\boldsymbol{x}_t, \boldsymbol{v}_t)$. The axes lengths of the ellipsoidal neighbourhood at time t are given by the eigenvalues of $\mathrm{e}^{\rho_t^{(1)}} > \mathrm{e}^{\rho_t^{(2)}}$, corresponding to the lengths of the dotted lines in Fig. 3.3.

The dynamics of infinitesimal phase-space volumes is particularly simple. Infinitesimal volume changes are given by the determinant of $\mathbb{J}_t$ and thus by the product of the eigenvalues of the stretch matrices. The determinant $\det \mathbb{J}_t$ obeys the simple equation of motion

$$\tfrac{\mathrm{d}}{\mathrm{d}t} \det \mathbb{J}_t = \mathrm{Tr}[\mathbb{W}_t(\boldsymbol{x}_t)] \det \mathbb{J}_t \,, \tag{3.15}$$

with solution $\det \mathbb{J}_t = \mathrm{e}^{-d(t-t_0)}$. This result is the local analogue of Eq. (3.3), implying an exponential contraction of local phase-space volumes along trajectories. As a result of this contraction, the $2d$ phase-space stretching exponents $\rho_t^{(i)}$ are related by the sum rule

$$\sum_{i=1}^{2d} \rho_t^{(i)} = -d(t-t_0) \,, \tag{3.16}$$

so that only $2d-1$ of the stretching exponents are independent.

3.2.1 Cauchy-Green tensors

The deformation matrix $\mathbb{J}_t$ describes the rotation and the shearing of neighbourhoods of particles in phase-space. Studying $\mathbb{J}_t$ directly has two main disadvantages: First, $\mathbb{J}_t$ need not be symmetric, so that its eigenvectors and eigenvalues are in general complex. Second, due to the residual rotations in the polar decomposition (3.12), the deformation matrix $\mathbb{J}_t$ does not converge in the long-time limit.

It turns out to be convenient to introduce the symmetric left and right Cauchy-Green tensors $\mathbb{B}_t$ and $\mathbb{C}_t$, respectively, defined by

$$\mathbb{B}_t = \mathbb{J}_t \mathbb{J}_t^{\mathsf{T}} \,, \qquad \mathbb{C}_t = \mathbb{J}_t^{\mathsf{T}} \mathbb{J}_t \,. \tag{3.17}$$

Both the left Cauchy-Green tensor $\mathbb{B}_t$ and the right Cauchy-Green tensor $\mathbb{C}_t$ are symmetric so that their eigenvectors form an orthogonal basis, and their eigenvalues are real. A comparison with Eq. (3.13) shows that $\mathbb{B}_t = \mathbb{V}_t^2$ and $\mathbb{C}_t = \mathbb{U}_t^2$. Hence, just as the stretch matrices $\mathbb{V}_t$ and $\mathbb{U}_t$, the Cauchy-Green tensors $\mathbb{B}_t$ and $\mathbb{C}_t$ have identical eigenvalues, given by $(\exp[2\rho_t^{(1)}], \ldots, \exp[2\rho_t^{(2d)}])$. Furthermore, the left Cauchy-Green tensor $\mathbb{B}_t$ has the same eigenvectors as the left stretch matrix $\mathbb{V}_t$, while the right Cauchy-Green tensor $\mathbb{C}_t$ has the same eigenvectors as the right stretch matrix $\mathbb{U}_t$. The eigenvectors of $\mathbb{B}_t$ and $\mathbb{V}_t$ are, however, different from the eigenvectors of $\mathbb{C}_t$ and $\mathbb{U}_t$.

The most important property of the right Cauchy-Green tensor $\mathbb{C}_t$ is its convergence

$$\lim_{t\to\infty}\frac{1}{2(t-t_0)}\log\mathbb{C}_t=\mathbb{L}\,, \tag{3.18}$$

ensured by the 'multiplicative ergodic theorem' [55, 61, 62].

That the time-rescaled logarithm of $\mathbb{C}_t$ converges to the fixed matrix $\mathbb{L}$ has two major implications. First, time-rescaled stretching exponents $\rho_t^{(i)}/(t-t_0)$ converge to fixed limits as $t\to\infty$. These limits define the 'Lyapunov exponents', which are characteristic for the long-time behaviour of particle neighbourhoods. When the largest Lyapunov exponent is positive, $\lim_{t\to\infty}\rho_t^{(1)}/(t-t_0)>0$, the particle dynamics is often chaotic [18, 19, 20], and depends sensitively on the initial conditions. I discuss the Lyapunov exponents in more detail in the Section 4.2. Second, the eigenvectors of $\mathbb{C}_t$ must converge to fixed orthogonal vectors. Hence, the orthogonal matrix $\tilde{\mathbb{O}}_t$ that diagonalises $\mathbb{C}_t$ converges in the long-time limit, $\tilde{\mathbb{O}}_t\to\tilde{\mathbb{O}}$.

The convergence property (3.18) holds only for the right Cauchy-Green tensor $\mathbb{C}_t$. To understand the relation between the left and right Cauchy-Green tensor, we write the deformation matrix $\mathbb{J}_t$ as

$$\mathbb{J}_t=\mathbb{R}_t\mathbb{U}_t=\mathbb{R}_t\mathbb{C}_t^{1/2}=\mathbb{R}_t\tilde{\mathbb{O}}_t\,\mathrm{diag}\Big(\mathrm{e}^{\rho_t^{(1)}},\mathrm{e}^{\rho_t^{(2)}},\ldots,\mathrm{e}^{\rho_t^{(2d)}}\Big)\tilde{\mathbb{O}}_t^{\mathsf{T}}\,. \tag{3.19}$$

For the left Cauchy-Green tensor $\mathbb{B}_t=\mathbb{J}_t\mathbb{J}_t^{\mathsf{T}}$, on the other hand we have $\mathbb{J}_t=\mathbb{V}_t\mathbb{R}_t=\mathbb{B}_t^{1/2}\mathbb{R}_t$, so that $\mathbb{B}_t^{1/2}=\mathbb{J}_t\mathbb{R}_t^{\mathsf{T}}=\mathbb{R}_t\mathbb{C}_t^{1/2}\mathbb{R}_t^{\mathsf{T}}$. Together with Eq. (3.19) this leads to

$$\mathbb{B}_t^{1/2}=\mathbb{R}_t\tilde{\mathbb{O}}_t\mathrm{diag}\Big(\mathrm{e}^{\rho_t^{(1)}},\mathrm{e}^{\rho_t^{(2)}},\ldots,\mathrm{e}^{\rho_t^{(2d)}}\Big)\tilde{\mathbb{O}}_t^{\mathsf{T}}\mathbb{R}_t^{\mathsf{T}}\,. \tag{3.20}$$

Hence, the combined rotation $\mathbb{O}_t=\mathbb{R}_t\tilde{\mathbb{O}}_t$ diagonalises both the left Cauchy-Green tensor $\mathbb{B}_t$ and the left stretch matrix $\mathbb{V}_t$. In other words, the eigenvectors of $\mathbb{B}_t$ determine the orientation of the main axes of the particle neighbourhood, shown as the dotted lines in Fig. 3.3. In that sense, $\mathbb{B}_t$ contains additional information about the dynamics of phase-space neighbourhoods.

A very convenient property of the left Cauchy-Green tensor is its time evolution. By taking a time derivative of $\mathbb{B}_t=\mathbb{J}_t\mathbb{J}_t^{\mathsf{T}}$ and using $\frac{\mathrm{d}}{\mathrm{d}t}\mathbb{J}_t=\mathbb{W}_t\mathbb{J}_t$ we find that $\mathbb{B}_t$ obeys the closed evolution equation

$$\tfrac{\mathrm{d}}{\mathrm{d}t}\mathbb{B}_t=\mathbb{W}_t\mathbb{B}_t+\mathbb{B}_t\mathbb{W}_t^{\mathsf{T}}\,. \tag{3.21}$$

Starting from Eq. (3.21), we use a method described in Ref. [60] to obtain stochastic differential equations for the eigenvectors $\boldsymbol{e}_t^{(i)}$ of $\mathbb{B}_t$, and for the stretching exponents $\rho_t^{(i)}$. After an initial transient, one finds [60]:

$$\frac{\mathrm{d}}{\mathrm{d}t}\boldsymbol{e}_t^{(i)}=\mathbb{W}_t\boldsymbol{e}_t^{(i)}-\Big(\boldsymbol{e}_t^{(i)}\cdot\mathbb{W}_t\boldsymbol{e}_t^{(i)}\Big)\boldsymbol{e}_t^{(i)}-\sum_{j<i}\Big(\boldsymbol{e}_t^{(j)}\cdot[\mathbb{W}_t+\mathbb{W}_t^{\mathsf{T}}]\boldsymbol{e}_t^{(i)}\Big)\boldsymbol{e}_t^{(j)}\,, \tag{3.22a}$$

$$\frac{\mathrm{d}}{\mathrm{d}t}\rho_t^{(i)}=\boldsymbol{e}_t^{(i)}\cdot\mathbb{W}_t\boldsymbol{e}_t^{(i)}\,. \tag{3.22b}$$

Equations (3.22), together with with the equation of motion (3.1) for the reference trajectory provide a useful tool for the local analysis of the phase-space dynamics of particles. Equations (3.22) determine both the orientation [Eq. (3.22a)], and the lengths [Eq. (3.22b)] of the main axes of the phase-space neighbourhood. Note that Eqs. (3.22a) are decoupled from Eq. (3.22b). This decoupling happens after an initial transient, provided that the stretching exponents are all different [60].

As we have seen, the right and left Cauchy-Green tensors, $\mathbb{C}_t$ and $\mathbb{B}_t$, have complementary properties. The convergence property (3.18) of $\mathbb{C}_t$ allows to prove the multiplicative ergodic theorem. This theorem ensures the convergence of the rescaled phase-space stretching exponents $\rho_t^{(i)}/(t-t_0)$. The left Cauchy-Green tensor $\mathbb{B}_t$ has the same eigenvalues as $\mathbb{C}_t$. Furthermore, the eigenvectors $\boldsymbol{e}_t^{(i)}$ of $\mathbb{B}_t$ determine the orientation of main axes of the phase-space neighbourhood, shown as the dotted lines in Fig. 3.3. This orientation is important when we consider projections of particle neighbourhoods in Chapter 6. The eigenvectors $\boldsymbol{e}_t^{(i)}$ of $\mathbb{B}_t$ and the stretching exponents $\rho_t^{(i)}$ obey the closed evolution equations (3.22). I use these equations in Chapters 5 and 6, and in Paper C, to calculate the long-time statistics of the stretching exponents.

Note that although $\mathbb{B}_t$ gives the orientation of the particle neighbourhood, its eigenvectors are not identical to the eigenvectors of $\mathbb{J}_t$. The eigenvectors and eigenvalues of the deformation matrix $\mathbb{J}_t$ are in general complex, since $\mathbb{J}_t$ is not in general symmetric. In the generic case, the real parts of the eigenvalues of $\mathbb{J}_t$ are identical to the eigenvalues of $\mathbb{U}_t$ and $\mathbb{V}_t$ [19]. Counter examples, however, can be constructed when the stretching exponents are degenerate [63].

3.2.2 White-noise limit

In the white-noise limit, the evolution of infinitesimal neighbourhoods simplifies considerably. Recall from Section 2.5.2 that the white-noise limit is taken by letting Ku → 0 and St → ∞ such that the white-noise parameter $\varepsilon^2 = \mathrm{Ku}^2\mathrm{St}d^{-1}\left(1+2\wp\right)$ stays constant. In this limit, both the fluid-velocity field $\boldsymbol{u}(\boldsymbol{x},t)$ and fluid-velocity gradients $\mathbb{A}(\boldsymbol{x},t)$ become white-noise signals. More importantly, the statistics of the fluid-velocity field $\boldsymbol{u}(\boldsymbol{x}_t,t)$ and of the fluid-velocity gradient matrix $\mathbb{A}(\boldsymbol{x}_t,t)$ become independent of the particle position $\boldsymbol{x}_t$. As a consequence, the dynamics of the particle neighbourhood (3.8) becomes independent of the dynamics of the reference trajectory (3.1) [17]. This is the great simplification of the white-noise limit. The dynamics of infinitesimal phase space separations $\boldsymbol{R}_t$ simplifies to

$$\tfrac{\mathrm{d}}{\mathrm{d}t}\boldsymbol{R}_t = \mathbb{W}_t\boldsymbol{R}_t\,,\quad \mathbb{W}_t = \begin{pmatrix} 0_{d\times d} & \mathbb{1}_{d\times d} \\ \mathbb{A}_t & -\mathbb{1}_{d\times d}\end{pmatrix}. \tag{3.23}$$

In distinction to Eq. (3.8), $\mathbb{W}_t$ in Eq. (3.23) is independent of the particle position $\boldsymbol{x}_t$. The matrix-valued, Gaussian white-noise process $\mathbb{A}_t$ has zero mean and correlation function:

$$\langle A_{ik}(t)A_{jl}(t')\rangle = \frac{2\varepsilon^2}{1+2\wp}C_{ijkl}\delta(t-t')\,, \tag{3.24}$$

with tensor C_{ijkl} given in Eq. (3.10). The white-noise limit allows for analytical calculations, since the tangent flow Eq. (3.23) constitutes a so-called Markov system [52, 64]. This means that the increments of the phase-space separation $\boldsymbol{R}_t$ and of the deformation matrix $\mathbb{J}_t$ depend only on the states of $\boldsymbol{R}_t$ and $\mathbb{J}_t$ at time t, respectively, and thus not on the past.

To conclude, I introduced in this chapter several important quantities and concepts which allow for a systematical study of the statistical model of heavy particles in turbulence. The global dynamics is characterised by the phase-space particle density ϱ_{t,t_0}. This quantity tends to the singular density $\bar{\varrho}_t$, with associated measure μ_t, in the long-time limit. In this limit, the phase-space density is supported by a time-dependent, fractal attractor $\mathscr{F}_t$. A general concept that I use throughout this thesis is to study the local deformations of particle neighbourhoods instead of the global dynamics. These deformations are determined by the properties of the deformation matrix $\mathbb{J}_t$, evaluated along a reference trajectory. How $\mathbb{J}_t$ stretches and rotates infinitesimal phase-space neighbourhoods is, in turn, quantified by the stretching exponents $\rho_t^{(i)}$, with corresponding eigenvectors $\boldsymbol{e}_t^{(i)}$ of the left Cauchy-Green tensor $\mathbb{B}_t = \mathbb{J}_t\mathbb{J}_t^{\mathsf{T}}$. Intuitively it might be reasonable that the local deformation of neighbourhoods has implications for the global dynamics in the long-time limit. The precise connection between the two formulations is made in Chapter 4.

Phase-space clustering of the kind observed in this chapter is particular to mono-disperse particle suspensions. In more realistic systems with particles of different sizes, the particles react differently to the same fluid-velocity field $\boldsymbol{u}(\boldsymbol{x}, t)$. In which way the results for mono-disperse suspensions can be applied to particle systems in nature is, a priori, unclear. In Chapter 8, and in Paper A, I discuss how the present picture needs to be adjusted for systems of non-identical particles.

4 Observables

A systematic analysis of the distribution of heavy particles in turbulence requires statistical observables that can be compared. For the analysis of the phase-space density in the statistical model, such observables can be defined globally, or locally. Globally defined observables require, at least approximately, the knowledge of the dynamics on the entire phase space. Local observables, on the other hand, rely only on the dynamics of phase-space neighbourhoods. Therefore, it is often easier to reliably compute local observables than global ones. Sometimes, the precise knowledge of the local dynamics allows to compute global observables.

In this chapter, I discuss two commonly used sets of phase-space observables, the Renyi dimensions and the finite-time Lyapunov exponents (FTLEs). The standard methods for calculating the Renyi dimensions are global, and they are thus hard to obtain numerically. I review these methods in the first section of the chapter. The FTLEs determine the statistics of stretching and compression of local phase-space neighbourhoods. They are computed using the tangent flow, and are thus intrinsically local. In phase-space, the FTLEs have convenient mathematical properties in the long-time limit, which I review in the second section. In the last section, I describe how the statistics of FTLEs are connected to the Renyi dimensions.

4.1 Phase-space Renyi dimensions

The Renyi dimension D_q with $q \in \mathbb{R}$ is a one-parameter family of numbers that provide information about the small-scale structure of the phase-space measure μ_t [65, 66, 67, 68]. The perhaps most well-known representative of D_q is the 'box counting dimension' D_0. The box-counting dimension quantifies, how much the fractal attractor $\mathscr{F}_t$ fills out phase-space. When the attractor is not a fractal set but a smooth set, then D_0 agrees with the topological dimension, the number of parameters needed to parametrise the set. That is, if $\mathscr{F}_t$ is a smooth curve, then $D_0 = 1$, for a surface one has $D_0 = 2$ and so on. When D_0 is not an integer, on the other hand, the attractor is said to be a fractal. For $1 < D_0 < 2$, for instance, the fractal is more space-filling than a line, but less space-filling than a surface.

For $q \neq 0$, the Renyi dimensions describe characteristics of the measure μ_t

supported by the attractor $\mathscr{F}_t$. They characterise how (in-)homogeneously the fractal attractor $\mathscr{F}_t$ is sampled by the dynamics (3.1). The physically most relevant [9] Renyi dimension is D_2, the correlation dimension [69], which gives the probability scaling of the phase-space separation $\mathscr{R}_t \equiv |\boldsymbol{R}_t|$ between two particles:

$$P(\mathscr{R}_t \le \delta) \propto \delta^{D_2}\,, \qquad \delta \ll 1\,. \tag{4.1}$$

For general q, we define the Renyi dimension D_q in terms of the statistics of the probability ('mass') $\mathscr{M}_\delta(\boldsymbol{x},\boldsymbol{v})$ contained in a small box or a ball of varying size δ around a phase-space point $(\boldsymbol{x},\boldsymbol{v})$. For small δ, the moments $\langle \mathscr{M}_\delta^n \rangle$ have a power-law scaling in δ of the form [66, 67, 68]

$$\langle \mathscr{M}_\delta^n \rangle \propto \delta^{\xi_n}\,, \qquad \delta \ll 1\,. \tag{4.2}$$

Here, the exponent ξ_n, called the singularity spectrum [70], is a function of the order of the mass moment $n \in \mathbb{R}$. The average in Eq. (4.2) must be taken both over the phase-space measure μ_t and over realisations of the fluid-velocity field $\boldsymbol{u}(\boldsymbol{x},t)$. Since we allow n to take negative values we always need to exclude from the average in Eq. (4.2) the points $(\boldsymbol{x},\boldsymbol{v})$ in phase space for which $\mathscr{M}_\delta(\boldsymbol{x},\boldsymbol{v}) = 0$.

The Renyi dimension [65] D_q are obtained from the singularity spectrum ξ_n by

$$D_q = \frac{\xi_{q-1}}{q-1}\,. \tag{4.3}$$

When the phase-space measure μ_t of particles can be written in terms of a non-singular density, all Renyi dimensions are equal to the dimensionality $2d$ of phase-space, $D_q = 2d$ [71]. In other words, the phase-space density must be singular in order to obtain $D_q \ne 2d$. When D_q is constant but not equal to $2d$, the measure μ_t is said to be (mono-)fractal, with fractal dimension $D_q = D_0$. For 'multifractal' measures, D_q is a non-trivial and non-increasing function of q [72].

There are two commonly used algorithms to calculate the Renyi dimension D_q. The first method is to calculate the scaling of the mass moments in Eq. (4.2) by discretising the whole phase space by a sequence of box-grids with decreasing grid size δ_m, so that $\delta_m \to 0$ as $m \to \infty$ [66, 67]. In general,

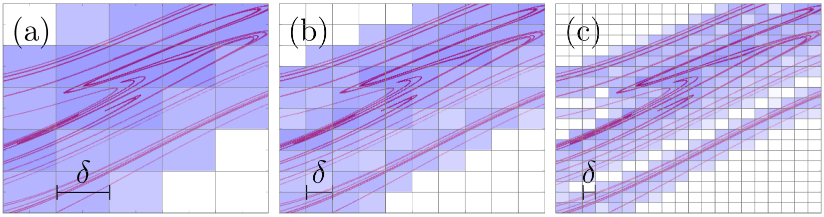

Figure 4.1: Successive covering of the phase-space fractal with boxes of decreasing size δ_m. The fractal measure is shown is red. The covering boxes are shown in blue, its darkness represents the measure (mass) contained in the corresponding box. (a) $\delta_m = 1/5$, $N_m = 21$. (b) $\delta_m = 1/10$, $N_m = 75$. (c) $\delta_m = 1/20$, $N_m = 260$. For this realisation of the fractal $\mathscr{F}_t$, and the measure μ_t, the Renyi dimension D_q takes for $q = 0,1,2$ the values $D_0 \approx 1.20$, $D_1 \approx 1.18$ and $D_2 \approx 1.05$.

only a subset of the boxes of the grids overlap with the fractal attractor $\mathscr{F}_t$ at time t. Therefore, only a small fraction of the boxes are non-empty and contribute to the average in Eq. (4.2). The probability $\mathscr{M}_{\delta_m,i}$ contained in the i-th non-empty box $N_{\delta_m,i}$ of side length δ_m is given by

$$\mathscr{M}_{\delta_m,i} = \mu_t(N_{\delta_m,i}) = \int_{N_{\delta_m,i}} \mathrm{d}\mu_t(\boldsymbol{x},\boldsymbol{v})\,. \tag{4.4}$$

At grid level m, we denote by N_m the total number of non-empty boxes with $\mathscr{M}_{\delta_m,i} > 0$. The singularity spectrum ξ_n is then defined in the limit $m \to \infty$ by

$$\xi_n = \lim_{m\to\infty} \frac{1}{\log \delta_m} \log \left\langle \sum_{i=1}^{N_m} \mathscr{M}_{\delta_m,i}^{n+1} \right\rangle_u\,. \tag{4.5}$$

Here the sum is taken over the non-empty boxes. Note that the measure μ_t and the masses $\mathscr{M}_\delta$ are discretised equally in this construction. Therefore, the average over the phase-space measure in Eq. (4.2) is replaced by the sum over non-empty boxes, and the exponent of $\mathscr{M}_{\delta_m,i}$ is $n+1$. The discretised measure μ_t is normalised at each level m, so that $\sum_{i=1}^{N_m} \mathscr{M}_{\delta_m,i} = 1$ for all m. The average $\langle \ldots \rangle_u$ in Eq. (4.5) is taken over realisations of the fluid-velocity field $\boldsymbol{u}(\boldsymbol{x},t)$.

Fig. 4.1 shows the covering of the fractal attractor by a sequence of boxes for a two-dimensional phase-space, and for a single realisation of the fluid-velocity field $\boldsymbol{u}(\boldsymbol{x},t)$. The fractal attractor is shown in red, the non-empty boxes are shown in blue. The colour-code for the boxes is chosen such that darker boxes correspond to larger phase-space mass $\mathscr{M}_{\delta_m,i}$.

Choosing $q=0$ in Eq. (4.3) and evaluating the sum in Eq. (4.5) for $n=-1$ explains why D_0 is called the box-counting dimension: D_0 gives the rate at which the number of non-empty boxes diverges as $m\to\infty$. Note that D_0 is blind to the measure μ_t on the fractal attractor $\mathscr{F}_t$, since $\mathscr{M}_{\delta_m,i}$ does not appear in the sum in Eq. (4.5) for $n=-1$. Hence, D_0 only provides information about the geometry of the fractal attractor $\mathscr{F}_t$ itself, and not about how densely the particles accumulate in different regions of it. Varying q, on the other hand, changes the weight given to large masses compared to small ones. For $q>0$ large masses are given more weight than low masses, and vice versa for $q<0$.

The grid-based discretisation scheme has the disadvantage that the whole phase-space needs to be covered with boxes. This is numerically expensive as for fractal attractors with $D_0<2d$, a large fraction of the boxes are empty as $\delta_n\to 0$.

Another commonly used, but computationally more efficient method samples the probability masses $\mathscr{M}_\delta$ directly from the fractal $\mathscr{F}_t$ in order to avoid non-empty boxes. In this 'point-based' construction [68], the masses $\mathscr{M}_\delta(\boldsymbol{x}_t,\boldsymbol{v}_t)$ are chosen to be spheres of radius δ, centered at positions $(\boldsymbol{x}_t,\boldsymbol{v}_t)$ of particles that have been evolved with the dynamics (3.1). In the long-time limit, the particles themselves sample the phase-space measure μ_t, so that the probability that $\mathscr{M}_\delta(\boldsymbol{x}_t,\boldsymbol{v}_t)=0$ is small, when the number of simulated particles is sufficient. We define the point-centered masses $\mathscr{M}_\delta(\boldsymbol{x}_t,\boldsymbol{v}_t)$ by

$$\mathscr{M}_\delta(\boldsymbol{x}_t,\boldsymbol{v}_t)=\mu_t[S_\delta(\boldsymbol{x}_t,\boldsymbol{v}_t)]=\int_{S_\delta(\boldsymbol{x}_t,\boldsymbol{v}_t)}\mathrm{d}\mu_t(\boldsymbol{x}',\boldsymbol{v}'). \tag{4.6}$$

Here, $S_\delta(\boldsymbol{x},\boldsymbol{v})$, is a phase-space ball of radius δ, centered at $(\boldsymbol{x}_t,\boldsymbol{v}_t)$. In numerical simulations, we evolve a large number $N_p\gg 1$ of particles for a long time $\Delta t=t-t_0$. In the limit $N_p\to\infty$, the probability mass $\mathscr{M}_{\delta,i}$ at the position $(\boldsymbol{x}_t^{(i)},\boldsymbol{v}_t^{(i)})$ of the i-th particle can be written as [20, 71]

$$\mathscr{M}_{\delta,i}=\lim_{N_p\to\infty}\frac{1}{N_p-1}\sum_{i\neq j}^{N_p}\theta\left[\delta-\left|\left(\boldsymbol{x}_t^{(i)}-\boldsymbol{x}_t^{(j)},\boldsymbol{v}_t^{(i)}-\boldsymbol{v}_t^{(j)}\right)\right|\right]. \tag{4.7}$$

The Heaviside step function $\theta(x)$ ensures that only particles in the phase-space ball $S_\delta(\boldsymbol{x}_t^{(i)}, \boldsymbol{v}_t^{(i)})$ contribute to the so-called 'correlation sum' [69] in Eq. (4.7). We now write the point-centered estimator of the singularity spectrum ξ_n as

$$\xi_n = \lim_{\delta\to 0} \frac{1}{\log\delta} \log \left\langle \lim_{N_p\to\infty} \frac{1}{\bar{N}_p} \sum_{i=1}^{\bar{N}_p} \mathscr{M}_{\delta,i}^n \right\rangle_u . \tag{4.8}$$

As in the previous case, the sum must be restricted to the non-empty phase-space balls with $\mathscr{M}_{\delta,i} > 0$, whose total number we denote as $\bar{N}_p \le N_p$. Since the phase-space locations of the masses $\mathscr{M}_{\delta,i}$ are, by construction, sampled from μ_t, the exponent in Eq. (4.8) is n, instead of $n+1$ in Eq. (4.5).

Regardless of the method, the Renyi dimensions require knowledge of the entire phase-space dynamics. In particular, it is difficult to obtain good statistics for the average over realisations $\langle\ldots\rangle_u$ in both Eqs. (4.5) and (4.8) [73]. A notable exception is the correlation dimension D_2. As we can see from Eq. (4.1), D_2 is determined by the probability scaling of infinitesimal phase-space separations, which can be obtained from the tangent flow. Therefore, D_2 can typically be calculated to much higher accuracy. This is particularly useful in the white-noise limit [17, 23, 24, 74, 75].

4.2 Phase-space (finite-time) Lyapunov exponents

Local observables, evaluated along particle trajectories often allow for precise numerical calculations, and in some cases even for analytical solutions. In Section 3.2 we have encountered the stretching exponents $\boldsymbol{\rho}_t = (\rho_t^{(1)}, \ldots, \rho_t^{(2d)})$ which determine the deformation of phase-space neighbourhoods. After long times, the vector $\boldsymbol{\rho}_t$ grows linearly in time. This motivates us to define the corresponding 'stretching rates' $\boldsymbol{\sigma}_t = (\sigma_t^{(i)}, \ldots, \sigma_t^{(2d)})$ by

$$\sigma_t^{(i)} = \frac{\rho_t^{(i)}}{t - t_0}, \tag{4.9}$$

also called finite-time Lyapunov exponents (FTLEs). The phase-space FTLEs determine the rates at which phase-space neighbourhoods are stretched or contracted by the deformation matrix $\mathbb{J}_t$. As stretching exponents $\boldsymbol{\rho}_t$ are

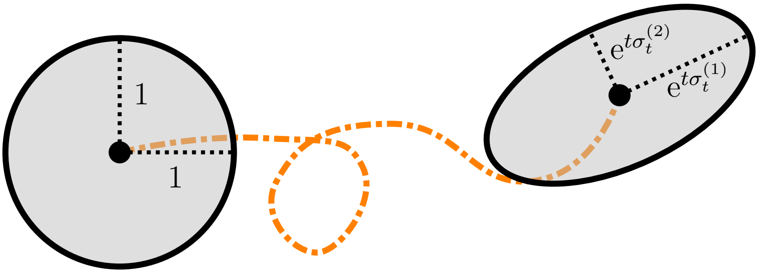

Figure 4.2: Schematic drawing of a two-dimensional phase-space neighbourhood of particles. The finite-time Lyapunov exponents determine the stretching of small particle neighbourhoods (grey shaded area) around a reference trajectory (orange, dash-dotted curve). Because the FTLEs are in general different, an initial circle is deformed into an ellipse.

ordered by to their magnitude, Eq. (3.14), so are the phase-space FTLEs $\boldsymbol{\sigma}_t$,

$$\sigma_t^{(1)} \geq \sigma_t^{(2)} \geq \ldots \sigma_t^{(2d)} . \tag{4.10}$$

The sum rule Eq. (3.16) for the stretching exponents requires that the sum of all phase-space FTLEs is constant and negative for all t:

$$\sum_{i=1}^{2d} \sigma_t^{(i)} = -d . \tag{4.11}$$

Fig. 4.2 shows schematically how the phase-space FTLEs deform local phase-space neighbourhoods. An infinitesimal neighbourhood at time t_0 is deformed into an ellipse with axis lengths $(e^{t\sigma_t^{(1)}}, e^{t\sigma_t^{(2)}})$. For a non-degenerate spectrum of FTLEs, the axis lengths are all different, so that an initial sphere is deformed into an ellipse at time $t > t_0$.

In order to get a better understanding of the role played by the phase-space FTLEs, consider a $2d$-dimensional, infinitesimal phase-space neighbourhood of particles around a reference trajectory at time t_0. For $t > t_0$, the particle neighbourhood is deformed and rotated by the deformation matrix $\mathbb{J}_t$. Typical phase-space separations $\mathscr{R}_t \equiv |\boldsymbol{R}_t|$ within the neighbourhood obey

$$\mathscr{R}_t = \sqrt{\boldsymbol{R}_{t_0}^{\mathsf{T}} \mathbb{J}_t^{\mathsf{T}} \mathbb{J}_t \boldsymbol{R}_{t_0}} = \sqrt{\boldsymbol{R}_{t_0}^{\mathsf{T}} \mathbb{C}_t \boldsymbol{R}_{t_0}} . \tag{4.12}$$

Note that the right Cauchy-Green tensor $\mathbb{C}_t = \mathbb{J}^{\mathsf{T}}\mathbb{J} = \mathbb{U}_t^2$ appears naturally in Eq. (4.12) when considering separations. The eigenvalues of $\mathbb{C}_t$ grow or shrink as $\sim \mathrm{e}^{2(t-t_0)\sigma_t^{(i)}}$. For long enough times, the largest phase-space FTLE, $\sigma_t^{(1)}$, becomes dominant. By dividing with the initial separation, we find for typical separations

$$\frac{\mathscr{R}_t}{\mathscr{R}_{t_0}} = \sqrt{\boldsymbol{n}_{t_0}^{\mathsf{T}}\mathbb{C}_t\boldsymbol{n}_{t_0}} \sim \mathrm{e}^{(t-t_0)\sigma_t^{(1)}}\left[1+\mathscr{O}\left(\mathrm{e}^{(t-t_0)[\sigma_t^{(2)}-\sigma_t^{(1)}]}\right)\right], \tag{4.13}$$

where $\boldsymbol{n}_{t_0}$ is a unit vector in the direction of $\boldsymbol{R}_{t_0}$. Eq. (4.13) says that for long enough time, typical separations grow as $\sim \mathrm{e}^{(t-t_0)\sigma_t^{(1)}}$.

Now consider an infinitesimal area $\mathscr{A}_{t_0}$ at time t_0 given by the area of the square spanned by two orthogonal vectors. As time evolves, one of the vectors must, according to Eq. (4.13), grow as $\sim \mathrm{e}^{(t-t_0)\sigma_t^{(1)}}$. The second vector, on the other hand, lies in the subspace perpendicular to the first one. Its growth or contraction is dominated by the *second* largest FTLE $\sigma_t^{(2)}$. Hence, similar to (4.13), we can write for the evolution of the area $\mathscr{A}_t$

$$\frac{\mathscr{A}_t}{\mathscr{A}_{t_0}} \sim \mathrm{e}^{(t-t_0)[\sigma_t^{(1)}+\sigma_t^{(2)}]}\left[1+\mathscr{O}\left(\mathrm{e}^{(t-t_0)[\sigma_t^{(3)}-\sigma_t^{(2)}]}\right)\right]. \tag{4.14}$$

This construction can be continued to higher dimensional (sub-)volumes in the same way. In general, the cumulative sums $\sum_{i=1}^{n}\sigma_t^{(i)}$ determine the rate of expansion or contraction of n-dimensional (sub-)volumes spanned by $n+1$ infinitesimally close trajectories in phase space.

So far, we have only considered finite times, for which the phase-space FTLEs $\boldsymbol{\sigma}_t$ depend on time and, in general, on the initial conditions $(\boldsymbol{x}_{t_0}, \boldsymbol{v}_{t_0})$ at time t_0. The convergence property (3.18) of the right Cauchy-Green tensor $\mathbb{C}_t$ [61, 62] ensures that the phase-space FTLEs attain fixed limits for $t \to \infty$:

$$\lim_{t\to\infty}\sigma_t^{(i)} = \lambda_i\,. \tag{4.15}$$

Here λ_i are the Lyapunov exponents of the particle dynamics (3.1). A positive largest Lyapunov exponent $\lambda_1 > 0$ signifies that phase-space separations grow exponentially fast as $t \to \infty$. The system is then said to depend sensitively on the initial conditions. Positivity of at least one of the Lyapunov exponents is often used as a definition of chaotic systems [18]. For the statistical model it follows from Eq. (4.11) that $\sum_{i=1}^{2d}\lambda_i = -d$, so that $\lambda_1 > 0$ implies that at

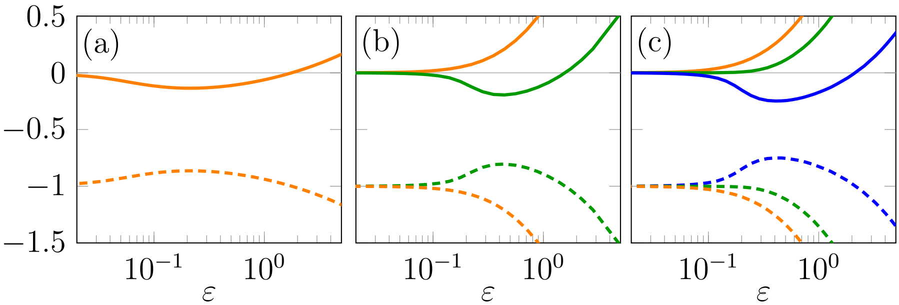

Figure 4.3: Phase-space Lyapunov exponents λ_i in the white-noise limit in spatial different dimensions d, as functions of the white-noise parameter ε. (a) One-dimensional case, $d=1$. λ_1 and λ_2 are shown in orange, as the solid and dashed line, respectively. (b) Two-dimensional case, $d=2$: λ_1 (orange, solid), λ_2 (green, solid), λ_3 (green, dashed) and λ_4 (orange, dashed). (c) Three-dimensional case $d=3$: λ_1 (orange, solid), λ_2 (green, solid), λ_3 (blue, solid), λ_4 (blue, dashed), λ_5 (green, dashed) and λ_6 (orange, dashed).

least one other Lyapunov exponent is negative. In this case, a phase-space neighbourhood is, in the infinite-time limit, stretched along (at least) one axis and compressed along (at least) one other axis. This is why the phase-space attractor $\mathscr{F}_t$ attains a filamentary, fractal shape, as shown in Figs. 3.2 and 4.1, when $\lambda_1 > 0$.

The phase-space Lyapunov exponents λ_i have been studied extensively both in the white-noise limit [54, 76, 77, 78, 79] and for finite Ku and St [17, 80]. In Fig. 4.3(a), (b) and (c) the white-noise limit results [81] for the Lyapunov exponents λ_i, $i=1,\ldots,2d$ in $d=1$, 2 and 3 are summarised. For $d=2$ and $d=3$, the fluid-velocity field is incompressible $\wp=0$. In the one-dimensional case, on the other hand, the fluid-velocity field is always fully compressible, so that $\wp=1$. In the one-dimensional case shown in Fig. 4.3(a), the leading Lyapunov exponent λ_1 is negative for small ε and changes sign at $\varepsilon_{\rm pc} \approx 1.33$ [76, 77]. The change of sign of λ_1 marks a phase transition from an ordered to a chaotic behaviour as ε passes the critical value $\varepsilon_{\rm pc}$. This phenomenon is called 'aggregation-disorder transition' [76] or 'path-coalescence transition' [77]. When $\lambda_1 < 0$ all Lyapunov exponents are negative, and the phase-space volume $\mathscr{V}_t$ eventually contracts to a point. That λ_1 is negative for $\varepsilon < \varepsilon_{\rm pc}$ is due to the compressibility of the fluid-velocity field $\boldsymbol{u}(\boldsymbol{x},t)$ in one spatial dimension. It can be observed in higher dimensional compressible fluid-velocity fields with $\wp > 0$ as well [77, 78]. For incompressible $\boldsymbol{u}(\boldsymbol{x}, t)$ in $d > 1$, the largest Lyapunov exponent λ_1 [orange, solid line in both Fig. 4.3(b) and (c)] is positive, $\lambda_1 > 0$ for all ε. A similar behaviour is observed for finite Ku and St, where the Stokes number St essentially takes the role of the white-noise parameter ε. This shows that the statistical model for heavy particles in turbulence is chaotic in $d > 1$ when the underlying fluid-velocity field $\boldsymbol{u}(\boldsymbol{x}, t)$ is incompressible. In all dimensions we can observe the pairing property of the Lyapunov exponents established in Ref. [82], $\lambda_i = -1 - \lambda_{2d+1-i}$.

For finite time, on the other hand, the phase-space FTLEs $\boldsymbol{\sigma}_t$, depend in general on the initial conditions $(\boldsymbol{x}_{t_0}, \boldsymbol{v}_{t_0})$, and on the realisation $\boldsymbol{u}(\boldsymbol{x}, t)$. Hence, the phase-space FTLEs $\boldsymbol{\sigma}_t \equiv (\sigma_t^{(1)}, \ldots, \sigma_t^{(2d)})$ are random variables with probability density $P_t(\boldsymbol{\sigma}_t = \boldsymbol{s})$. The limit (4.15) implies that

$$\lim_{t\to\infty} P_t(\boldsymbol{\sigma}_t = \boldsymbol{s}) = \delta(\boldsymbol{s} - \boldsymbol{\lambda}). \tag{4.16}$$

At large large but finite times the dependence on the initial conditions is lost, and the FTLEs $\boldsymbol{\sigma}_t$ fluctuate around the most probable value $\boldsymbol{\lambda} = (\lambda_1, \ldots, \lambda_{2d})$. In this transient state, $\boldsymbol{\sigma}_t$ obeys a large-deviation principle [83, 84, 85] which means that the probability density $P_t(\boldsymbol{\sigma}_t = \boldsymbol{s})$ takes a characteristic exponential form given by [29, 60, 86]

$$P_t(\boldsymbol{\sigma}_t = \boldsymbol{s}) \propto \mathbf{1}_{\sigma_t^{(1)} \geq \ldots \geq \sigma_t^{(2d)}} \delta\left(\sum_{i=1}^{2d} \sigma_t^{(i)} + d\right) \exp[-t I(\boldsymbol{s})]\,. \tag{4.17}$$

Here the indicator function $\mathbf{1}$ ensures the ordering (4.10) of FTLEs, while the delta function enforces the sum rule (4.11). Eq. (4.17) implies that the phase-space FTLEs $\boldsymbol{\sigma}_t$ approach the Lyapunov exponents $\boldsymbol{\lambda}$ exponentially fast in distribution. The exponential rate of approach is determined by the 'rate function' $I(\boldsymbol{s})$ in Eq. (4.17). The rate function $I(\boldsymbol{s})$ has a single minimum at $\boldsymbol{s} = \boldsymbol{\lambda}$ where it vanishes, $I(\boldsymbol{\lambda}) = 0$. This is consistent with the convergence of the density $P_t(\boldsymbol{\sigma} = \boldsymbol{s})$ to the delta function in Eq. (4.16). Due to the sum rule (4.11) we can remove the dependence on $\sigma_t^{(2d)}$ in Eq. (4.17) by integration. We therefore need to consider only the first $2d - 1$ components of $\boldsymbol{\sigma}_t$, and we take from now on $\boldsymbol{\sigma}_t = (\sigma_t^{(1)}, \ldots, \sigma_t^{(2d-1)})$ and $\boldsymbol{s} = (s_1, \ldots, s_{2d-1})$.

To establish the large-deviation principle (4.17), it is often useful to consider the scaled cumulant-generating function (SCGF) of $\boldsymbol{\sigma}_t$ defined as

[83, 84, 85, 87]

$$\Lambda(\boldsymbol{k}) = \lim_{t\to\infty} \frac{1}{t-t_0} \log\langle \exp[(t-t_0)\boldsymbol{k}\cdot\boldsymbol{\sigma}_t]\rangle\,, \tag{4.18}$$

where $\boldsymbol{k} = (k_1,\ldots,k_{2d-1})$. The existence of the SCGF $\Lambda(\boldsymbol{k})$ ensures, under certain conditions [83, 84, 85, 87], the large deviation principle (4.17) for $\boldsymbol{\sigma}_t$. The rate function $I(\boldsymbol{s})$ given by the Legendre transform of $\Lambda(\boldsymbol{k})$

$$I(\boldsymbol{s}) = \sup_{\boldsymbol{k}\in\mathbb{R}^{2d-1}} \{\boldsymbol{s}\cdot\boldsymbol{k} - \Lambda(\boldsymbol{k})\}\,. \tag{4.19}$$

This link between $\Lambda(\boldsymbol{k})$ and $I(\boldsymbol{s})$ is provided by the Gärtner-Ellis theorem [64, 88]. Note that for $d=1$, $\boldsymbol{k}=k$ is a scalar, and the range of $\Lambda(k)$ must be differentiable in order for Eq. (4.19) to hold [83, 84, 85, 87]. For non-convex rate functions, the Legendre transform (4.19) gives the 'convex hull' which may differ from the actual rate function [85]. One therefore needs to be careful when applying Eq. (4.19) for SCGFs that are not differentiable, because the Legendre transform may not give the correct result for the rate function.

Although the phase-space Lyapunov exponents are well understood, much less is known about the statistics of the phase-space FTLEs. Most studies are restricted to the small-Stokes limit $\mathrm{St} \ll 1$ [70, 86], where the FTLEs have Gaussian statistics, so that the rate function $I(\boldsymbol{s})$ is parabolic [1]. The small-Stokes regime corresponds to the small-ε regime $\varepsilon \ll 1$ of the white-noise limit of the statistical model [17]. For finite ε and $d=1$, $I(s)$ and $\Lambda(k)$ have been studied in Refs. [89, 90] using similar methods to those I describe in Chapter 6 and Paper C. These studies show that $I(s)$ is not parabolic for finite ε. Instead, large fluctuations of the FTLEs are much more likely than expected from the Gaussian approximation, with important implications for the fractal structure of the natural measure.

4.3 Relations between Renyi dimensions and FTLEs

The evolution of a local particle neighbourhood around a reference trajectory can be connected to the global properties of the fractal measure μ_t. The underlying assumption is ergodicity: The phase-space measure μ_t of any subset $\mathscr{S}$ of phase-space, is equal to the fraction of time a trajectory initialised at $t_0 \to -\infty$ spends in $\mathscr{S}$. Put differently, even a single trajectory and its neighbourhood, whose evolution is averaged for long enough time, may, in an ergodic system sample, the global properties of the measure μ_t [19].

The probably most well-known connection between the Renyi dimensions and the local properties of phase-space neighbourhoods is provided by the Kaplan-Yorke formula [91, 92]. The Kaplan-Yorke formula relates the so called 'information dimension' D_1 of a measure generated by a dynamical system to the Lyapunov exponents λ_i of the underlying dynamics. The Kaplan-Yorke formula reads

$$D_1 = k + \frac{\sum_{i=1}^{k} \lambda_k}{|\lambda_{k+1}|}\,. \tag{4.20}$$

Here k is the largest integer for which the sum in Eq. (4.20) is positive. The idea behind Eq. (4.20) is quite simple. The cumulative sum $\sum_{i=1}^{n} \lambda_i$ determines the rate at which n-dimensional (sub-)volumes of phase-space expand or contract in the infinite-time limit. Generically, any of these sums is either positive or negative for different n. The number k in Eq. (4.20) is a lower bound for a fractal dimension in which the cumulative sum of Lyapunov exponents is zero. An upper bound, on the other hand, is provided by the sum $\sum_{i=1}^{k+1} \lambda_i$. The Kaplan-Yorke formula says that the information dimension D_1 is given by linearly interpolating between the upper bound and the lower bound $(k+1-D_1)\sum_{i=1}^{k} \lambda_i + (D_1 - k)\sum_{i=1}^{k+1} \lambda_i = 0$. Equation (4.20) is known to hold for generic deterministic dynamical systems [18], and it has been proven for a broad class of random dynamical systems [93].

Note that according to Eq. (4.20), D_1 depends only on the Lyapunov exponents $\boldsymbol{\lambda}$ which have fixed values. More information is contained in the rate function $I(\boldsymbol{s})$, which provides the detailed statistics of the transient fluctuations of the FTLEs $\boldsymbol{\sigma}_t$ around $\boldsymbol{\lambda}$ for long but finite time t. The singularity spectrum ξ_n in Eq. (4.2) is obtained from the moments the phase-space masses $\mathscr{M}_\delta$. The idea pursued in Ref. [70] is to interpret the phase-space mass $\mathscr{M}_\delta(\boldsymbol{x}_t, \boldsymbol{v}_t)$ as the volume of a phase-space neighbourhood that was transported along a trajectory $(\boldsymbol{x}_t, \boldsymbol{v}_t)$, and deformed by the phase-space FTLEs. Since trajectories do not cross in phase-space, the mass contained in $\mathscr{M}_\delta(\boldsymbol{x}_t, \boldsymbol{v}_t)$ at time t must be the same as that contained in an initial phase-space ellipsoid, whose main axes had the different lengths

$(\delta \mathrm{e}^{(t_0-t)\sigma^{(1)}},\dots,\delta \mathrm{e}^{(t_0-t)\sigma^{(2d)}})$ at initial time t_0. Using this, the authors of Ref. [70] derived a relation between the rate function $I(\boldsymbol{s})$ of phase-space FTLEs and the singularity spectrum ξ_n for two-dimensional dynamical systems. By adjusting their method to our system, we obtain two relations for ξ_n in one spatial dimension:

$$\sup_{s\geq -1/2}\{(\xi_n-2n)s-I(s)\}=-(\xi_n-n),\quad |\xi_n|\geq|n| \tag{4.21a}$$

$$\sup_{s\geq -1/2}\{-\xi_n s-I(s)\}=0,\quad |\xi_n|\leq|n|. \tag{4.21b}$$

These relations can be conveniently rewritten as explicit equations for ξ_n

$$\xi_n=\begin{cases}\inf_{0\leq y<2}\{ny+J(y)\}, & |\xi_n|\geq|n|\\ \inf_{0\leq y<1}\left\{\frac{J(y)}{1-y}\right\}, & \text{otherwise}.\end{cases} \tag{4.22}$$

where

$$J(y)=I\left[\frac{y-1}{2-y}\right](2-y). \tag{4.23}$$

Equations (4.22) and (4.23) show that ξ_n can be computed directly from the rate function of phase-space FTLEs, and thus from the local properties of transient stretchings or compressions of phase-space neighbourhoods at large but finite times. Note that for small n, the first condition in Eq. (4.22) for ξ_n reduces to $\xi_n\sim n y_{\min}$, where $J(y_{\min})=0$. Using Eq. (4.23), we infer for $n\ll 1$

$$\xi_n\sim n\left(1+\frac{\lambda_1}{\lambda_1+1}\right)=n\left(1+\frac{\lambda_1}{|\lambda_2|}\right). \tag{4.24}$$

Together with Eq. (4.3) this implies that $D_1=1+\lambda_1/|\lambda_2|$ in $d=1$. This shows that one recovers the Kaplan-Yorke formula (4.20) for D_1 from Eqs. (4.21).

To conclude, the small-scale properties of the phase-space measure μ_t are characterised by the Renyi dimension D_q. The commonly used numerical methods to determine D_q are global. This means that they require, at least approximately, the knowledge of the phase-space measure μ_t in the entire phase-space. Local observables, relying on the evaluation of the tangent flow along trajectories can be computed more efficiently. The phase-space FTLEs determine the transient statistics of stretchings or contractions of phase-space neighbourhoods. Interestingly, the rate function $I(\boldsymbol{s})$ of phase-space FTLEs allows to compute the Renyi dimension. Unfortunately, the rate function $I(\boldsymbol{s})$ is often still hard to compute numerically, because it depends sensitively on large fluctuations of $\boldsymbol{\sigma}_t$ whose probability is exponentially suppressed. In Chapter 5 and Paper C, I show that in the one-dimensional white-noise limit, one can compute $I(s)$ accurately by an operator method. Equation (4.22) is then a valuable tool, that enables us to compute D_q with high accuracy.

PART III
MY WORK

In this third part of my thesis, I give a summary of the work that I have done in the course of four years as a doctoral student. Most of my research is on the statistical model for heavy particles in turbulence in one spatial dimension.

I present the main contents of the papers A-C. Apart from these articles, I have (co-)authored two additional papers that I discuss in my Licentiate thesis [1]. I have split up the discussion of the papers A-C into four chapters, ordered not chronologically but according to how their content fits into the thesis. The third part of the thesis is organised as follows:

Chapter 5 contains my work on the Renyi dimensions in the one-dimensional white-noise model. This chapter contains results from papers A and C. I show how to compute the rate function $I(s)$ of the phase-space FTLEs introduced in Section 4.2. From this rate function, I obtain the Renyi dimensions using Eqs. (4.22) and (4.3). After that, I discuss the non-analytical structure of the phase-space correlation dimension D_2 in the limit of small white-noise parameter, $\varepsilon \ll 1$.

In Chapter 6, I explain how spatial clustering is affected by folds of the phase-space distribution over configuration space. The results of this chapter are contained in Paper C. I show how the spatial projection of local phase-space neighbourhoods is applied in order to compute the rate function $\hat{I}(s)$ of the spatial FTLE in one spatial dimension. This spatial rate function $\hat{I}(s)$ is partly identical to the phase-space rate function $I(s)$ calculated in Chapter 5, but acquires a universal linear part for negative parameter values.

Chapter 7 deals with the one-dimensional persistent limit of the statistical model. This chapter describes the results of Paper B. I discuss how particles accumulate in the vicinity of long-lived traps in this limit. This trapping allows us to solve the model analytically in one spatial dimension.

Finally, I describe in Chapter 8 the relative dynamics of suspensions of heavy particles with different Stokes numbers, the subject of Paper A. In this chapter, I show that the particle dispersion in phase-space of a particle pair with different Stokes numbers exhibits two different regimes. The first regime is diffusive and leads to a plateau in the steady-state distribution of phase-space separations. In the second regime, the relative particle dynamics is that of a pair of identical particles, with an effective Stokes number $\bar{\mathrm{St}}$. This leads to a power-law scaling of the steady-state distribution at large phase-space separations.

5 Phase-space Renyi dimensions

As a substantial part of my work, I used operator methods to study the fractal small-scale structure of the phase-space measure μ_t in the one-dimensional white-noise limit. In Paper C, I employed the relation (4.22) between the rate function $I(s)$ of phase-space FTLEs $\boldsymbol{\sigma}_t$ and the singularity spectrum ξ_n, to compute the Renyi dimension D_q to high precision. In Paper A I applied a matched asymptotic expansion to derive an asymptotic, non-analytic expression for the phase-space correlation dimension D_2 for small white-noise parameter $\varepsilon \ll 1$. I summarise these results in this chapter, and give a little more detail in places where the corresponding explanations in the papers are brief.

5.1 Phase-space rate function

In the one-dimensional white-noise limit, the closed evolution equations Eqs. (3.22) for the eigenvectors and eigenvalues of the left Cauchy-Green tensor $\mathbb{B}_t$ allow us to compute the rate function $I(s)$ explicitly. I now summarise how this calculation is carried out.

In the white-noise limit, the dynamics of the phase-space neighbourhood (the tangent flow) is independent of the dynamics of the reference trajectory. The matrix $\mathbb{W}_t$ in Eq. (3.23) takes the simple form

$$\mathbb{W}_t = \begin{pmatrix} 0 & 1 \\ A_t & -1 \end{pmatrix}. \tag{5.1}$$

Here, the one-dimensional fluid-velocity gradient matrix $\mathbb{A}_t$ is given by a scalar Gaussian white-noise A_t with zero mean and correlation function

$$\langle A_t A_{t'} \rangle = 2\varepsilon^2 \delta(t-t'). \tag{5.2}$$

Furthermore, because the phase-space is two-dimensional in $d = 1$, the phase-space eigenvectors $\boldsymbol{e}_t^{(1)}$ and $\boldsymbol{e}_t^{(2)}$ of $\mathbb{B}_t$ can be parameterised by a single angle α_t. We write

$$\boldsymbol{e}_t^{(1)} = \begin{pmatrix} \cos\alpha_t \\ \sin\alpha_t \end{pmatrix}, \quad \text{and} \quad \boldsymbol{e}_t^{(2)} = \begin{pmatrix} -\sin\alpha_t \\ \cos\alpha_t \end{pmatrix}. \tag{5.3}$$

Using the evolution equations (3.22) one obtains the following stochastic equations for α_t and for the phase-space FTLE $\sigma_t^{(1)}$:

$$\tfrac{\mathrm{d}}{\mathrm{d}t}\alpha_t = -\sin\alpha_t(\sin\alpha_t + \cos\alpha_t) + \cos^2\alpha_t A_t\,, \tag{5.4a}$$

$$\sigma_t^{(1)} = \frac{1}{t-t_0}\int_{t_0}^{t} \mathrm{d}t' \tan\alpha_{t'} + \frac{1}{t-t_0}\int_0^t \mathrm{d}\alpha_{t'} \tan\alpha_{t'}\,, \tag{5.4b}$$

$$\sigma_t^{(2)} = -\sigma_t^{(2)} - 1\,. \tag{5.4c}$$

The stochastic differential equation (5.4a) and the stochastic integral in Eq. (5.4b) must be interpreted in the Stratonovich sense. Because the dynamics of α_t is invariant under the shift $\alpha_t \to \alpha_t + k\pi$, $k \in \mathbb{Z}$, we equip α_t with periodic boundary conditions on $[-\pi/2, \pi/2)$. Equations (5.4) parameterise the evolution of a local phase-space neighbourhood in the one-dimensional white-noise limit. The parameterisation is shown in Fig. 5.1, see also Fig. 4.2. The two phase-space FTLEs $\sigma_t^{(1)}$ and $\sigma_t^{(2)}$ determine the deformation of the neighbourhood along their main axes, the angle α_t gives the orientation of the major axis with respect to configuration space.

From Eqs. (5.4) we can calculate the rate function $I(s)$ of the phase-space FTLE $\sigma_t^{(1)}$. To this end, we first transform the process for the angle α_t into the new process $Z_t = \tan\alpha_t = \delta v_t/\delta x_t$, known as the particle-velocity gradient [17]. This process has been studied extensively in the context of heavy particles in turbulence [21, 78, 94, 95], but also in acoustics [96]. The infinitesimal generator $\mathscr{L}$ of the particle-velocity gradient Z_t is given by

$$\tfrac{\mathrm{d}}{\mathrm{d}t}\langle f(Z_t)\rangle = \langle \mathscr{L} f(z)\rangle\,. \tag{5.5}$$

The generator $\mathscr{L}$ is a differential operator, acting on functions of the process Z_t. It is the adjoint of the Fokker-Planck operator $\mathscr{L}^\dagger$. Explicitly, $\mathscr{L}$ and $\mathscr{L}^\dagger$ read

$$\mathscr{L} = (z+z^2)\tfrac{\mathrm{d}}{\mathrm{d}z} + \varepsilon^2\tfrac{\mathrm{d}^2}{\mathrm{d}z^2}\,, \quad \text{and} \quad \mathscr{L}^\dagger = -\tfrac{\mathrm{d}}{\mathrm{d}z}(z+z^2) + \varepsilon^2\tfrac{\mathrm{d}^2}{\mathrm{d}z^2}\,. \tag{5.6}$$

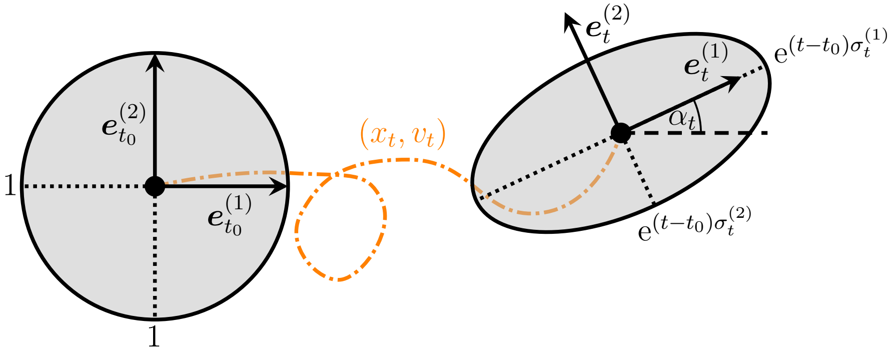

Figure 5.1: Evolution of a two-dimensional phase-space neighbourhood. An initial disc is deformed and rotated into an ellipse with axis lengths given by the phase-space FTLEs $\sigma_t^{(1)}$ and $\sigma_t^{(2)}$. The main axis is rotated by the angle α_t. The vectors $\boldsymbol{e}_t^{(1)}$ and $\boldsymbol{e}_t^{(2)}$ denote the eigenvectors (5.3) of the left Cauchy-Green tensor $\mathbb{B}_t$. The reference trajectory is shown as the orange, dash-dotted line.

The generator $\mathscr{L}$ and its adjoint $\mathscr{L}^\dagger$ determine the time-evolution of statistical averages of the process Z_t, such as its density and the moments. The generator $\mathscr{L}$ is in general not Hermitian, so that its left and right eigenfunctions do not coincide.

The *tilted* generator $\mathscr{L}_k$ [97, 98], on the other hand, is associated with statistical quantities of observables of the process Z_t. In general, an observable A_t of Z_t is defined in terms of the integrals [97, 98, 99]

$$A_t = \frac{1}{t-t_0}\int_{t_0}^{t} \mathrm{d}t' f(Z_{t'}) + \frac{1}{t-t_0}\int_{t_0}^{t} \mathrm{d}Z_{t'} g(Z_{t'}), \tag{5.7}$$

where f and g are functions of the process Z_t. As before, the stochastic integral in Eq. (5.7) must be interpreted according to the Stratonovich convention [52, 64]. In the case we consider here, the observable is the phase-space FTLE given in Eq. (5.4b). By transforming Eq. (5.4b) into an equation for Z_t, and by comparison with Eq. (5.7), we find that $f(z) = z$ and $g(z) = z/(z^2+1)$. Using the so-called Feynman-Kac formula [100], one can then show [97] that the moment generating function $G(z,t) = \langle \mathrm{e}^{(t-t_0)kA_t} | Z_{t_0} = z\rangle$, conditioned on the initial value $Z_{t_0} = z$ of the process Z_t, obeys the differential equation

$$\partial_t G(z,t) = \mathscr{L}_k G(z,t), \tag{5.8}$$

where $\mathscr{L}_k$ is the tilted generator. The form of the tilted generator depends on the functions f and g in Eq. (5.7), and on the underlying process. Its general form can be found in Refs. [97, 98]. For the particle-velocity gradient Z_t with observable (5.4b) the tilted generator $\mathscr{L}_k$ is given by

$$\mathscr{L}_k = (z^2+1)^{k/2}\mathscr{L}(z^2+1)^{-k/2} + kz\,. \tag{5.9}$$

Note that for $k=0$ we recover the generator of the process, $\mathscr{L}_{k=0} = \mathscr{L}$. Similarly to the generator $\mathscr{L}$, the tilted generator $\mathscr{L}_k$ is not Hermitian. For long times, $G(z,t)$ grows exponentially with the largest eigenvalue of $\mathscr{L}_k$. Importantly, by comparison with Eq. (4.18) we find that this largest eigenvalue of $\mathscr{L}_k$ must be equal to the scaled cumulant-generating function (SCGF) $\Lambda(k)$ of the phase-space FTLE $\sigma_t^{(1)}$ [97, 98]:

$$\Lambda(k) = \lim_{t\to\infty}\frac{1}{t-t_0}\log\left\langle \mathrm{e}^{k(t-t_0)\sigma_t^{(1)}}\right\rangle. \tag{5.10}$$

Hence, the SCGF $\Lambda(k)$ can be obtained by computing the leading eigenvalue of the tilted generator (5.9). This link provides a powerful tool for calculating the SCGF $\Lambda(k)$. The tilted generator approach admits the use of analytic methods such as perturbation theory, and different numerical methods, to calculate $\Lambda(k)$. Once $\Lambda(k)$ is obtained, the rate function $I(s)$ can be obtained by a Legendre transform, as described in Section 4.2. The tilted generator is not Hermitian, so we need to consider the two eigenvalue equations

$$\mathscr{L}_k l_k(z) = \Lambda(k) l_k(z)\,, \qquad \mathscr{L}_k^\dagger r_k(z) = \Lambda(k) r_k(z)\,, \tag{5.11}$$

where $l_k(z)$ and $r_k(z)$ are the left and right eigenfunctions of $\mathscr{L}_k$, respectively. The leading eigenvalue $\Lambda(k)$ is typically unique and real. In Paper C we solved the eigenvalue equations (5.11) numerically by a shooting method [23, 24]. The results of this method are shown in Figure 6 of that paper. An important property of the phase-space rate function $I(s)$ and of the scaled cumulant-generating function $\Lambda(k)$ are the relations

$$\Lambda(k-1) - \Lambda(-k-1) = -k\,, \tag{5.12a}$$

$$I(s-1/2) - I(-s-1/2) = -2s\,. \tag{5.12b}$$

These equations can be derived directly from a symmetry of the tilted generator, as explained in Appendix D of Paper C. They follow from a hidden time-reversal invariance of the equation of motion Z_t, as described in Appendix E of Paper C. In non-equilibrium statistical mechanics, relations like Eqs. (5.12) are called 'fluctuation relations' [101, 102, 103, 104, 105, 106, 107, 108]. In recent years, there has been growing interest in fluctuation relations since they are some of the few exact results that can be formulated for general classes on non-equilibrium systems.

In the present case, the relations (5.12) describe a symmetry between the occurrences of positive and negative phase-space FTLEs. That is, there is a strict relation between the probabilities of stretching along the $\boldsymbol{e}_t^{(1)}$ direction ($\sigma_t^{(1)} > 0$, $\sigma_t^{(2)} < -1$), and stretching along the $\boldsymbol{e}_t^{(2)}$ direction ($\sigma_t^{(1)} < -1$, $\sigma_t^{(2)} > 0$). In Eq. (5.12b) we see that $I(s)$ has an inflection point at $s = -1/2$ [82], which marks the case of isotropic contraction of the phase-space neighbourhood along both directions $\sigma_t^{(1)} = \sigma_t^{(2)} = -1/2$. In Paper C, we show that the inflection point in the rate function $I(s)$ occurs at zero when the dynamics is conservative.

5.2 Renyi dimensions

The tilted generator approach allows us, in principle, to obtain the rate function $I(s)$ to arbitrary accuracy. Once $I(s)$ is calculated, we can use the link between $I(s)$ and ξ_n discussed in Section 4.3 to compute the singularity spectrum ξ_n, and thus the phase-space Renyi dimension D_q. This way, we circumvent the global numerical methods that I described in Section 4.1, and obtain D_q very accurately. To determine ξ_n, we first compute $J(y)$ given in Eq. (4.23),

$$J(y) = I\left[\frac{y-1}{2-y}\right](2-y), \tag{5.13}$$

and then calculate ξ_n from Eq. (4.22):

$$\xi_n = \begin{cases} \inf_{0\le y<2}\{ny + J(y)\}, & |\xi_n| \ge |n| \\ \inf_{0\le y<1}\left\{\frac{J(y)}{1-y}\right\}, & \text{otherwise}. \end{cases} \tag{5.14}$$

The result for ξ_n is shown in Fig. 5.2(a), and in Figure 7(a) of Paper C. We observe that ξ_n is a concave function that levels off to ξ_∞ at a critical value n_{crit}. For small ε the transition from the increasing part to the saturation is non-smooth. For larger ε, on the other hand, the transition is smooth and

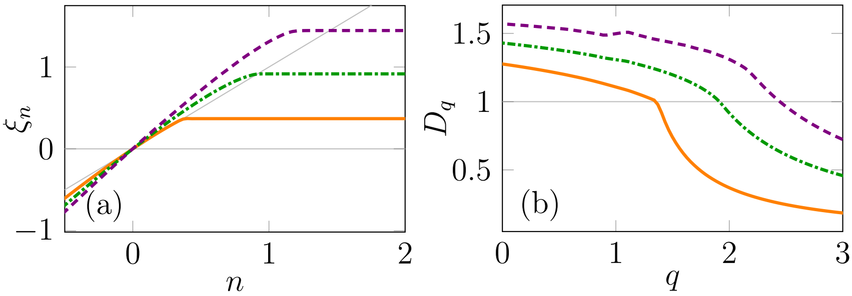

Figure 5.2: Singularity spectrum ξ_n and Renyi dimension spectrum D_q in the one-dimensional white-noise model for $\varepsilon = 2, 4, 8$, plotted as the solid, dash-dotted and dashed lines, respectively. (a) Singularity spectrum ξ_n plotted as a function of n. The light grey lines show $\xi_n = 0$ and $\xi_n = n$. (b) Renyi dimension D_q plotted as a function of q. The light grey line shows $D_q = 1$.

occurs earlier, at $n_{\rm crit} < n$. These two regimes are separated by a critical value $\varepsilon_{\rm crit} \approx 4.548$.

The Renyi dimension D_q is computed from ξ_n using Eq. (4.3). The results are shown in Fig. 5.2(b). As expected, D_q is a non-increasing function of q [72]. The non-smooth transition of ξ_n at $n_{\rm crit}$ manifests itself in a non-smooth transition of D_q from $D_q > 1$ to $D_q < 1$. This transition occurs at the light grey line in Fig. 5.2 when $\varepsilon < \varepsilon_{\rm crit}$. The results for ξ_n and D_q in Fig. 5.2 confirm that phase-space clustering of inertial particles in the one-dimensional statistical model is multifractal. This was conjectured on the basis of numerical simulations [59], and because of the discrepancy between the Renyi dimensions D_1 and D_2 [17, 74, 75].

Our results for the phase-space fractal dimensions of the one-dimensional statistical model in the white-noise limit show that the phase-space measure μ_t has an intricate, multifractal structure. The methods that I described in this section allow to compute the Renyi dimension D_q which characterise μ_t to high accuracy.

5.2.1 Correlation dimension for small ε

The correlation dimension D_2 is of particular importance for the physical applications, because it determines the scaling of the probability (4.1) of finding two particles close-by in phase-space. In Paper A we consider the scaling (4.1) for small white-noise parameter $\varepsilon \ll 1$. So far, we have interpreted all Renyi dimensions as properties of the phase-space measure μ_t. In order for the attractor $\mathscr{F}_t$ to be a fractal, the dynamics needs to be chaotic, and thus to have a positive largest Lyapunov exponent $\lambda_1 > 0$. As I explained in Section 4.2, λ_1 is negative in one-dimensional white-noise model for $\varepsilon < \varepsilon_{\rm pc} \approx 1.33$, within the path-coalescence regime [76, 77]. In this regime, the phase-space dynamics contracts to a point, and the Renyi dimensions are therefore, strictly speaking, all equal to zero, $D_q = 0$. One can, however, adopt a somewhat wider definition of the correlation dimension D_2 which allows it to be *negative* when $\lambda_1 < 0$.

Assume there exists a small-scale cutoff R_c which prevents the phase-space dynamics from contracting to a point. Physically, this cutoff can be provided by, e.g., Brownian motion [86], but also by a finite particle size or, as in Paper A, a difference in the Stokes numbers between two particle species. The idea is to consider, in the presence of the cutoff R_c, the scaling of the cumulative probability distribution $P(\mathscr{R}_t \le \delta)$ of phase-space separations $\mathscr{R}_t = |\boldsymbol{R}_t|$ in the intermediate regime $R_c \ll \delta \ll 1$. The scaling in the intermediate regime is of the form (4.1) so that one finds two scaling regimes

$$P(\mathscr{R}_t \le \delta) \sim \begin{cases} \delta^{2d}, & \delta \ll R_c\,, \\ \delta^{D_2}, & R_c \ll \delta \ll 1\,, \end{cases} \tag{5.15}$$

Interestingly, the correlation dimension D_2 can be defined in this way both for $\lambda_1 > 0$ and $\lambda_1 < 0$. In the latter case, D_2 becomes negative [109]. Equation (5.15) shows that even a negative D_q can be physically relevant as it describes the scaling of separations in an intermediate regime.

After this discussion, I now outline how we calculate D_2 in one spatial dimension in the limit $\varepsilon \to 0$. More details on the precise asymptotic expansion can be found in the supplemental material of Paper A. Note again that $\lambda_1 < 0$ for $\varepsilon \ll 1$, so that D_2 should be negative. Similarly to $\Lambda(k)$ in Eq. (5.11) we can express D_2 as the generalised eigenvalue of the generator $\mathscr{L}$ of Z_t [23, 24], defined in Eq. (5.6):

$$\mathscr{L}\, l(z) = D_2 z\, l(z)\,, \quad \text{and} \quad \mathscr{L}^\dagger r(z) = D_2 z\, r(z)\,. \tag{5.16}$$

The functions l and r are the generalised left and right eigenfunctions, respectively. The standard strategy to solve these equations for small ε is to rescale the z-coordinate, $z \to \varepsilon z$, and expand l, r and D_2 perturbatively in ε. More precisely, one makes the ansatz $l = l^{(0)} + \varepsilon l^{(1)} + \ldots$, $r = r^{(0)} + \varepsilon r^{(1)} + \ldots$

and $D_2 = D_2^{(0)} + \varepsilon D_2^{(1)} + \ldots$ and solves the corresponding equations iteratively, order for order in ε. This standard approach, however, fails for Eqs. (5.16) [74, 75, 109]. The standard perturbation theory gives $D_2^{(0)} = -1$, and $D_2^{(n)} = 0$ for all $n > 0$, leading to the perturbative result

$$D_2 \sim -1\,, \tag{5.17}$$

to all perturbative orders in ε. First of all, this result suggests that the correlation dimension is negative in the limit $\varepsilon \to 0$. The negative correlation dimension gives the scaling of the probability $P(\mathscr{R}_t \le \delta)$ in the presence of a cutoff R_0 in the intermediate regime $R_0 \ll \delta \ll 1$, as given in Eq. (5.15). Since the correlation dimension D_2 must be positive for $\varepsilon > \varepsilon_{\rm pc}$, Eq. (5.17) can clearly not be the solution for D_2 for all ε.

The reason for this discrepancy is that the perturbation problem in Eqs. (5.16) is singular, and it needs to be solved with methods of singular perturbation theory [110]. Singular perturbation theory allows for solutions of the generalised eigenvalue D_2, that are non-perturbative, and thus do not have the form of a series expansion in powers of ε.

The starting point for the method that we use in Paper A is to note that there exists an exact solution to Eqs. (5.16) for $D_2 = -1$ that is valid for all ε. This solution, however, does not satisfy the required boundary conditions for the generalised eigenfunctions l and r. Using this solution, we reduce second order differential equations in Eqs. (5.16) to first order differential equations, using the method of reduction of order [110]. The next step is to expand $D_2 = -1 + \delta D_2$, where $\delta D_2 \to 0$ as $\varepsilon \to 0$. The crucial third step is to make a regular perturbative expansion of the generalised eigenfunctions in δD_2. Requiring that these eigenfunctions satisfy the boundary conditions then determines δD_2. To lowest non-vanishing order we find $\delta D_2 \sim \pi^{-1} {\rm e}^{-1/(6\varepsilon^2)}$, and thus

$$D_2 \sim -1 + \frac{1}{\pi} {\rm e}^{-1/(6\varepsilon^2)}\,. \tag{5.18}$$

Apart from the actual result, the calculation leading to Eq. (5.18) shows that we need to take into account the algebraic tails of the generalised eigenfunctions l and r, that are related to the caustic escapes $Z_t \to -\infty$ in the Z_t-dynamics. I discuss these events in more detail in Chapter 6. These tails are absent in the standard perturbative expansions of l and r. This suggests that the non-perturbative contribution in Eq. (5.18) is related to occurrence of caustics in the dynamics.

The result (5.18) allows an insight into the non-analytical structure of the correlation dimension D_2 at small ε. The eigenvalue splitting δD_2 between the unphysical solution with $D_2=-1$ and the physical solution with Eq. (5.18) is reminiscent of the instanton contributions to the energy splitting of a quantum particle in a double-well potential [111]. In this case, the energies are given by a so-called trans-series expansion [112] in terms of the perturbation parameter, thus generalising the standard perturbation expansion. In Paper A, see also [113], we speculate that D_2 may also have a representation in terms of such a trans-series, in which caustics play a similar role as the instantons in the quantum mechanical double-well.

5.3 Implications of the results

All the results that I presented in this chapter were obtained for the one-dimensional statistical model in the white-noise limit. Therefore, they are probably not particularly interesting from an experimental point of view. In my opinion, however, these results showcase the complexity of the phase-space dynamics in one spatial dimension. From a technical perspective they show the power of operator methods for the calculation of the Renyi dimensions in the statistical model. Physically, the result (5.18) show that the caustic excursions $Z_t \to -\infty$ play an essential role in the dynamics, and that they have an impact on clustering in phase space. The non-perturbative nature of these caustics makes it difficult to deal with them in perturbative expansions. I discuss this aspect in detail in Chapter 6. In higher dimensions, it was shown that perturbative expansions fail to describe numerical results for the phase-space correlation dimension D_2 at finite inertia parameters [17, 74, 75, 79]. The reason could be non-perturbative contributions similar to that in Eq. (5.18).

6 Fractal catastrophes

Phase-space clustering is an important property of the statistical model of heavy particles in turbulence. As I explained in Secs. 3.1 and 4.2, the dissipative nature of the phase-space dynamics (3.1) together with chaotic dynamics ($\lambda_1 > 0$) leads to the formation of a fractal attractor $\mathscr{F}_t$ that is sampled inhomogeneously by the phase-space dynamics. The small-scale properties of the phase-space measure μ_t are quantified by the phase-space Renyi dimension D_q. The inhomogeneous distribution of heavy particles in phase-space is known as phase-space clustering.

If we want to measure phase-space clustering in an experiment, we must determine the phase-space density $\varrho_{t,t_0}(\boldsymbol{x},\boldsymbol{v})$ of particles in the long-time limit. This is often not possible if an experimental apparatus, for instance, only allows us to make time-isolated snapshots of the positions of particles, with no reference to momentary velocities. An illustration of such a case is shown in Fig. 6.1. The subfigures (a)-(c) show snapshots of the evolution of the particle density in two spatial dimensions $d=2$, obtained from statistical model simulations. In $d=2$, phase-space is four dimensional, but the snapshots are taken only of the two-dimensional spatial domain. Figures 6.1(a), (b) and (c) correspond to snapshots at times $\Delta t = t - t_0 = 1, 3, 5$, respectively.

In cases like this, we only have access to the spatial distribution of particles, determined by the spatial density $\hat{\varrho}_{t,t_0}(\boldsymbol{x})$, the marginal density of the phase-space density ϱ_{t,t_0}:

$$\hat{\varrho}_{t,t_0}(\boldsymbol{x}) = \int \mathrm{d}\boldsymbol{v}\, \varrho_{t,t_0}(\boldsymbol{x},\boldsymbol{v}), \tag{6.1}$$

We can interpret the spatial density $\hat{\varrho}_{t,t_0}$ as arising from the projection of the phase-space locations of particles to configuration space, $(\boldsymbol{x},\boldsymbol{v}) \mapsto \boldsymbol{x}$. The projection is not in general one-to-one, because any position in configuration space may be occupied by many particles, with very different velocities. This observation has interesting consequences for the spatial density $\hat{\varrho}_{t,t_0}$: In Fig. 6.1(a), we observe an increased particle density on line-like sets that emerge from singular points. These singularities are the consequence of the spatial projection of folds in the phase-space particle distribution, known as caustics. In optics, caustics are singularities in the light intensity arising from random, partial focussing of rays. On the bottom of a swimming pool

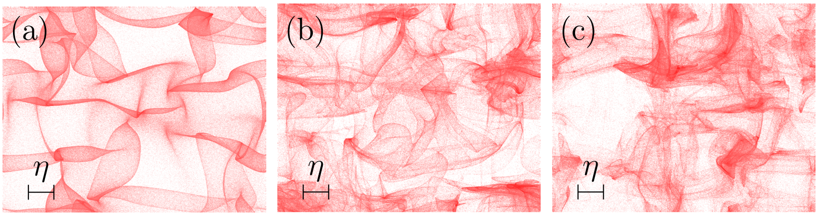

Figure 6.1: Spatial particle density $\hat{\varrho}_{t,t_0}$ for the two-dimensional statistical model in the white-noise limit with $\varepsilon = 1.5$ and $\wp = 0$ at different times $\Delta t = t - t_0$. The density is obtained from evolving $2 \cdot 10^7$ particles. (a) $\hat{\varrho}_{t,t_0}$ for $\Delta t = 1$. (b) $\hat{\varrho}_{t,t_0}$ for $\Delta t = 3$. (c) $\hat{\varrho}_{t,t_0}$ for $\Delta t = 5$.

on a sunny day [22, 25], light is diffracted randomly by the water surface and focused on line-like sets [25], similar to the ones we see in Fig. 6.1(a).

In Paper C we ask the question how these caustic folds affect the spatial density $\hat{\varrho}_{t,t_0}$, and thus the spatial clustering of particles. It is generally assumed that caustics increase spatial clustering [21], but it is not precisely clear how to quantify this expectation. In Paper C we quantify the effect of caustics in terms of the projection of local spatial neighbourhoods. In the following, I review our analysis of spatial clustering in Paper C.

6.1 Spatial density

The spatial density is obtained from integrating the phase-space density ϱ_{t,t_0} over the velocities, Eq. (6.1). If the maximum Lyapunov exponent is positive $\lambda_1 > 0$, the dynamics is chaotic and we expect ϱ_{t,t_0} to approach the singular phase-space density $\bar{\varrho}_t$, with associated phase-space measure μ_t in the limit $t_0 \to -\infty$. Similarly to the discussion in Section 3.1 we define the limiting (and possibly singular) spatial density

$$\hat{\bar{\varrho}}_t(\boldsymbol{x}) = \lim_{t_0 \to -\infty} \int \mathrm{d}\boldsymbol{v}\, \varrho_{t,t_0}(\boldsymbol{x}, \boldsymbol{v})\,. \tag{6.2}$$

The associated spatial measure $\hat{\mu}_t$ of an arbitrary spatial set $\hat{\mathscr{S}}$ reads

$$\hat{\mu}_t(\hat{\mathscr{S}}) = \int_{\hat{\mathscr{S}}} \mathrm{d}\hat{\mu}(\boldsymbol{x}) \equiv \lim_{t_0 \to -\infty} \int_{\hat{\mathscr{S}}} \mathrm{d}\boldsymbol{x} \int \mathrm{d}\boldsymbol{v}\, \varrho_{t,t_0}(\boldsymbol{x}, \boldsymbol{v})\,. \tag{6.3}$$

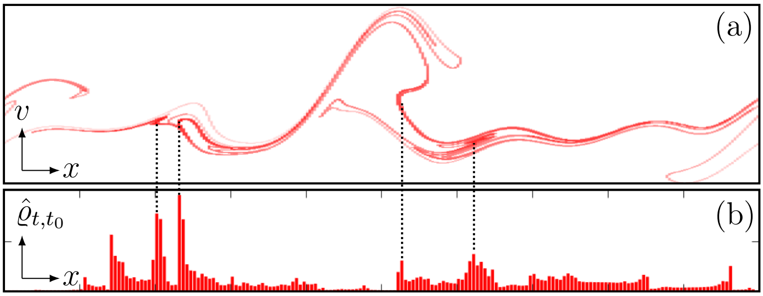

Figure 6.2: Comparison of the phase-space density ϱ_{t,t_0} and the spatial density $\hat{\varrho}_{t,t_0}$ in $d = 1$ for $\Delta t = t - t_0 = 50$, obtained from simulations of the one-dimensional white-noise limit with $\varepsilon = 1.5$ and 10^7 particles. (a) Phase-space density ϱ_{t,t_0}. The position is plotted horizontally, the velocity vertically. The logarithmic colour coding shows the magnitude of ϱ_{t,t_0}. (b) Corresponding spatial density $\hat{\varrho}_{t,t_0}(x)$ plotted against the position x. Large spatial particle concentrations can be observed in the vicinity of folds, exemplified by the dotted lines.

The spatial density $\hat{\bar{\varrho}}_t(\boldsymbol{x})$ is then the density associated with the differential spatial measure $\mathrm{d}\hat{\mu}_t(\boldsymbol{x})$

$$\mathrm{d}\hat{\mu}_t(\boldsymbol{x}) = \hat{\bar{\varrho}}_t(\boldsymbol{x})\mathrm{d}\boldsymbol{x}\,, \tag{6.4}$$

interpreted in the sense of distributions.

Figure 6.2 illustrates the connection between the phase-space density ϱ_{t,t_0} and the spatial density $\hat{\varrho}_{t,t_0}$ in one spatial dimension after a long time. Here, ϱ_{t,t_0} and $\hat{\varrho}_{t,t_0}$ are approximations of the infinite-time densities $\bar{\varrho}_t$ and $\hat{\bar{\varrho}}_t$, respectively. Fig. 6.2(a) shows the phase-space density of the one-dimensional model, Fig. 6.2(b) shows the corresponding $\hat{\varrho}_{t,t_0}$. We observe that the spatial density $\hat{\varrho}_{t,t_0}$ is strongly inhomogeneous, similarly to the phase-space density. Furthermore, the spatial density exhibits peaks in regions where the phase-space density folds over configuration space. This is exemplified by the dotted lines in Fig. 6.2. At the edges of these folds, the integral in Eq. (6.1) accumulates infinitesimal neighbourhoods of the phase-space density in single points in configuration space. This leads to the divergencies in $\hat{\varrho}_{t,t_0}$, which are the caustics in the one dimensional statistical model.

Comparing Fig. 6.2 to Fig. 6.1 we note that the caustic singularities in $d = 1$ are singular points instead of lines emerging from points in $d = 2$.

For all finite times, this can be explained in terms of catastrophe theory [114, 115]. In catastrophe theory, the folds observed in $d = 1$ and $d = 2$ are called catastrophes, which can be categorised into so-called normal forms according to their co-dimension. In $d = 1$ and $d = 2$ only the so-called cuspoids [25, 114] are structurally stable. Cuspoids have co-dimension one, so they are one dimensional (fold lines) in $d = 2$ and zero dimension (single points) in $d = 1$. The fold lines in $d = 2$ emerge from singular points, so-called cusp points [114], as we observe in Figs. 6.1(a). For longer times [Figs. 6.1(b) and (c)], caustics have led to the formation of many branches of particles in phase space, which makes it harder to identify new caustics in these figures. This is analogous to the one-dimensional case in Fig. 6.2(a), where we observe a large number of phase-space branches lying on top of each other.

After long times, the phase-space density is supported by a fractal set, and the associated folds are the folds of a fractal attractor. In Paper C we therefore call these folds 'fractal catastrophes', due to their fractal nature in the long-time limit. Figures 6.1 and 6.2 seem to suggest that fractal catastrophes lead to an increase in the spatial density.

6.2 Projection formula for spatial Renyi dimension

The small-scale structure of spatial measure $\hat{\mu}_t$ can be characterised by a family of spatial Renyi dimensions $\hat{D}_q$. We can estimate the spatial Renyi dimensions numerically by using the box-counting methods that I described in Section 4.1. As the spatial natural measure is obtained from a projection, however, it is tempting to use known results for the projection of fractals [116] to compute the fractal properties of the spatial measure $\hat{\mu}_t$ from the phase-space measure μ_t. Projection formulas relate the Renyi dimension D_q of a multifractal measure in a higher-dimensional space (phase-space) to the corresponding $\hat{D}_q$ in the lower dimensional projected space (configuration space). It was shown in Refs. [117], that for generic multifractal measures the projected Renyi dimension $\hat{D}_q$ obeys the formula

$$\hat{D}_q = \min\{D_q, d\}, \tag{6.5}$$

for $q \in [0,2]$. Equation (6.5) holds for 'typical' projections of the measure to lower-dimensional subspaces. Since our dynamics, Eq. (3.1), is non-isotropic in phase-space, there is, a priori, no reason to believe that the projection to configuration space is typical. Therefore, it is not clear if we can use the projection formula Eq. (6.5) to compute the spatial Renyi dimension $\hat{D}_q$ from their phase-space counter parts D_q. In Paper C and in Section 6.5 we show that (6.5) does, in fact, hold for $q = 2$.

6.3 Spatial particle neighbourhoods and their collapse

For the analysis of the fractal structure of the phase-space measure μ_t in Chapter 5, it proved useful to analyse the local behaviour of phase-space neighbourhoods. It may therefore appear natural to do the same for the analysis of the spatial measure $\hat{\mu}_t$ in configuration space. To this end, we must project local phase-space neighbourhoods to configuration space. In this section I show how this projection is carried out. The dynamics of stretching or compression of the projected neighbourhoods is determined by d spatial finite-time Lyapunov exponents (spatial FTLEs) $\hat{\boldsymbol{\sigma}}_t = (\hat{\sigma}_t^{(1)}, \ldots, \hat{\sigma}_t^{(d)})$. Analogously to the analysis in phase-space, the cumulative sums $\sum_{i=1}^{n} \hat{\sigma}_t^{(i)}$ determine the transient fluctuations of the evolution of n-dimensional spatial (sub-)volumes. In particular, the evolution of d-dimensional spatial volumes $\hat{\mathscr{V}}_t$ is, by definition, determined by

$$\frac{\hat{\mathscr{V}}_t}{\hat{\mathscr{V}}_{t_0}} = \mathrm{e}^{(t-t_0)\hat{S}_t}, \qquad \text{with} \qquad \hat{S}_t = \sum_{i=1}^{d} \hat{\sigma}_t^{(i)}. \tag{6.6}$$

At initial time t_0 an infinitesimal d-dimensional spatial volume $\hat{\mathscr{V}}_{t_0}$ is characterised by d orthogonal unit vectors, that lie entirely in configuration space. As I explained in Section 3.2, each of these vectors is stretched and rotated by the (phase-space) deformation matrix $\mathbb{J}_t$. In the long-time limit, any d-dimensional volume must align with the first d eigenvectors $\boldsymbol{e}_t^{(i)}$, $i = 1, \ldots, d$ of the left Cauchy-Green tensor $\mathbb{B}_t$, defined in Section 3.2.1. Hence for $t > t_0$, the initial spatial volume $\hat{\mathscr{V}}_{t_0}$ evolves through phase-space, with phase-space volume $\sim \exp[(t-t_0)\sum_{i=1}^{n} \sigma_t^{(i)}]$. In configuration space, however, we observe the projection $\hat{\mathscr{V}}_t$ of the volume. In Paper C we show that this projection leads to a factorisation of the spatial volume $\hat{\mathscr{V}}_t$ into a spatial volume factor and a phase-space volume factor. We find

$$\frac{\hat{\mathscr{V}}_t}{\hat{\mathscr{V}}_{t_0}} = |\det \mathbb{O}_t^{(d)}| \mathrm{e}^{(t-t_0)\sum_{i=1}^{d} \sigma_t^{(i)}}. \tag{6.7}$$

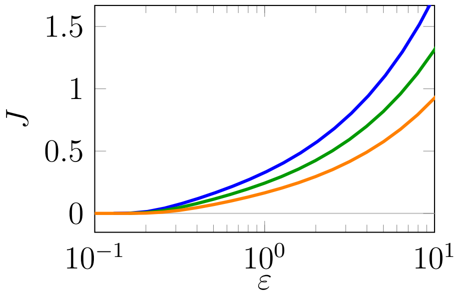

Figure 6.3: Rate of caustic formation J in the white-noise limit for different dimensions [81]. The cases $d=1$, $d=2$ and $d=3$ are shown in orange, green and blue, respectively.

Here $|\det \mathbb{O}_t^{(d)}|$ is the spatial volume factor given in terms of the $d\times d$ dimensional spatial sub-matrix of the matrix $\mathbb{O}_t$ of eigenvectors of $\mathbb{B}_t$. We have

$$\mathbb{O}_{ij}^{(d)} = \boldsymbol{e}_t^{(i)}\cdot\hat{\boldsymbol{e}}_j\,,\qquad 1\le i,j\le d\,,\tag{6.8}$$

where $\hat{\boldsymbol{e}}_i$, $i=1,\dots,d$ are the Cartesian unit vectors spanning configuration space. We call $\exp[(t-t_0)\sum_{i=1}^d\sigma_t^{(i)}]$ in Eq. (6.7) phase-space volume factor because it describes the evolution of d-dimensional volumes in phase-space. The spatial volume factor $|\det \mathbb{O}_t^{(d)}|$ is smaller than or equal to unity. It describes the collapse of spatial volumes $\hat{\mathscr{V}}_t\to 0$, when two of the projected vectors of the spatial volume become collinear, so that $|\det \mathbb{O}_t^{(n)}|\to 0$.

This collapse of spatial volumes is the local signature of the caustic singularities in the spatial density. The rate J at which caustics form along trajectories was calculated in the white-noise limit in Refs. [21, 77, 79]. The results for J in $d=1,2$ and 3 are shown in Fig. 6.3 as the orange, green and blue lines, respectively [81]. In all cases, J is an increasing function of the white-noise parameter ε. For small ε, J shows an activated behaviour $J\propto \mathrm{e}^{-S/\varepsilon^2}$, where $S=1/6$ is a constant that was conjectured to be independent of d [17]. Outside the white-noise limit, for finite Ku and St, J shows a similar activated behaviour as a function of the Stokes number St [118], but with an Ku-dependent exponent S [118].

That J has the form $J\propto \mathrm{e}^{-S/\varepsilon^2}$ implies that J is non-analytic at $\varepsilon=0$. Hence, perturbation expansions around the $\varepsilon=0$-limit do not capture the effects of caustics. The non-perturbative nature of the caustics complicates their theoretical description. This is one of the reasons why the quantitive contribution of the rate of caustic formation to spatial clustering is poorly understood. The activated behaviour of J as a function of St has been observed not only in the statistical model, but also in direct numerical simulations of heavy particles in turbulence [119].

Using Eq. (6.6) and (6.7) we find an expression for $\hat{S}_t$ in Eq. (6.6) given by

$$\hat{S}_t = \sum_{i=1}^{d} \sigma_t^{(i)} + \frac{1}{t-t_0} \log|\det \mathbb{O}_t^{(d)}| \tag{6.9}$$

When the spatial volume collapses, $\det \mathbb{O}_t^{(d)} \to 0$, $\hat{S}_t$ escapes to negative infinity. After the collapse, the spatial volume must become finite again, so that $\hat{S}_t$ jumps instantaneously from $-\infty$ to ∞.

6.4 Neighbourhoods in one spatial dimension

In one spatial dimension we study the spatial FTLE $\hat{\sigma}_t$, the one-dimensional analogue of $\hat{S}_t$. It describes the statistics of the transient stretching or contraction of one-dimensional spatial volumes, which are simply line elements. After an initial transient, a spatial line element aligns with the leading eigenvector of the leading phase-space FTLE $\boldsymbol{e}_t^{(1)}$, parameterised by the angle α_t [see Eq. (5.3) and Fig. 5.1]. In the one-dimensional version of Eq. (6.9), the spatial volume factor is simply $\det|\mathbb{O}_t^{(1)}| = \cos\alpha_t$. Figure 6.4(a) shows a typical trajectory of α_t as a function of time. We observe that α_t moves to $-\pi/2$ and reappears at $\pi/2$ at time t_c. In the event $\alpha_t = \pi/2$, the eigenvector $\boldsymbol{e}_t^{(1)}$ is perpendicular to configuration space, and the spatial volume factor vanishes, $\cos\alpha_t = 0$.

The evolution equation for the spatial FTLE $\hat{\sigma}_t$ is obtained from Eq. (5.4b), and from Eq. (6.9) with $\mathbb{O}_t^{(1)} = \cos\alpha_t$. We find

$$\hat{\sigma}_t = \frac{1}{t-t_0} \int_{t_0}^{t} \mathrm{d}t' \tan\alpha_{t'} . \tag{6.10}$$

Assume $\alpha_t \to -\pi/2$, at the caustic time t_c. In the vicinity of t_c, we can approximate $\hat{\sigma}_t$ by $\hat{\sigma}_t \sim \log(|t-t_c|)$. This shows that $\hat{\sigma}_t$ escapes to $-\infty$ at $t = t_c$ and returns to finite values for $t > t_c$. The blue curve in Fig. 6.4(b)

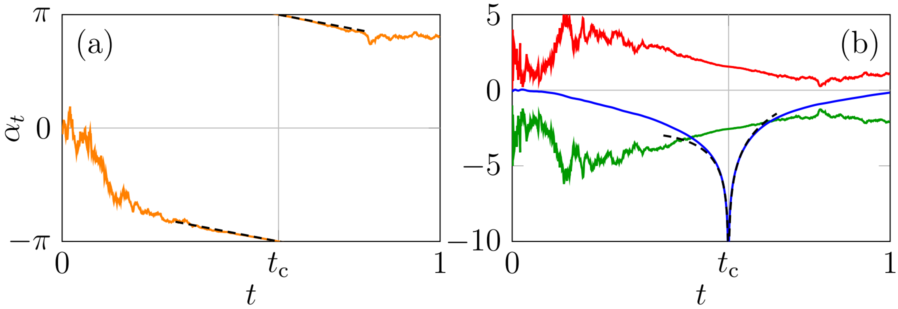

Figure 6.4: Typical trajectories of α_t and the FTLEs for the same realisation of the (white-in-time) fluid-velocity gradient A_t, obtained from evaluating Eqs. (5.4). (a) Trajectory for α_t for $\varepsilon = 2$. At the caustic time t_c, α_t jumps from $-\pi/2$ to $\pi/2$. In the vicinity of t_c, α_t is linear in time, $\alpha_t \sim \pm\pi/2 + t_c - t$ (black, dashed line) (b) Typical trajectory of the phase-space FTLEs $\sigma_t^{(1)}$ (red), $\sigma_t^{(2)}$ (green), and of the spatial FTLE $\hat\sigma_t$ (blue) corresponding to the values of α_t in (a). At the caustic time t_c, the spatial FTLE $\hat\sigma_t$ escapes to $-\infty$ and returns. In the vicinity of t_c, we have $\sigma_t \sim \log|t-t_c|^{-1}$ (black, dashed line).

shows a typical trajectory of the spatial FTLE $\hat\sigma_t$, obtained from evaluating Eq. (6.10) with the realisation of α_t given in Fig. 6.4(a). The black dashed line shows the asymptotic behaviour around the caustic time t_c. The red and green lines in Fig. 6.4(b) show the evolution the phase-space FTLEs $\sigma_t^{(1)}$ and $\sigma_t^{(2)}$, respectively, obtained from Eqs. (5.4b) with the same realisation of α_t. While the spatial FTLE $\hat\sigma_t$ escapes to negative infinity at the caustic time t_c, the phase-space FTLEs stay finite.

In order to understand why the divergence observed for spatial FTLE $\hat\sigma_t$ does not occur for phase-space FTLEs $\sigma_t^{(1)}$ and $\sigma_t^{(2)}$, we consider their equations of motion (5.4b) and (5.4c) in the vicinity of the caustic time t_c. I restate Eqs. (5.4b) and (5.4c) here for convenience:

$$\sigma_t^{(1)} = \frac{1}{t-t_0}\int_{t_0}^{t} \mathrm{d}t' \tan\alpha_{t'} + \frac{1}{t-t_0}\int_{0}^{t} \mathrm{d}\alpha_{t'} \tan\alpha_{t'}\,, \tag{6.11a}$$

$$\sigma_t^{(2)} = -\sigma_t^{(1)} - 1\,. \tag{6.11b}$$

When $\alpha \to -\pi/2$, the individual integrands in the equation for $\sigma_t^{(1)}$, Eq. (6.11a), diverge. However, as we see from Eq. (5.4a), $\mathrm{d}\alpha_t = -\mathrm{d}t$ at $\alpha_t = -\pi/2$, so that α_t transitions deterministically from $-\pi/2$ to $\pi/2$ with angular velocity -1.

The deterministic transition of α_t is shown as the dashed line in Fig. 6.4(a). This shows that the two divergencies in the integrands of Eq. (6.11a) cancel so that the phase-space FTLEs stay finite for all times.

In Paper C we show that these caustic escapes of $\hat{\sigma}_t$ leave a universal signature in the spatial rate function. I review our main results for the spatial rate function in the next section.

6.5 Large deviations of spatial FTLE

The spatial FTLE obeys a large-deviation principle with spatial rate function $\hat{I}(s)$. Analogously to the phase-space rate function $I(s)$, the spatial rate function $\hat{I}(s)$ derives from the large-deviation form

$$P_t(\hat{\sigma}_t = s) \propto \mathrm{e}^{-t\hat{I}(s)}\,, \tag{6.12}$$

after a large but finite time t. The spatial SCGF $\hat{\Lambda}(k)$ is defined by

$$\hat{\Lambda}(k) = \lim_{t\to\infty} \frac{1}{t-t_0} \log\left\langle \mathrm{e}^{(t-t_0)\hat{\sigma}_t} \right\rangle . \tag{6.13}$$

In Paper C we show that the caustic divergencies of $\hat{\sigma}_t$ shown in Fig. 6.4(b) lead to a linear part in the spatial rate function. Where exactly this linear part emerges may depend on the statistical properties of the fluid-velocity gradient A_t. In the white-noise limit, we find

$$\hat{I}(s) = \begin{cases} I(s) & s > -1/2\,, \\ -s - \Lambda(-1/2) & s \le -1/2\,. \end{cases} \tag{6.14}$$

The general case is discussed in Paper C. Equation (6.14) shows that the spatial rate function $\hat{I}(s)$ in Eq. (6.14) coincides with the phase-space rate function $I(s)$ for $s > -1/2$. For $s \le -1/2$ the rate function is linear, as a consequence of the caustic divergencies of $\hat{\sigma}_t$. In Paper C we show that although the location of the onset of the linear part in $\hat{I}(s)$ may depend on the characteristics of A_t, and on whether or not the dynamics is dissipative, the linear form is independent of these factors.

That the linear part of $\hat{I}(s)$ has a universal form can be understood by noting that $\hat{\sigma}_t$ and $\sigma_t^{(1)}$ in Eqs. (6.10) and (6.11a) agree up to the term $(t-$

$t_0)^{-1}\int_{t_0} \mathrm{d}\alpha_{t'} \tan\alpha_{t'}$, which has the form of a total derivative

$$\frac{1}{t-t_0}\int_{t_0}^{t} \mathrm{d}\alpha_{t'} \tan\alpha_{t'} = \frac{1}{t-t_0}\log|\cos\alpha_t|\,. \tag{6.15}$$

This shows that in the limit $t \to \infty$ only the divergent part $\cos\alpha_t \to 0$ of the extra term (6.15) may contribute to the large deviation form of the density (6.12). Since the excursions $\alpha_t \to -\pi/2$ are deterministic and independent of the details of A_t, these contributions must be deterministic.

The linear part in the spatial rate function $\hat{I}(s)$ and the divergence of $\hat{\Lambda}(k)$ have important consequences that I summarise in the following. More details can be found in Paper C.

First, the spatial SCGF $\hat{\Lambda}(k)$ diverges for $k \leq -1$ and is identical to the phase-space SCGF for $k > -1$:

$$\hat{\Lambda}(k) = \begin{cases} \Lambda(k), & k > -1\,, \\ \infty\,, & k \leq -1\,. \end{cases} \tag{6.16}$$

Second, the distribution of spatial separations $P(|\delta x_t| = \delta)$ is constant for $\delta < \mathrm{e}^{-t/2}$. This is in distinction to the finite-time distribution of phase-space separations $\mathscr{R}_t$, where $P(\mathscr{R}_t = 0)$ vanishes for all finite times. This finding implies that the projection lets spatial separations become zero in finite time. In phase-space on the other hand, particles come close because of the dissipative nature of the dynamics, which leads to an exponential, and thus asymptotic, approach of particles.

Third, the linear part in $\hat{I}(s)$ allows to prove the projection formula for D_2 from the linear part of the spatial rate function $\hat{I}(s)$. We find

$$\hat{D}_2 = \min\{D_2, 1\}\,. \tag{6.17}$$

Our detailed analysis in Paper C shows that the saturation of the spatial correlation dimension $\hat{D}_2$ is due to the divergence of $\hat{\Lambda}(k)$ for $k \leq -1$ in Eq. (6.16), which is a result of caustics in the dynamics. If and how caustics influence the projection formula for the Renyi dimension D_q with $q \neq 2$ is an open question.

6.6 Implications of the results and generalisations

The results described in this chapter and detailed in Paper C show how the projection from phase-space to configuration space affects the statistics of spatial FTLEs. The main result is the linear part in the spatial rate function $\hat{I}(s)$, and the corresponding divergence of the spatial SCGF $\hat{\Lambda}(k)$. The linear part was shown to be a consequence of finite-time singularities in the spatial FTLE $\hat{\sigma}_t$.

First of all, the result shows the close connection between clustering in phase-space, and in configuration space. That is, the spatial rate function $\hat{I}(s)$ agrees with the phase-space rate function $I(s)$ for $s \geq -1/2$, so that the long-time dynamics of stretchings in phase-space and in configuration space are similar. Discrepancies in the rate function occur only for strong compressions of neighbourhoods with $s < -1/2$. In configuration space the strong compression is due to caustic folds that lead to additional spatial clustering. In short, spatial neighbourhoods expand in the same way as phase-space volumes, but the way they contract is very different.

The factorisation of spatial volumes into the phase-space and spatial volume factors in Section 6.3 suggests that the one-dimensional results laid out in this chapter should generalise to the sum of spatial FTLEs in higher dimensions. Thus, we speculate that the rate function of $\hat{S}_t = \sum_{n=1}^{d} \hat{\sigma}_t^{(i)}$ has a linear part. This would suggest that the projection formula (6.17) for $\hat{D}_2$ can be generalised to higher dimensions, in accordance with the results of numerical simulations [17, 59].

Furthermore, our results for the spatial rate function are not restricted to systems with dissipation. In Paper C we consider a more general case with a variable 'damping ratio' ζ, a measure for the dissipation in the system. In this chapter, I presented the case $\zeta = -1/2$. In Paper C we obtain conservative dynamics by taking the limit $\zeta \to 0$. In such conservative systems, there is no fractal clustering. However, the caustic singularities still lead to substantial inhomogeneities in the spatial distribution of particles. The spatial rate function $\hat{I}(s)$ in conservative systems has a linear part that starts at $s = 0$ and extends to $-\infty$, and the spatial SCGF $\hat{\Lambda}(k)$ diverges for $k \leq -1$. As we argue in the Sec. 9 of Paper C, the close relation between the inertial-particle problem and random systems without dissipation could allow to relate the divergence in $\Lambda(k)$ to the analysis of the 'twinkling' of stars in optics [120].

7 Persistent limit

In the white-noise limit in one spatial dimension, many of the observables of the statistical model can be calculated analytically. The reason is that the dynamics of the neighbourhoods become independent of the dynamics of the reference trajectory, so that the equations of motion (3.8) form a Markov system. This is, however, not possible in general, because the statistical properties of the fluid-velocity gradient matrix $\mathbb{A}_t(\boldsymbol{x}_t)$ depend on the momentary particle position $\boldsymbol{x}_t$ which, in turn, depends on the history of the fluid-velocity field $\boldsymbol{u}(\boldsymbol{x},t)$. A notable exception is the persistent limit, for which analytic results can be obtained in one spatial dimension. The reasons that allow to solve the equations in this limit are, however, quite different.

In this chapter, I review the main results of Paper B. In this article, we describe how to obtain analytical results in the one-dimensional persistent limit of the statistical model. We encountered the persistent limit already in Section 2.5.3. The model describes heavy particles in a highly persistent fluid-velocity field, where the correlation time $\tau_{\rm c}$ is the largest of all time scales, $\tau_{\rm c} \gg \tau_{\rm a}, \tau_{\rm p}$.

7.1 Particle trapping

When $\tau_{\rm c}$ is much larger than both the advection time $\tau_{\rm a}$ and the particle time scale $\tau_{\rm p}$, the particles move through the fluid essentially as if the fluid-velocity field $\boldsymbol{u}(\boldsymbol{x},t)$ were constant in time. When $\boldsymbol{u}(\boldsymbol{x},t)$ is sufficiently compressible, particles can get trapped in long-lived sinks of the fluid-velocity field $\boldsymbol{u}(\boldsymbol{x},t)$. To see this, consider a fully compressible fluid-velocity field with $\wp = 1$. The equations of motion then read in dimensionless form

$$\tfrac{\mathrm{d}}{\mathrm{d}t}\boldsymbol{x}_t = \boldsymbol{v}_t\,, \qquad \tfrac{\mathrm{d}}{\mathrm{d}t}\boldsymbol{v}_t = -\boldsymbol{\nabla} U(\boldsymbol{x}_t,t) - \boldsymbol{v}_t\,, \tag{7.1}$$

where $U(\boldsymbol{x},t) = -\phi(\boldsymbol{x},t)$ and $\phi(\boldsymbol{x},t)$ is the random scalar function introduced in Chapter 2. We see from Eqs. (7.1) that $U(\boldsymbol{x},t)$ takes the role of a potential in configuration space. In the de-dimensionalisation scheme used in this thesis, time is rescaled by the particle relaxation time $\tau_{\rm p}$, as discussed in Section 2.5.1. From Eq. (2.7) and the limit (2.22) we find that the random potential $U(\boldsymbol{x},t)$ has the correlation function

$$\langle U(\boldsymbol{x},t)U(\boldsymbol{x}',t')\rangle = \langle \phi(\boldsymbol{x},t)\phi(\boldsymbol{x}',t')\rangle \sim \frac{\kappa^2}{d(d+2)}\exp\big[-(\boldsymbol{x}-\boldsymbol{x}')^2/2\big]\,. \tag{7.2}$$

Hence, $U(\boldsymbol{x},t)$ is essentially constant in time, when time is measured in units of $\tau_{\rm p}$. Since the dynamics is still dissipative, the particles accumulate in the vicinity of the stable minima of the potential $U(\boldsymbol{x},t)$. The extrema of $U(\boldsymbol{x},t)$ are obtained by the condition $\boldsymbol{\nabla}U(\boldsymbol{x}^*,t) = -\boldsymbol{u}(\boldsymbol{x}^*,t) = 0$. Hence, the points $\boldsymbol{x}^*$ are the fixed points of the dynamics (7.1) in configuration space where the fluid-velocity field vanishes. In order for a fixed point $\boldsymbol{x}^*$ to be a minimum of $\boldsymbol{U}(\boldsymbol{x},t)$, all eigenvalues of the Hessian matrix $\partial_i\partial_j U(\boldsymbol{x}^*,t) = -A_{ij}$ must be positive. These two conditions define isolated points $\boldsymbol{x}^*$ in space where particles are trapped.

Traps are created and destroyed at rate $\sim \tau_{\rm c}^{-1}$. A trap is destroyed when, e.g., one of the eigenvalues of the Hessian becomes negative. The particles in the vicinity of a destroyed trap are released and migrate to another trap. The migration time of the particles from one trap to next is given by $\sim \max\{\tau_{\rm p},\tau_{\rm a}\}$, which is much smaller than the typical persistence time of the traps. Hence, when $\tau_{\rm c} \gg \tau_{\rm a},\tau_{\rm p}$, the migration of particles between traps can be neglected. As a consequence, the particles spend the vast majority of the time close to the stable minima of $U(\boldsymbol{x},t)$.

In the strict limit Ku $\to \infty$, St $\to 0$ so that KuSt $\propto \kappa =$ const, we can therefore obtain the dynamics of the particles by considering the tangent flow in the vicinity of the traps

$$\tfrac{\mathrm{d}}{\mathrm{d}t}\boldsymbol{R}_t = \begin{pmatrix} 0_{d\times d} & \mathbb{1}_{d\times d} \\ \mathbb{A}_n & -\mathbb{1}_{d\times d}\end{pmatrix}\boldsymbol{R}_t\,, \tag{7.3}$$

where $\mathbb{A}_n = -\mathrm{Hess}\,U(\boldsymbol{x}_n^*,t)$ is the fluid-velocity gradient matrix at the n-th trap. Because the separation between traps is of the order of $\sim \eta = 1$ the matrices $\mathbb{A}_n$ are approximated by independent, identically distributed random matrices, so that $\langle \mathbb{A}_{n,ij}\mathbb{A}_{n',kl}\rangle \approx \langle \mathbb{A}_{n,ij}\rangle\langle \mathbb{A}_{n',kl}\rangle$ for $n \neq n'$.

7.2 Observables in one spatial dimension

Observables in the persistent limit are computed by the following strategy: At a trap with index n we compute the observables conditional on the realisation of the gradient matrix $\mathbb{A}_n$. The statistics of realisations of $\mathbb{A}_n$ are given by the properties of the random potential $U(\boldsymbol{x},t)=-\phi(\boldsymbol{x},t)$. They can be computed from the so-called 'Kac-Rice formula' [121, 122].

One then removes the conditioning by integrating the conditional observables over the statistics of realisations of $\mathbb{A}_n$. In Paper B we have computed the leading Lyapunov exponent λ_1 and the rate of caustic formation J in the one-dimensional persistent limit. Generalisations to higher dimensions can be done in a similar way, as long as the underlying fluid-velocity field is sufficiently compressible. For a homogeneous, isotropic and incompressible fluid-velocity field $\boldsymbol{u}(\boldsymbol{x},t)$, there are no particle traps of the kind I describe here, because $\mathrm{Tr}\mathbb{A}=0$. Hence, the linearised fluid-velocity field fixed point $\boldsymbol{x}^*$ for which $\boldsymbol{u}(\boldsymbol{x}^*,t)=0$ has at least one unstable direction.

7.2.1 Leading Lyapunov exponent and rate of caustic formation

From now on, I restrict the discussion to the one-dimensional case. In this case, the existence of particle traps is ensured by the compressibility of the one-dimensional fluid-velocity field. We start by considering the dynamics of the particle velocity gradient $Z_t=\tan\alpha_t$. From Eq. (5.4a) we obtain the equation of motion for Z_t, given by

$$\tfrac{\mathrm{d}}{\mathrm{d}t}Z_t=-Z_t-Z_t^2+A_n\,, \tag{7.4}$$

where we have replaced $A_t\to A_n$, so that the particle trajectory is in the vicinity of the n-th trap. The distribution of the gradient A_n at any trap is obtained from the Kac-Rice formula [121, 122]. The latter gives the density

$$P(A_n=a)=\begin{cases}\frac{|a|}{\kappa^2}\exp[-a^2/\kappa^2]\,, & a\le 0\\ 0\,, & a>0\,.\end{cases} \tag{7.5}$$

$P(A_n=a)$ is the probability density of gradients $A(x^*,t)$ conditional on that the fluid-velocity field $u(x^*,t)$ at x^* vanishes and that $A(x^*,t)<0$. Note that this density is very different from Gaussian, although both the one-dimensional fluid-velocity field $u(x,t)$ and its gradient $A(x,t)$ have Gaussian statistics at any position x in space. The reason for this discrepancy is that the density in Eq. (7.5) is evaluated at the particle position x_t, which must lie close to a stable minimum of the potential $U(x,t)=-\phi(x,t)$.

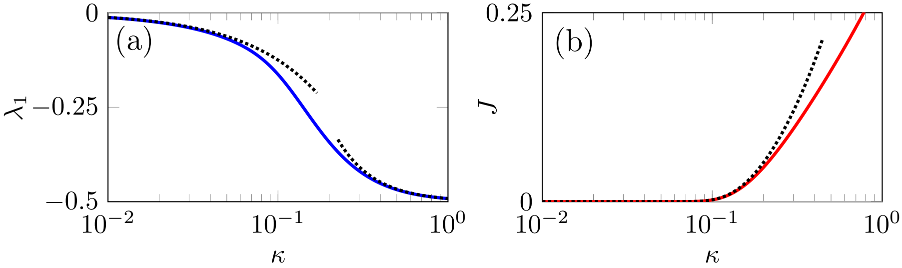

Figure 7.1: Leading Lyapunov exponent λ_1 and rate of caustic formation J in the one-dimensional persistent limit. (a) λ_1 as functions of κ, Eq. (7.6). The dotted lines show the asymptotic behaviour for small and large κ, see main text. (b) J as a function of κ, Eq. (7.7). The dotted line shows the the activated behaviour for small κ, see main text.

In Paper B we apply the conditioning method that I briefly described in the beginning of this section to calculate the leading phase-space Lyapunov exponent λ_1 and the rate of caustic formation J. The results are

$$\lambda_1 = -\frac{1}{2} + \frac{{}_2F_2\big[1,3/2,7/4,9/4;-1/(32\kappa^2)\big]}{120\kappa^2}\,, \tag{7.6}$$

and

$$J = (2^{5/2}\pi)^{-1}\exp\big[-1/(64\kappa^2)\big]\,K_{-1/4}[1/(64\kappa^2)]\,, \tag{7.7}$$

where ${}_2F_2$ and K are the generalised hypergeometric function and the modified Bessel function, respectively [123]. Figure 7.1 shows the expressions (7.6) and (7.7) as functions of κ. The Lyapunov exponent λ_1 in Fig. 7.1(a) is always negative. For small κ, we find $\lambda_1 \sim -\sqrt{\pi/2}\kappa$, which corresponds to result for advected particles, obtained in Ref. [124]. In the large-κ limit, λ_1 asymptotes to $-1/2+1/(120\kappa^2)$. This means that the particle density in phase-space concentrates on point-like sets and does not have the fractal structure that we observed Chapter 3. The rate of caustic formation J shown in Fig. 7.1(b) has an exponential activation for small κ, $J \sim \kappa\exp[-1/(96\kappa^2)]$, similar to that observed in a slightly different context in Ref. [118].

For finite Ku and St, the migration time between the traps is in general not negligible compared to their typical lifetime. During the migration of particles from one trap to another, the particles move through the fluid, sampling different fluid-velocity gradients on their way. In particular, there is a finite probability of sampling positive gradients, as opposed to $P(A_n > 0) = 0$ for the density (7.5). The particles migrate over typical length scales of $\sim \eta = 1$ through the flow. The effect of the migration on the gradient density thus depends on non-local properties of the random potential $U(\boldsymbol{x}, t)$. Therefore, we have no closed-form expression for the probability density $P(A_n = a)$ of fluid-velocity gradients. However, we compute this density numerically in Paper B, see Fig. 4 in that paper.

In the second part of Paper B we show that the numerically computed gradient density allows to approximate λ_1 and J in the vicinity of the persistent limit. This approximation is surprisingly good, as can be observed in Fig. 3 of the paper. This suggests that for large enough Ku and small enough St, the knowledge of the distribution of fluid-velocity gradients essentially determines all observables. Dynamical effects that come from the interplay of the fluid-velocity field with particle dynamics can be neglected. The reason is that the condition $\tau_\mathrm{c} \gg \tau_\mathrm{a}, \tau_\mathrm{p}$ still holds, although not in the strict limit (2.22), so that the particle dynamics takes place on much smaller time scales than τ_c. The main difference to the persistent limit is due to the possibility of sampling positive fluid-velocity gradients for finite Ku and St.

7.3 Implications for simulations and experiments

The results of Paper B apply to a one-dimensional and thus compressible fluid-velocity field. From the discussion in the beginning of this chapter, and in Ref. [124], I expect that similar results can be obtained in sufficiently compressible, higher dimensional flows. The main ingredient of the analysis is the existence of long-lived, localised traps where the particles spend most of their time. In homogeneous, isotropic and incompressible turbulence, there are no such traps for heavy particles. A theory of similar kind may, however, have an application for negatively buoyant particles, that are lighter than the fluid such as, e.g. air bubbles in water. Bubbles may get trapped in the long-lived vortical structures in turbulence, and experience persistent gradients.

An interesting aspect of the persistent limit is that it allows for caustics only at traps at which $A_n < -1/4$. This can easily be seen from Eq. (7.4), which has a stable fixed point for $A > -1/4$, so that the dynamics cannot escape to negative infinity. Preliminary numerical studies of heavy particles in turbulence [125] suggest that a similar correlation between the momentary properties of the fluid-velocity gradient matrix $\mathbb{A}_t$ and the rate of caustic formation J may exist in two- and three-dimensional systems. I discuss these preliminary results in more detail in the outlook in Chapter 10.

8 Suspensions of particles of different sizes

Mono-disperse suspensions of heavy particles in turbulence are an idealisation. In practice, turbulent suspensions contain particles that are not strictly identical, but vary e.g. in their size, shape and mass. This dispersion in the particle properties has a strong impact on the dynamics of particle suspensions. In this chapter, I review the results of Paper A, where we relax the identical-particle idealisation: We consider suspensions of particles of different Stokes numbers, so-called poly-disperse suspensions.

The first step towards understanding the behaviour of poly-disperse suspensions is to consider suspensions of particles of two Stokes numbers, which we call bi-disperse. Similarly to the mono-disperse case, we assume that the particle suspension is dilute and that particles do not collide, so that the individual particles follow the single-particle equations of motion (3.1). With these simplifications, a bi-disperse suspension is essentially a pair of mono-disperse suspensions, driven by identical realisations of the fluid-velocity field $\boldsymbol{u}(\boldsymbol{x},t)$. Each individual suspension behaves as described in Chapter 3. Since, however, both suspensions are immersed in the same underlying random fluid-velocity field, the *relative* dynamics between particles is non-trivial.

8.1 Bi-disperse particle distribution

The Stokes time $\tau_{\rm p} = \gamma^{-1} = 2\rho_{\rm p}a^2/(9\nu\rho_{\rm f})$, is a function of the radius a of the particle. In a bi-disperse suspension we consider two different particle species with radii a and a', and with corresponding Stokes times $\tau_{\rm p}$ and $\tau'_{\rm p}$. I denote by $(\boldsymbol{x}_t,\boldsymbol{v}_t)$ and $(\boldsymbol{x}'_t,\boldsymbol{v}'_t)$ the position and the velocity of a pair of particles with Stokes times $\tau_{\rm p}$ and $\tau'_{\rm p}$. The dimensional equations of motion for $(\boldsymbol{x}_t,\boldsymbol{v}_t)$ and $(\boldsymbol{x}'_t,\boldsymbol{v}'_t)$ then read

$$\tfrac{\rm d}{{\rm d}t}\boldsymbol{x}_t = \boldsymbol{v}_t\,, \qquad \tfrac{\rm d}{{\rm d}t}\boldsymbol{v}_t = \frac{1}{\tau_{\rm p}}[\boldsymbol{u}(\boldsymbol{x}_t,t)-\boldsymbol{v}_t]\,, \tag{8.1a}$$

$$\tfrac{\rm d}{{\rm d}t}\boldsymbol{x}'_t = \boldsymbol{v}'_t\,, \qquad \tfrac{\rm d}{{\rm d}t}\boldsymbol{v}'_t = \frac{1}{\tau'_{\rm p}}[\boldsymbol{u}(\boldsymbol{x}'_t,t)-\boldsymbol{v}'_t]\,. \tag{8.1b}$$

Analogously to the mono-disperse case discussed in Chapter 3, the particle phase-space density of the bi-disperse suspension becomes singular in the

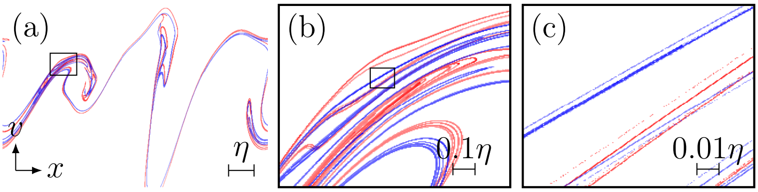

Figure 8.1: Phase-space density of a bi-disperse suspension of particles in the one-dimensional white-noise limit. The phase-space densities of the two different particle species are shown in different colours. Red colour coding corresponds to particles with $\varepsilon = 1.58$, blue colour coding corresponds to particles with $\varepsilon' = 1.43$. The relative parameters (see main text) are given by $\bar{\varepsilon} = 1.5$ and $\theta = 0.1$. The phase-space density has evolved for a long time $\Delta t = t - t_0 = 50$. (a) Phase-space density in a box of size 10η. (b) Magnification by a factor of 10 of the small box in subfigure (a). (c) Magnification by a factor of 10 of the small box in subfigure (b).

long-time limit, and the particles converge to a fractal attractor. Figure 8.1 shows the particle distribution of a bi-disperse particle suspension in the one-dimensional white-noise limit, where the role of $\tau_{\rm p}$ and $\tau'_{\rm p}$ is played by the two different white-noise parameters ε and ε'. In order to see how the different particle species within the suspension behave relative to each other, the phase-space densities ϱ_{t,t_0} and ϱ'_{t,t_0} of particles with ε and ε' are shown in different colours. The red colour coding corresponds to ϱ_{t,t_0} with $\varepsilon = 1.58$, blue colour coding is chosen for the density ϱ'_{t,t_0} with $\varepsilon' = 1.43$. Both densities have evolved for a long time, so that ϱ_{t,t_0} and ϱ'_{t,t_0} are approximations of the infinite-time densities $\bar{\varrho}_t$ and $\bar{\varrho}'_t$, as explained in Chapter 3. In Fig. 8.1(a), we observe that the two particle species cluster on separate attractors $\mathscr{F}_t$ and $\mathscr{F}'_t$ that lie close to each other in phase space. Figures 8.1(b) and (c) show magnifications of the framed boxes in Figs. 8.1(a) and (b), respectively. As we see in these magnifications, the strong correlations between the fractals $\mathscr{F}_t$ and $\mathscr{F}'_t$ that we observe on large scales in Fig. 8.1(a) become less and less pronounced the more we zoom in. In Fig. 8.1(c) the two attractors $\mathscr{F}_t$ and $\mathscr{F}'_t$ appear independent.

This observation was made independently in Refs. [11] and [28], for the distribution of particle separations. The authors in these papers found that the dynamics of particles is spatially uncorrelated at small spatial separations. At larger spatial scales, the particle cluster in a similar way as in the mono-disperse case. These regimes were found to be separated by a scale r_{c}, called the cutoff, or crossover scale [11, 28]. The one-dimensional simulations in Fig. 8.1 show, however, that the behaviour of the fractals at different scales is not restricted to spatial clustering, but holds in phase space. That is, also the velocities of close-by particles are uncorrelated when their relative velocities are small. Yet Fig. 8.1 shows that when the separations and relative velocities are not small, the particles seem to behave similarly to particles of the same size.

8.2 Heuristic description of relative dynamics

Figure 8.1 shows that the particle distribution of a bi-disperse suspension looks, on large scales, like the particle density of a mono-disperse suspension. At small scales, on the other hand, the densities of the individual particle species appear independent. This behaviour can be understood heuristically by considering a pair of particles with different sizes at small separation. I denote the position of the first particle by $\boldsymbol{x}_t$, the position of the second one as $\boldsymbol{x}'_t$. When the separation between the particles is small, $|\boldsymbol{x}_t - \boldsymbol{x}'_t| \ll 1$, we can write $\boldsymbol{u}(\boldsymbol{x}, t)$ at $\boldsymbol{x}'_t$ as the Taylor expansion

$$\boldsymbol{u}(\boldsymbol{x}'_t, t) \sim \boldsymbol{u}(\boldsymbol{x}_t, t) + \mathbb{A}(\boldsymbol{x}_t, t)(\boldsymbol{x}'_t - \boldsymbol{x}_t) . \tag{8.2}$$

The first term in Eq. (8.2) is the fluid-velocity field at the position $\boldsymbol{x}_t$ of the first particle. The second term depends linearly on the particle separation, and on the fluid-velocity gradient. A pair of spatially close-by particles is thus essentially driven by the sum of a constant flow $\boldsymbol{u}(\boldsymbol{x}_t, t)$ and a linear flow $\mathbb{A}(\boldsymbol{x}_t, t)(\boldsymbol{x}'_t - \boldsymbol{x}_t)$.

For a close-by particle pair at $\boldsymbol{x}_t$ and $\boldsymbol{x}'_t$ with identical Stokes times, $\tau_{\mathrm{p}} = \tau'_{\mathrm{p}}$, the term $\boldsymbol{u}(\boldsymbol{x}_t, t)$ accelerates both particles identically. Therefore the relative dynamics of a pair of identical particles is not affected by $\boldsymbol{u}(\boldsymbol{x}_t, t)$, but driven only by the linear flow $\mathbb{A}(\boldsymbol{x}_t, t)(\boldsymbol{x}'_t - \boldsymbol{x}_t)$ [the second term on the right-hand side of Eq. (8.2)].

In a pair of non-identical particles, on the other hand, each particle reacts differently to $\boldsymbol{u}(\boldsymbol{x}_t, t)$, since the Stokes times of the particles differ. Hence, both terms on the right-hand side of Eq. (8.2) contribute to the relative particle dynamics. When the spatial separation between the particles is small enough, the contribution from $\boldsymbol{u}(\boldsymbol{x}_t, t)$ must dominate. But the contribution from $\mathbb{A}(\boldsymbol{x}_t,t)(\boldsymbol{x}'_t-\boldsymbol{x}_t)$ in Eq. (8.2) grows linearly with the particle separation. When the difference between the Stokes times is not too large, we may therefore expect that at larger separations, $\mathbb{A}(\boldsymbol{x}_t,t)(\boldsymbol{x}'_t-\boldsymbol{x}_t)$ dominates over $\boldsymbol{u}(\boldsymbol{x}_t,t)$. These considerations intuitively explain the different behaviours at small and larger particle separations. Note that I have implicitly assumed here that the relative velocities between the particles are small enough so that the particle viscous damping is negligible against the acceleration from the flow field $\boldsymbol{u}(\boldsymbol{x},t)$.

In Paper A we develop a simple, one-dimensional phase-space model for the phase-space separations between the particle species. The model describes the parameter dependence of *two* cutoff scales, r_c and v_c, for the onset of uncorrelated relative motion. I review the construction of this model in the next section.

8.3 Model for relative dynamics

We start out by deriving the equations of motion for particle pairs of two different Stokes times $\tau_{\rm p}$ and $\tau'_{\rm p}$. Each particle in the pair follows its own dynamics determined by its respective equations of motion (8.1). In order to study the *relative* dynamics of the particle pair, we consider the quantities

$$(\Delta\boldsymbol{x}_t,\Delta\boldsymbol{v}_t)=\big(\boldsymbol{x}_t-\boldsymbol{x}'_t,\boldsymbol{v}_t-\boldsymbol{v}'_t\big)\,, \tag{8.3a}$$

$$(\bar{\boldsymbol{x}}_t,\bar{\boldsymbol{v}}_t)=\big(\boldsymbol{x}_t+\boldsymbol{x}'_t,\boldsymbol{v}_t+\boldsymbol{v}'_t\big)\,. \tag{8.3b}$$

Using the single-particle equations of motion (8.1), we can write the dynamics of the quantities in Eq. (8.3) as

$$\tfrac{\rm d}{{\rm d}t}\bar{\boldsymbol{x}}_t=\bar{\boldsymbol{v}}_t\,,\qquad \tfrac{\rm d}{{\rm d}t}\bar{\boldsymbol{v}}_t=\frac{1}{\bar{\tau}_{\rm p}}[\bar{\boldsymbol{u}}-\bar{\boldsymbol{v}}_t+\theta(\Delta\boldsymbol{u}-\Delta\boldsymbol{v}_t)]\,, \tag{8.4a}$$

$$\tfrac{\rm d}{{\rm d}t}\Delta\boldsymbol{x}_t=\Delta\boldsymbol{v}_t\,,\qquad \tfrac{\rm d}{{\rm d}t}\Delta\boldsymbol{v}_t=\frac{1}{\bar{\tau}_{\rm p}}[\Delta\boldsymbol{u}-\Delta\boldsymbol{v}_t+\theta(\bar{\boldsymbol{u}}-\bar{\boldsymbol{v}}_t)]\,. \tag{8.4b}$$

The two parameters $\bar{\tau}_{\rm p}$ and θ in Eq. (8.4) are given by

$$\frac{1}{\bar{\tau}_{\rm p}}=\frac{1}{2}\left(\frac{1}{\tau_{\rm p}}+\frac{1}{\tau'_{\rm p}}\right),\quad \text{and}\quad \theta=\frac{|\tau_{\rm p}-\tau'_{\rm p}|}{\tau_{\rm p}+\tau'_{\rm p}}\,. \tag{8.5}$$

The time scale $\bar{\tau}_{\rm p}$ is the harmonic mean of the two individual Stokes times of the particle pair. The dimensionless parameter θ is a measure for the difference between the two Stokes times. In terms of $\bar{\tau}_{\rm p}$ and θ the equations of motion Eqs. (8.4) are similar to the equations for a reference trajectory and the tangent flow of identical particles in Chapter 3. However, the Stokes time $\tau_{\rm p}$ for identical particles is replaced by the mean Stokes time $\bar{\tau}_{\rm p}$. Furthermore, the dimensionless parameter θ multiplies additional contributions $\bar{\boldsymbol{u}}$ and $\Delta\boldsymbol{u}$ from the fluid-velocity field $\boldsymbol{u}(\boldsymbol{x},t)$. These contributions are expressed in terms of $\boldsymbol{u}(\boldsymbol{x},t)$ as

$$\bar{\boldsymbol{u}} = \boldsymbol{u}(\boldsymbol{x}_t,t)+\boldsymbol{u}\big(\boldsymbol{x}'_t,t\big)\,, \quad \text{and} \quad \Delta\boldsymbol{u} = \boldsymbol{u}(\boldsymbol{x}_t,t)-\boldsymbol{u}\big(\boldsymbol{x}'_t,t\big)\,. \tag{8.6}$$

The contributions of $\bar{\boldsymbol{u}}$ and $\Delta\boldsymbol{u}$ correspond to the constant flow and the linear flow, respectively, in Eq. (8.2). Equation (8.6) shows that $\bar{\boldsymbol{u}}$ and $\Delta\boldsymbol{u}$ are sums of Gaussian random functions evaluated at the positions $\boldsymbol{x}_t$ and $\boldsymbol{x}'_t$. In general, we do not know the statistics of these random terms, because $\boldsymbol{u}(\boldsymbol{x},t)$ is evaluated at the particle positions $\boldsymbol{x}_t$ and $\boldsymbol{x}'_t$, which themselves move through the flow. In the white-noise limit, however, the dynamics of $\boldsymbol{u}(\boldsymbol{x},t)$ becomes independent of the particle position.

8.3.1 White-noise limit

In this section, I show how to take the white-noise limit of Eq. (8.4) to obtain insights into the relative dynamics of a particle pair. Similarly to the white-noise limit in the mono-disperse system discussed in Section 2.5.2, this is done by a suitable reparameterisation of the equations of motion (8.4), followed by a limit in terms of dimensionless parameters. In their current form, Eqs. (8.4) depend only on one time scale, $\bar{\tau}_{\rm p}$, analoguos to $\tau_{\rm p}$ in the mono-disperse case. The parameter θ is dimensionless. Together with the fluid time scales $\tau_{\rm c}$ and $\tau_{\rm a}$ we find that the bi-disperse model can be written in terms of θ and two out of the three dimensionless parameters

$$\bar{\rm St} = \frac{\bar{\tau}_{\rm p}}{\tau_{\rm c}}\,, \qquad {\rm Ku} = \frac{\tau_{\rm c}}{\tau_{\rm a}}\,, \qquad \bar{K} = \frac{\bar{\tau}_{\rm p}}{\tau_{\rm a}}\,. \tag{8.7}$$

In order to take the white-noise limit, we transform the coordinates in Eqs. (8.4) according to $t \to t\bar{\tau}_{\rm p}$, $\boldsymbol{x} \to \eta\boldsymbol{x}$, $\boldsymbol{v} \to \eta\boldsymbol{v}/\bar{\tau}_{\rm p}$ and $\boldsymbol{u} \to \eta\boldsymbol{u}/\bar{\tau}_{\rm p}$. This way, the equations of motion (8.4) loose their explicit dependence on $\bar{\tau}_{\rm p}$. The dependence on $\bar{\rm St}$ and Ku is entirely contained in the correlations of the terms $\bar{\boldsymbol{u}}$

and $\Delta\boldsymbol{u}$. Taking the limit $\bar{\mathrm{St}} \to \infty$ and $\mathrm{Ku} \to 0$ such that $\mathrm{Ku}^2\bar{\mathrm{St}}$ stays finite, the terms $\bar{\boldsymbol{u}}$ and $\Delta\boldsymbol{u}$ become white-noise signals. Furthermore, the statistics of $\bar{\boldsymbol{u}}$ and $\Delta\boldsymbol{u}$ depend only on the spatial separation $\Delta\boldsymbol{x}_t$, and not on $\bar{\boldsymbol{x}}_t$. This means that the equation of motion for $\bar{\boldsymbol{x}}_t$ decouples from the rest of the equations. The term $\Delta\boldsymbol{u}_t$, for instance, has zero mean and correlation function

$$\begin{aligned}\langle \Delta u_i(t)\Delta u_j(t')\rangle &\sim \big\langle \big[u_i(\boldsymbol{x}_t,t)-u_i(\boldsymbol{x}'_t,t)\big]\big[u_j(\boldsymbol{x}_{t'},t')-u_j(\boldsymbol{x}'_{t'},t')\big]\big\rangle\,,\\ &= \frac{4\bar{\varepsilon}^2}{1+2\wp}K_{ij}(\Delta\boldsymbol{x})\delta(t-t'),\end{aligned} \tag{8.8}$$

for $|\Delta\boldsymbol{x}| \ll 1$, with the tensor K_{ij} defined in Eq. (2.11). The diffusion constant $\bar{\varepsilon}^2 = \mathrm{Ku}^2\bar{\mathrm{St}}(1+2\wp)/d$ is the analogue of ε^2 in the mono-disperse case, see Eq. (2.21). The other correlation functions of $\bar{\boldsymbol{u}}$ and $\Delta\boldsymbol{u}$ read

$$\begin{aligned}\langle \bar{u}_i(t)\bar{u}_j(t')\rangle &\sim \frac{4\bar{\varepsilon}^2}{1+2\wp}\big[2\delta_{ij}-K_{ij}(\Delta\boldsymbol{x})\big]\delta(t-t'),\\ \langle \Delta u_i(t)\bar{u}_j(t')\rangle &= 0\,.\end{aligned} \tag{8.9}$$

In Paper A we analyse the one-dimensional white-noise limit of the equations of motion Eq. (8.4) to describe numerical simulations of the model in higher dimensions. The description of the model in Paper A is rather brief. I therefore discuss the one-dimensional model in more detail in the following.

8.3.2 Bi-disperse white-noise model in one spatial dimension

The one-dimensional version of the white-noise model of the bi-disperse model allows important insights into the behaviour in higher dimensions. In particular, the main property of the bi-disperse dynamics is that there are two distinct regimes of diffusion: One of them is a regular, additive diffusion which dominates at small separations and small relative velocities. In the second regime, the contributions from the fluid-velocity field that drive Eq. (8.4) are multiplicative in Δx_t. This leads to essentially mono-disperse dynamics at larger separations and larger relative velocities, in keeping with the intuitive conclusions drawn in Section 8.2. The simplest way to describe these regimes is provided by the one-dimensional white-noise limit.

In one spatial dimension, the fluid-velocity field is fully compressible, $\wp = 1$, and all quantities are scalars. We merge the noise terms in Eqs. (8.4) by writing them as the vector $\boldsymbol{\xi}_t$ with components $\xi_t^{(1)} = \Delta u + \theta\,\bar{u}$, $\xi_t^{(2)} = \bar{u} + \theta\Delta u$. This way, we obtain from Eqs. (8.4) the simplified dynamics

$$\frac{\mathrm{d}}{\mathrm{d}t}\Delta x_t = \Delta v_t\,, \tag{8.10a}$$

$$\frac{\mathrm{d}}{\mathrm{d}t}\begin{pmatrix}\Delta v_t\\ \bar{v}_t\end{pmatrix} = -\begin{pmatrix}1 & \theta\\ \theta & 1\end{pmatrix}\begin{pmatrix}\Delta v_t\\ \bar{v}_t\end{pmatrix} + \boldsymbol{\xi}_t\,. \tag{8.10b}$$

As discussed earlier in this chapter, the equation for $\bar{x}_t$ decouples from the rest of the equations in the white-noise limit, so that it does not appear in Eqs. (8.10). Recall that $(\bar{x}_t, \bar{v}_t)$ in the bi-disperse dynamics corresponds to (x_t, v_t) (the reference trajectory) in the mono-disperse case. In the mono-disperse dynamics, however, both x_t and v_t decouple from the dynamics of the tangent flow $\boldsymbol{R}_t = (\delta x_t, \delta v_t)^{\mathsf{T}}$ in the white-noise limit. In Eq. (8.10), on the other hand, $\bar{v}_t$ does not decouple. The vector-valued noise term $\boldsymbol{\xi}_t$ is white in time, but its correlation functions depend on the separations. The diffusion matrix $\mathscr{D}_{ij} = \int_0^\infty \mathrm{d}t\,\langle \xi_t^{(i)}\xi_0^{(j)}\rangle$ reads

$$\mathscr{D} \sim \frac{4}{3}\bar{\varepsilon}^2\begin{pmatrix}\theta^2 + 3/4(1-\theta^2)\Delta x_t^2 & \theta\\ \theta & 1\end{pmatrix}. \tag{8.11}$$

For $\theta = 0$ the equations for Δv_t and $\bar{v}_t$ in Eq. (8.10) decouple and $(\Delta x_t, \Delta v_t) \to (\delta x_t, \delta v_t)$ becomes the one-dimensional tangent flow. In this case, the relative motion of the particles is driven only by the fluid-velocity gradients. The equations for the mean motion $(\bar{x}_t, \bar{v}_t)$ are then equivalent to the twice single-particles dynamics since $(\bar{x}_t, \bar{v}_t) \to 2(x_t, v_t)$ for $\theta \to 0$.

For $\theta = 1$, on the other hand, Eq. (8.10) describes relative dynamics of a particle pair the limit of one particle being much smaller than the other one. In this case, the diffusion matrix $\mathscr{D}$ in Eq. (8.11) is independent of Δx_t, so that Eq. (8.10) becomes a Gaussian process.

For $0 < \theta < 1$ the nature of the particle motion depends on the magnitudes of the particle separation Δx_t, and of the relative velocity Δv_t. As we argue in Paper A, the dynamics continuously alternates between being purely diffusive for $\Delta x_t^2 \ll \theta^2/(1-\theta^2)$ and $\Delta v_t^2 \ll \bar{\varepsilon}^2\theta^2$, and being effectively mono-disperse for $\Delta x_t^2 \gg \theta^2/(1-\theta^2)$ and $\Delta v_t^2 \gg \bar{\varepsilon}^2\theta^2$. This leads to the definition of the cutoff scales r_c and v_c:

$$r_{\mathrm{c}} \sim \frac{\theta}{\sqrt{1-\theta^2}}\,, \qquad \text{and} \qquad v_{\mathrm{c}} \sim \bar{\varepsilon}\theta\,. \tag{8.12}$$

For small enough θ both cutoff scales depend linearly on θ. For separations and relative velocities smaller than the cutoff scales (8.12), the diffusion constant $\mathscr{D}$ is independent of Δx_t:

$$\mathscr{D} \sim \frac{4}{3}\bar{\varepsilon}^2 \begin{pmatrix} \theta^2 & \theta \\ \theta & 1 \end{pmatrix} . \tag{8.13}$$

In this case, the process (8.10) is Gaussian. The Gaussian dynamics at small phase-space separations leads to a steady-state distribution that is Gaussian at small Δx_t and Δv_t. In the opposite case, on the other hand, the equations of motion for Δv_t and $\bar{v}_t$ decouple, so that $(\Delta x_t, \Delta v_t)$ becomes independent of $\bar{v}_t$. In this limit, we obtain the effective equations of motion

$$\tfrac{\mathrm{d}}{\mathrm{d}t}\Delta x_t = \Delta v_t \, , \tag{8.14a}$$

$$\tfrac{\mathrm{d}}{\mathrm{d}t}\Delta v_t \sim -\Delta v_t + \Delta x_t \eta_t \, . \tag{8.14b}$$

The white-noise η_t has the correlation $\langle \eta_t \eta_{t'} \rangle = 2\bar{\varepsilon}^2(1-\theta^2)\delta(t-t')$, so that Eqs. (8.14) are identical to the equations of motion of a mono-disperse particle pair in the one-dimensional white-noise limit, but with an adjusted (effective) white-noise parameter, $\varepsilon^2 \to \bar{\varepsilon}^2(1-\theta^2)$. For small θ, this substitution reads $\varepsilon^2 \to \bar{\varepsilon}^2$, as discussed in Paper A. Hence, for phase-space separations $\mathscr{R}_t$ much larger than the phase-space cutoff $R_c = \sqrt{r_c^2 + v_c^2}$, the distribution of phase-space separations $P(\mathscr{R}_t \le \delta)$ has a power-law scaling, Eq. (4.1), with exponent D_2, as explained in Secs. 4.1 and 5.2.1.

In terms of the steady-state probability density $P_s(\Delta x, \Delta v)$, the two different regimes lead to a Gaussian plateau for phase-space separations smaller than the cutoff scales (8.12), and to power-law tails at large phase-space separations. Fig. 8.2(a) shows a schematic contour plot of the logarithm of $P_s(\Delta x, \Delta v)$. The yellow region shows that the plateau which is bounded by the two cutoff scales r_c and v_c. The blue region with equidistant level lines (dotted lines) shows the mono-disperse regime, where the distribution scales as a power law.

Although our derivation of the cutoff-scales as presented here is strictly valid only for the one-dimensional white-noise limit of the relative dynamics (8.4), the conclusions apply qualitatively also in higher dimensions, because the random fluid-velocity field $\boldsymbol{u}(\boldsymbol{x}_t, t)$ is spatially isotropic. For $d > 1$ the radial separation $r = |\Delta \boldsymbol{x}_t|$ takes the role of Δx_t, and the radial velocity $v_r = \Delta v_t \cdot \Delta x_t / r$ corresponds to Δv_t.

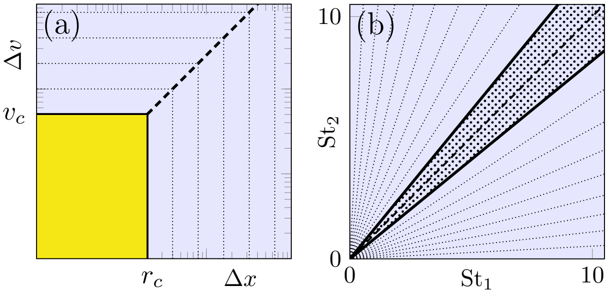

Figure 8.2: Schematic contour plots of the joint distribution $P_s(\Delta x, \Delta v)$, and of $\theta(\mathrm{St}_1, \mathrm{St}_2)$. (a) Contour of the logarithm of the joint distribution, $\log P_s(\Delta x, \Delta v)$ plotted schematically against Δx and Δv, both plotted on a logarithmic scale. The yellow region marks the plateau. The blue region with the dotted lines corresponds to the power-law regime (see main text). (b) Contour plot of θ in the St_1-St_2 parameter plane. The dashed line shows $\mathrm{St}_1 = \mathrm{St}_2$, the dotted region corresponds to $\theta < 0.1$. The thick, solid lines show to the level lines $\theta = 0.1$. The dotted lines show the levels $\theta = 0.2, 0.3, \ldots, 0.9$.

We confirm the qualitative agreement of the one-dimensional model with the higher-dimensional case in Paper A. In Fig. 1(a) in Paper A we show numerical simulations of the two-dimensional statistical model. For $r \gg r_\mathrm{c}$ and $v_r \gg v_\mathrm{c}$, the distribution shows a power-law behaviour, just as in the mono-disperse case [23]. The exponent of the power-law is identical to that of the mono-disperse case, but with adjusted Stokes number $\mathrm{St} \to \bar{\mathrm{St}}$, see Fig 1(d) in Paper A. Note again that the Stokes number St and the mean Stokes number $\bar{\mathrm{St}}$ correspond to ε and $\bar{\varepsilon}$, respectively in the white-noise limit. Hence, the $\bar{\mathrm{St}}$ dependence of the exponent is explained by the effectively mono-disperse dynamics (8.14) in the tails, where $\varepsilon \to \bar{\varepsilon}$ for small θ. Similarly, the approximately linear dependence of the cutoff scales r_c and v_c on the parameter θ, Eq. (8.12), is confirmed for the two-dimensional statistical model in Fig. 1(c) in Paper A.

To conclude, there are two different regimes in the dynamics of bi-disperse suspensions that depend on the two parameters θ and $\bar{\mathrm{St}}$ ($\bar{\varepsilon}$ in the white-noise limit). The magnitude of the parameter θ determines the size of the plateau in the joint distribution of Δv_t and Δx_t. When θ is small enough, one can observe a clear separation between the diffusive and the mono-disperse behaviour. For θ of the order of $\theta \approx 0.1$, however, the cutoff scales r_c and v_c are of the order or the regime of validity of the smooth approximation that defines the Batchelor regime. This means that the onset of the power-laws may not be observed when θ is too large. This can be seen in Fig 1(c) in Paper A: For $\theta = 0.1$, the power-law tails in the distribution of the radial velocity v_r at small radial separations is completely covered by the extensive plateau in the distribution. In the $\mathrm{St}_1 - \mathrm{St}_2$ parameter plane, the region $\theta \le 0.1$ is quite small. In other words, if we pick two values for St_1 and St_2 at random, the probability of having $\theta \le 0.1$ is relatively small. Figure Fig. 8.2(b) shows a contour plot of θ as a function of St_1 and St_2. The wedge-shaped dotted region corresponds to $\theta \le 0.1$. That the case $\theta \le 0.1$ occupies only a small area in the $\mathrm{St}_1 - \mathrm{St}_2$ parameter plane has important implications for numerical simulation and experiments. Here the parameter θ is often so large that the diffusive dynamics extends into the inertial range of turbulence, where smooth approximations of the kind (2.10) break down.

8.4 Implications for simulations and experiments

In my opinion, the most relevant result of our investigation of bi-disperse particle suspensions is the parameter dependence of the cutoff scales r_c and v_c in Eq. (8.12). In the numerical simulations carried out recently in Refs. [33, 35] the authors consider the root-mean square radial velocity $w = \sqrt{\langle v_r^2 \rangle}$ of particle pairs in bi-disperse suspensions in turbulence. As the authors of Refs. [33, 35] vary the individual (turbulent) Stokes numbers, St_1 and St_2, of the particle pair, they observe that w is smallest for $\mathrm{St}_1 = \mathrm{St}_2$, where $\theta = 0$. This is explained by the results of our model, because finite θ cuts off the distribution of relative velocities at small $|\Delta v_t|$, giving more weight to large relative velocities, and resulting in a minimum of w at $\theta = 0$. In Ref. [34] the authors considered the steady-state distribution $P_s(v_r, r)$, evaluated at finite $r \approx 1$, see Figs. 2 and 4 in that paper. Here r is measured in units of the Kolmogorov scale η_{K}. The authors observe that the distribution is essentially Gaussian with increasing variance as the difference in the Stokes numbers increases. This finding is explained in terms of our model by looking at their θ values, which range between $\theta \approx 0.33$ and ≈ 0.94, so that the joint distribution $P_s(v_r, r)$ is dominated by the plateau. Because the chosen values of θ in Ref. [34] are quite large, the plateau extends approximately to the Kolmogorov scale and there are no power-law tails at small scales.

Both the power-law tails and the plateau in $P(v_r, r)$ are observed in Ref. [37]

where validity of our bi-disperse model is studied by numerical simulations of particles in turbulence. They authors of Ref. [37] confirm the linear dependence of both cutoff scales r_c and v_c on the parameter θ, for small θ. This shows that θ is the characteristic parameter that determines the size of the plateau in the distribution $P(v_r, r)$, as predicted by our one-dimensional model.

In experiments [41, 43, 44, 45] particle suspensions are always poly-disperse. This means that θ itself becomes a random variable that differs from particle pair to particle pair. It is challenging to generate a narrow range of Stokes numbers in experiments because the Stokes number in turbulence $\mathrm{St} = \tau_\mathrm{p}/\tau_\mathrm{K}$ is calculated by dividing the Stokes time τ_p by the Kolmogorov time scale τ_K, both of which are subject to uncertainties. The main uncertainty in the Stokes time is the particle radius a which has a relative error of between 1/6 and 1/3 in Refs. [41, 43, 45] and approximately 1/20 in Ref. [44] . The main uncertainty in the estimation of τ_K is the energy dissipation rate ϵ which was reported to have a relative error of about 1/10 in Refs. [41, 43]. From the error estimates of the particle radii a and of the turbulent energy dissipation rate ϵ in the experimental papers, one can estimate the fluctuations in the parameter θ. Given the error estimates reported in Refs. [41, 43], for instance, we can roughly estimate the standard deviation of θ to be ≈ 0.3. According to our model this corresponds to substantial fluctuations of the size of the plateau, of the order of the Kolmogorov scale η_K. This means that it is challenging to actually measure the predictions of the bi-disperse model, let alone the mono-disperse model, in state-of-the-art experiments, because the plateau in the distribution $P_s(v_r, r)$ is likely to be of the order of η_K. In order to explain experimentally obtained particle distributions at sub-Kolmogorov scales, one must therefore model the effect of a random θ that varies among particle pairs. I discuss my ideas for such a model in the outlook in Chapter 10.

PART IV

CONCLUSIONS AND OUTLOOK

In my opinion, the most fascinating aspect of research is that it never ends. It starts with a question, an idea or simply a plan of how to calculate or measure something. Sometimes, if we are lucky, our questions have definite answers, and we eventually reach a conclusion. If not, we are led to ask new, and possibly more precise questions, formulate new ideas, and make new plans.

In my time as a doctoral student I was given the opportunity to ask questions, and was lucky to find answers to some of them.

9 Conclusions

For me, the most intriguing result of my work is the linear part in the rate function of the spatial FTLE $\hat{\sigma}_t$, presented in Chapter 6 and Paper C. One reason could be that it is my latest work. For some reason I am most enthusiastic about the questions that I am thinking about at the moment. But I believe it is more than just that. My feeling is that this result combines several aspects that make a good story. First, it starts out with an interesting question: how do caustic folds affect spatial clustering? Second, posing the question in a way so that it could be answered, required me to learn about large-deviation theory, a mathematical subject that was entirely new to me. Third, the analysis of the question with these tools leads to a surprisingly simple answer, that has far-reaching consequences which go beyond the initial scope of this work. Finally, and perhaps most importantly, the result leads to many new and refined questions, which I could not formulate in the beginning. This feeling of only having scratched the surface is, to me, exciting and frightening at the same time.

The possibly most important result, albeit being only partly new, is the explanation of the cutoff-scales r_c and v_c of the relative phase-space dynamics of bi-disperse particles, presented in Chapter 8 and Paper A. This result shows that different particle sizes have a significant effect on the relative distribution at small phase-space separations. Even in state-of-the-art laboratory experiments, it is very challenging to generate a droplet-size distribution that is narrow enough to justify the mono-disperse approximation for the suspension. Therefore, the parameter θ that controls the magnitude of the cutoff-scales is most probably too large to measure a power-law scaling in the distribution of phase-space separations at scales of the order of the Kolmogorov length scale. The next question must therefore be how we can explain the phase-space distribution of poly-disperse particle suspensions at these scales

I started working on the persistent limit (presented in Chapter 7 and Paper B) as a simple toy example for a particle model with a fluid-velocity field of non-zero (but infinite!) correlation time τ_c. Soon I realised that it is analytically solvable, although perhaps, I thought, unphysical. In my opinion, the model offers quite a unique and simple way of understanding the particle dynamics when the fluid changes only slowly. As it seems to turn out now [125] the methods that I used to solve the persistent limit, albeit in a different form, may be useful to explain some aspects of the particle dynamics in turbulence. The persistent limit seems to explain the necessary local conditions under which caustics form along trajectories. I come back to this point in the outlook.

10 Outlook

Finally, I describe some of the new questions that emerged from previous ones. As initial ideas do, these research questions vary substantially in their concreteness and precision. In this last chapter of the thesis, I formulate these questions as precisely as I can, while trying to be vague enough to account for all uncertainties.

Poly-disperse suspensions of particles

A poly-disperse suspension at scales below the correlation length η of the fluid-velocity field can be interpreted as an ensemble of many mono-disperse suspensions, each of which clusters on its own fractal attractor $\mathscr{F}_t$ in phase-space. The relative dynamics between the particles in the suspension is characterised by the parameters θ and $\bar{\mathrm{St}}$, that I introduced in Chapter 8. If we take a particle pair from the suspension at random, the parameters θ and $\bar{\mathrm{St}}$ are random variables.

In nature and experiments the distributions of θ and $\bar{\mathrm{St}}$ depend on what the particles are made of, and how they are created. In turbulent clouds, for instance, the size distribution of water droplets depends on the history of particle collisions [2]. In experiments, on the other hand, the particles may be liquid or solid, and they can be created in different ways, affecting their size distributions. In the experiments reported in Refs. [41, 43, 44] the particles are made of a liquid that is brought onto a spinning disc. The spinning disc spills out the liquid as small droplets with a narrow size distribution. In Ref. [45] small solid particles ('glass bubbles') are used whose size distribution is controlled by sieving.

For a given distribution of Stokes numbers, it is a simple task to compute the joint distribution of $\theta = |\mathrm{St}_1 - \mathrm{St}_2|/(\mathrm{St}_1 + \mathrm{St}_2)$ and $\bar{\mathrm{St}} = 2/(\mathrm{St}_1^{-1} + \mathrm{St}_2^{-1})$, assuming that for a randomly chosen pair of particles the Stokes numbers St_1 and St_2 are independent and identically distributed. A short calculation shows that for a simple homogeneous particle-size distribution in a range between $a_{\rm max}$ and $a_{\rm min}$, one obtains a joint distribution $P(\theta, \bar{\mathrm{St}})$ of θ, $\bar{\mathrm{St}}$ that is peaked at $\theta = 0$ and that vanishes at a maximum value $\theta_{\rm max} = |a_{\rm max}^2 - a_{\rm min}^2|/(a_{\rm max}^2 + a_{\rm min}^2)$.

In Chapter 8, I modelled the relative dynamics of a particle pair of different but fixed Stokes numbers, and thus for fixed θ and $\bar{\mathrm{St}}$. One can formulate a simple model for the relative dynamics of a poly-disperse suspension by interpreting the results from Chapter 8 as conditioned on the values θ and $\bar{\mathrm{St}}$, $P(v_r, r|\theta, \bar{\mathrm{St}})$. The joint distribution of relative velocities v_r and separations r in the poly-disperse suspension is then given by lifting the conditioning:

$$P(v_r, r) = \int \mathrm{d}\theta \int \mathrm{d}\bar{\mathrm{St}}, P(v_r, r|\theta, \bar{\mathrm{St}}) P(\theta, \bar{\mathrm{St}}) . \tag{10.1}$$

From this simple model we may get a qualitative estimate of the shape of the joint distribution of separations and relative velocities $P(v_r, r)$. My future plan is compare this distribution to the results of numerical simulations and experiments.

Persistent limit in higher dimensions

A question for heavy particles in incompressible turbulence is: Are there characteristic local configurations of the turbulent fluid-velocity field $\boldsymbol{u}(\boldsymbol{x},t)$, and its gradient $\mathbb{A}(\boldsymbol{x},t)$, that cause nearby particles to form a caustic? This question is of general importance because it could improve our understanding of how caustics form in the particle dynamics.

In numerical simulations of heavy particles in incompressible turbulence indications were found [125] that such characteristic configurations indeed exist. These preliminary studies show that the momentary properties of the fluid-velocity gradient matrix $\mathbb{A}(\boldsymbol{x}_t,t)$ are strongly correlated with the occurrence of caustics. In two-dimensional turbulence, for instance, it appears that caustics occur along trajectories when $\mathrm{Tr}\mathbb{A}(\boldsymbol{x}_t,t)^2>0$, but never in the opposite case [125].

This finding can be explained with the methods developed for the one-dimensional persistent limit in Chapter 7. Although the persistent limit $\tau_{\rm c}\gg\tau_{\rm a},\tau_{\rm p}$ is not strictly justified in turbulent flows, numerical results [126] suggest that $\tau_{\rm c}$ is typically between 3 and 8 times larger than $\tau_{\rm a}$. For small enough $\tau_{\rm p}$, we may therefore, in a reasonable approximation, treat the fluid-velocity gradient matrix as constant in time, $\mathbb{A}(\boldsymbol{x}_t,t)=\mathbb{A}(\boldsymbol{x}_t)$. Note however, that there are no particle traps in incompressible turbulence, so that the statistics of $\mathbb{A}_t$ is unknown and needs to be measured by following particles through the flow. Preliminary results on the analysis of the two-dimensional persistent limit confirm that caustics form only when $\mathrm{Tr}\mathbb{A}(\boldsymbol{x}_t,t)^2>0$, in agreement with the numerical results for heavy particles in turbulence [125]. The three-dimensional case seems to be more complicated. My plan is to generalise these preliminary results to $d=3$. Using the persistent limit, I want to predict a 'phase diagram' of the rate of caustic formation as a function of the invariants of the fluid-velocity gradient matrix $\mathbb{A}(\boldsymbol{x}_t,t)$.

Spatial projection of the phase-space density

So far, the analysis of the projection to of the phase-space distribution $\bar{\varrho}_{t,t_0}$ to configuration space applies to the long-time statistics of local phase-space neighbourhoods in one spatial dimension. For these neighbourhoods, I derived in Chapter 6 and in Paper C the large-deviation form of the rate function of the spatial finite-time Lyapunov exponent (FTLE) $\hat{\sigma}_t$. We conjectured that the rate function of the sum of spatial FTLEs $\hat{S}_t$ may have the same form.

Clearly, it would be satisfying to prove this conjecture for the higher-dimensional case. Apart from that, I explained in Chapter 6, and in Paper C, that the projection formula for the spatial correlation dimension $\hat{D}_2$ follows from the linear part in the spatial rate function. For $q > 2$, it was shown in Refs. [117, 127] that a generic fold of a constant probability measure distributed homogeneously over a d-dimensional subspace leads to $\hat{D}_q < d$. This indicates that the effect of caustic folds on the spatial Renyi dimension $\hat{D}_q$ may, for $q > 2$, be more drastic than the simple saturation obtained from the projection formula (6.17). In short, the folds may decrease $\hat{D}_q$ below d. My plan is to analyse $\hat{D}_q$ for $q > 2$ using a combination of the so-called multifractal formalism [68, 71, 128], a large-deviation formalism for fractals, and the 'contraction principle' [85, 129] for rate functions. This principle allows one to compute rate functions of lower dimensional systems from the rate functions defined on higher-dimensional spaces.

Finally, I plan to investigate further the connection between the phase-space folds of the phase-space density $\bar{\varrho}_t$ and catastrophe theory. In optics, Berry [120] showed that catastrophes of different co-dimension determine how the statistical moments of the light intensity diverge as the wavelength tends to zero. These divergences are analogous to the divergence of the spatial scaled cumulant-generating function $\hat{\Lambda}(k)$ discussed in Chapter 6. In optics the wavelength provides a natural cutoff, so that intensity moments diverge only when the cutoff is removed. My plan is to study $\hat{\Lambda}(k)$ for $k \leq -1$ in the presence of such a cutoff, which could be given by, for instance, a finite number of particles. This analysis could give further insights into the effect of the spatial projection upon the spatial distribution of particles.

On a different yet related note, I plan to study the effect of measurement noise on the spatial rate function $\hat{I}(s)$. This analysis may, together with the assumption of a finite number of particles, allow to predict the shape of the spatial rate function under conditions that are closer to those in laboratory experiments.

ACKNOWLEDGEMENTS

This thesis, although written by my hand, was conceived with the help of others, to whom I would like to express my gratitude. First, I thank my supervisor Bernhard Mehlig for his enthusiasm, and for his motivating words. His criticism, and his ability to transform my vague ideas into precise questions, were a crucial guidance. I thank my co-supervisor Kristian Gustavsson for his help with technical and numerical questions, which he seems to have mastered decades ago.

I am grateful to our collaborators Jeremie Bec, Fabien Candelier, Fredrik Lundell, Lorenzo Pistone and Tomas Rosén for their effort to make our projects reality.

I thank my office mates Johan and Anshuman who are always open for a discussion, and who proof-read initial versions of the thesis. All mistakes and typos left in this text are mine alone.

Finally, I thank Sophia for her love, and for her continuous support. Soon we will show the world that one plus one sometimes equals three.

Bibliography

[1] MEIBOHM, J 2018 Clustering and caustics in one-dimensional models of turbulent aerosols. Licentiate thesis, Göteborgs universitet.

[2] SHAW, R. A 2003 Particle-turbulence interactions in atmospheric clouds. *Annu. Rev. Fluid Mech.* **35** (1), 183–227.

[3] BODENSCHATZ, E, MALINOWSKI, S. P, SHAW, R. A & STRATMANN, F 2010 Can we understand clouds without turbulence? *Science* **327** (5968), 970–971.

[4] DEVENISH, B. J, BARTELLO, P, BRENGUIER, J. L, COLLINS, L. R, GRABOWSKI, W. W, IJZERMANS, R. H, MALINOWSKI, S. P, REEKS, M. W, VASSILICOS, J. C, WANG, L. P & WARHAFT, Z 2012 Droplet growth in warm turbulent clouds. *Quarterly Journal of the Royal Meteorological Society* **138** (667), 1401–1429.

[5] REIGADA, R, HILLARY, R. M, BEES, M. A, SANCHO, J. M & SAGUÉS, F 2003 Plankton blooms induced by turbulent flows. *Proceedings of the Royal Society B: Biological Sciences* **270** (1517), 875–880.

[6] DENNY, M. W & GAYLORD, B 2010 Marine Ecomechanics. *Annual Review of Marine Science* **2**, 89–114.

[7] FALKOVICH, G, GAWEDZKI, K & VERGASSOLA, M 2001 Particles and fields in fluid turbulence. *Reviews of Modern Physics* **73** (4), 913–975.

[8] PUMIR, A & WILKINSON, M 2016 Collisional aggregation due to turbulence. *Annual Review of Condensed Matter Physics* **7**, 141–170.

[9] SUNDARAM, S & COLLINS, L. R 1997 Collision statistics in an isotropic particle-laden turbulent suspension. *J. Fluid. Mech.* **335**, 75–109.

[10] READE, W. C & COLLINS, L. R 2000 Effect of preferential concentration on turbulent collision rates. *Physics of Fluids* **12**, 2530–2540.

[11] BEC, J, CELANI, A, CENCINI, M & MUSACCHIO, S 2005 Clustering and collisions of heavy particles in random smooth flows. *Physics of Fluids (1994-present)* **17** (7), 073301.

[12] FALKOVICH, G, MUSACCHIO, S, PITERBARG, L & VUCELJA, M 2007 Inertial particles driven by a telegraph noise. *Physical Review E* **76** (2), 026313.

[13] GUSTAVSSON, K, MENEGUZ, E, REEKS, M & MEHLIG, B 2012 Inertial-particle dynamics in turbulent flows: Caustics, concentration fluctuations and random uncorrelated motion. *New Journal of Physics* **14** (11), 115017.

[14] KIØORBOE, T 2001 Formation and fate of marine snow: Small-scale processes with large-scale implications. *Scientia Marina* **65** (S2), 57–71.

[15] MAXEY, M. R 1987 The gravitational settling of aerosol particles in homogeneous turbulence and random flow fields. *Journal of Fluid Mechanics* **174**, 441–465.

[16] SQUIRES, K. D & EATON, J. K 1991 Preferential concentration of particles by turbulence. *Physics of Fluids A* **3**, 1169–1178.

[17] GUSTAVSSON, K & MEHLIG, B 2016 Statistical models for spatial patterns of heavy particles in turbulence. *Advances in Physics* **65** (1), 1–57.

[18] OTT, E 2002 *Chaos in dynamical systems, 2nd edition*. Cambridge, UK: Cambridge Univeristy Press.

[19] CVITANOVIC, P, ARTUSO, R, MAINIERI, R, TANNER, G, VATTAY, G, WHELAN, N & WIRZBA, A 2005 Chaos: classical and quantum. *ChaosBook. org (Niels Bohr Institute, Copenhagen 2005)* **69**.

[20] CENCINI, M, CECCONI, F & VULPIANI, A 2010 *Chaos: From simple models to Complex Systems*. World Scientific.

[21] WILKINSON, M & MEHLIG, B 2005 Caustics in turbulent aerosols. *Europhysics Letters* **71** (2), 186–192.

[22] WILKINSON, M, MEHLIG, B & BEZUGLYY, V 2006 Caustic activation of rain showers. *Physical Review Letters* **97** (4), 048501.

[23] GUSTAVSSON, K & MEHLIG, B 2011 Distribution of relative velocities in turbulent aerosols. *Physical Review E* **84** (4), 045304.

[24] GUSTAVSSON, K & MEHLIG, B 2014 Relative velocities of inertial particles in turbulent aerosols. *Journal of Turbulence* **15** (1), 34–69.

[25] BERRY, M. V & UPSTILL, C 1980 Catastrophe optics: Morphologies of caustics and their diffraction patterns. *Progress in Optics* **18**, 257–346.

[26] KIM, S & KARRILA, S. J 1991 *Microhydrodynamics: principles and selected applications*. Boston: Butterworth-Heinemann.

[27] HAPPEL, J & BRENNER, H 1983 *Low Reynolds Number Hydrodynamics*. Kluwer Academic Publishers Group.

[28] CHUN, J, KOCH, D. L, RANI, S. L, AHLUWALIA, A & COLLINS, L. R 2005 Clustering of aerosol particles in isotropic turbulence. *Journal of Fluid Mechanics* **536**, 219–251.

[29] BEC, J, BIFERALE, L, BOFFETTA, G, CENCINI, M, MUSACCHIO, S & TOSCHI, F 2006 Lyapunov exponents of heavy particles in turbulence. *Physics of Fluids* **18** (9), 091702.

[30] BEC, J, BIFERALE, L, CENCINI, M, LANOTTE, A, MUSACCHIO, S & TOSCHI, F 2007 Heavy particle concentration in turbulence at dissipative and inertial scales. *Physical Review Letters* **98** (8), 084502.

[31] CALZAVARINI, E, CENCINI, M, LOHSE, D & TOSCHI, F 2008 Quantifying turbulence-induced segregation of inertial particles. *Physical Review Letters* **101** (8), 084504.

[32] SAW, E. W, SALAZAR, J. P, COLLINS, L. R & SHAW, R. A 2012 Spatial clustering of polydisperse inertial particles in turbulence: I. Comparing simulation with theory. *New Journal of Physics* **14** (10), 105030.

[33] PAN, L, PADOAN, P & SCALO, J 2014 Turbulence induced relative velocity of dust particles II: the bidisperse case. *Astrophysical Journal* **791**, 48.

[34] PAN, L, PADOAN, P & SCALO, J 2014 Turbulence-Induced Relative Velocity of Dust Particles III: The Probability Distribution. *Astrophysical Journal* **792**, 69.

[35] ISHIHARA, T, KOBAYASHI, N, ENOHATA, K, UMEMURA, M & SHIRAISHI, K 2018 Dust Coagulation Regulated by Turbulent Clustering in Protoplanetary Disks. *The Astrophysical Journal* **854** (2), 81.

[36] BHATNAGAR, A, GUSTAVSSON, K & MITRA, D 2018 Statistics of the relative velocity of particles in turbulent flows: Monodisperse particles. *Physical Review E* **97** (2), 23105.

[37] BHATNAGAR, A, GUSTAVSSON, K, MEHLIG, B & MITRA, D 2018 Relative velocities in bidisperse turbulent aerosols: Simulations and theory. *Physical Review E* **98** (6), 63107.

[38] WOOD, A. M, HWANG, W & EATON, J. K 2005 Preferential concentration of particles in homogeneous and isotropic turbulence. *International Journal of Multiphase Flow* **31** (10-11), 1220–1230.

[39] SAW, E. W, SHAW, R. A, AYYALASOMAYAJULA, S, CHUANG, P. Y & GYLFASON, Á 2008 Inertial clustering of particles in high-reynolds-number turbulence. *Physical Review Letters* **100** (21), 214501.

[40] SALAZAR, J. P, DE JONG, J, CAO, L, WOODWARD, S. H, MENG, H & COLLINS, L. R 2008 Experimental and numerical investigation of inertial particle clustering in isotropic turbulence. *Journal of Fluid Mechanics* **600**, 245–256.

[41] BEWLEY, G. P, SAW, E. W & BODENSCHATZ, E 2013 Observation of the sling effect. *New Journal of Physics* **15** (8), 083051.

[42] SAW, E. W, SHAW, R. A, SALAZAR, J. P & COLLINS, L. R 2012 Spatial clustering of polydisperse inertial particles in turbulence: II. Comparing simulation with experiment. *New Journal of Physics* **14** (10), 105031.

[43] SAW, E. W, BEWLEY, G. P, BODENSCHATZ, E, SANKAR RAY, S & BEC, J 2014 Extreme fluctuations of the relative velocities between droplets in turbulent airflow. *Physics of Fluids* **26** (11), 111702.

[44] YAVUZ, M. A, KUNNEN, R. P, VAN HEIJST, G. J & CLERCX, H. J 2018 Extreme Small-Scale Clustering of Droplets in Turbulence Driven by Hydrodynamic Interactions. *Physical Review Letters* **120** (24), 244504.

[45] DOU, Z, BRAGG, A. D, HAMMOND, A. L, LIANG, Z, COLLINS, L. R & MENG, H 2018 Effects of Reynolds number and Stokes number on particle-pair relative velocity in isotropic turbulence: A systematic experimental study. *Journal of Fluid Mechanics* **839**, 271–292.

[46] TENNEKES, H, LUMLEY, J. L, LUMLEY, J. L & OTHERS 1972 *A first course in turbulence*. MIT press.

[47] FRISCH, U 1997 *Turbulence*. Cambridge, UK: Cambridge University Press.

[48] POPE, S. B 2000 *Turbulent flows*. Cambridge, UK: Cambridge University press.

[49] KOLMOGOROV, A. N 1941 The local structure of turbulence in incompressible viscous fluid for very large Reynolds numbers. *Doklady Akademii Nauk Sssr* **30** (4), 299–303.

[50] BATCHELOR, G. K 1959 Small-scale variation of convected quantities like temperature in turbulent fluid Part 1. General discussion and the case of small conductivity. *Journal of Fluid Mechanics* **5** (1), 113–133.

[51] ELGHOBASHI, S 1994 On predicting particle-laden turbulent flows. *Applied Scientific Research* **52** (4), 309–329.

[52] VAN KAMPEN, N 2007 Stochastic Processes in Physics and Chemistry. In *Stochastic Processes in Physics and Chemistry*. Elsevier.

[53] SOMMERER, J. C & OTT, E 1993 Particles floating on a moving fluid: A dynamically comprehensible physical fractal. *Science* **259** (5093), 335–339.

[54] PITERBARG, L 2001 The top Lyapunov exponent for a stochastic flow modeling the upper ocean turbulence. *SIAM J. Appl. Math.* **62**, 777–800.

[55] CARDY, J, FALKOVICH, G & GAWEDZKI, K 2008 *Non-equilibrium statistical mechanics and turbulence*. Cambridge University Press.

[56] GUSTAVSSON, K 2009 Advective collisions in random flows. Licentiate thesis, University of Gothenburg.

[57] PERGOLIZZI, B 2012 PhD thesis. *Université de Nice-Sophia Antipolis* .

[58] KRAICHNAN, R. H 1974 Convection of a passive scalar by a quasi-uniform random straining field. *Journal of Fluid Mechanics* **64** (4), 737–762.

[59] BEC, J 2005 Multifractal concentrations of inertial particles in smooth random flows. *J. Fluid Mech.* **528**, 255–277.

[60] BALKOVSKY, E & FOUXON, A 1999 Universal long-time properties of Lagrangian statistics in the Batchelor regime and their application to the passive scalar problem. *Phys. Rev. E* **60**, 4164–4174.

[61] OSELEDETS, V. I 1968 A multiplicative ergodic theorem. Characteristic Ljapunov, exponents of dynamical systems. *Trudy Moskovskogo Matematicheskogo Obshchestva* **19**, 179–210.

[62] RUELLE, D 1979 Ergodic theory of differentiable dynamical systems. *Publications Mathématiques de l'Institut des Hautes Études Scientifiques* **50** (1), 27–58.

[63] GOLDHIRSCH, I, SULEM, P. L & ORSZAG, S. A 1987 Stability and Lyapunov stability of dynamical systems: A differential approach and a numerical method. *Physica D: Nonlinear Phenomena* **27** (3), 311–337.

[64] GARDINER, C. W 2009 *Handbook of Stochastic Methods: For the Natural and Social Sciences.* Springer.

[65] RENYI, A 1970 Probability Theory. *Kiado, Budapest* .

[66] GRASSBERGER, P & PROCACCIA, I 1983 Generalized dimensions of strange attractors. *Physical Review Letters* **97A**, 227–230.

[67] HENTSCHEL, H. G. E & PROCACCIA, I 1983 The infinite number of generalized dimensions of fractals and strange attractors. *Physica D: Nonlinear Phenomena* **8** (3), 435–444.

[68] BENZI, R, PALADIN, G, PARISI, G & VULPIANI, A 1984 On the multifractal nature of fully developed turbulence and chaotic systems. *Journal of Physics A: General Physics* **17** (18), 3521.

[69] GRASSBERGER, P & PROCACCIA, I 1983 Characterization of strange attractors. *Physical Review Letters* **50** (5), 346.

[70] BEC, J, GAWEDZKI, K & HORVAI, P 2004 Multifractal clustering in compressible flows. *Physical Review Letters* **92** (22), 224501.

[71] HARTE, D 2001 *Multifractals: theory and applications.* Chapman and Hall/CRC.

[72] BECK, C 1990 Upper and lower bounds on the Renyi dimensions and the uniformity of multifractals. *Physica D: Nonlinear Phenomena* **41** (1), 67–78.

[73] Kristian Gustavsson knows what I am talking about.

[74] WILKINSON, M, MEHLIG, B & GUSTAVSSON, K 2010 Correlation dimension of inertial particles in random flows. *EPL* **89** (5), 50002.

[75] GUSTAVSSON, K, MEHLIG, B & WILKINSON, M 2015 Analysis of the correlation dimension of inertial particles. *Phys. Fluids* **27** (7), 073305.

[76] DEUTSCH, J. M 1985 Aggregation-disorder transition induced by fluctuating random forces. *Journal of Physics A: General Physics* **18** (9), 1449.

[77] WILKINSON, M & MEHLIG, B 2003 Path coalescence transition and its applications. *Physical Review E* **68** (4), 040101.

[78] MEHLIG, B & WILKINSON, M 2004 Coagulation by random velocity fields as a Kramers problem. *Physical Review Letters* **92** (25), 250602.

[79] DUNCAN, K, MEHLIG, B, ÖSTLUND, S & WILKINSON, M 2005 Clustering in mixing flows. *Physical Review Letters* **95**.

[80] GUSTAVSSON, K & MEHLIG, B 2011 Ergodic and non-ergodic clustering of inertial particles. *EPL* **96** (6), 60012.

[81] GUSTAVSSON, K 2019 I received the data for this plot from Kristian Gustavsson .

[82] FOUXON, I & HORVAI, P 2007 Fluctuation relation and pairing rule for Lyapunov exponents of inertial particles in turbulence. *Journal of Statistical Mechanics: Theory and Experiment* **2007** (08), L08002.

[83] ELLIS, R. S 2007 *Entropy, large deviations, and statistical mechanics.* Springer.

[84] DEN HOLLANDER, F 2008 *Large deviations.* American Mathematical Soc.

[85] TOUCHETTE, H 2009 The large deviation approach to statistical mechanics. *Physics Reports* **478** (1), 1–69.

[86] BALKOVSKY, E, FALKOVICH, G & FOUXON, A 2001 Intermittent distribution of inertial particles in turbulent flows. *Physical Review Letters* **86**, 2790–2793.

[87] BUCKLEW, J. A 1992 *Large Deviation Techniques in Decision, Simulation and Estimation.* Wiley.

[88] ELLIS, R. S 1984 Large Deviations for a General Class of Random Vectors. *The Annals of Probability* **12** (1), 1–12.

[89] SCHOMERUS, H & TITOV, M 2002 Statistics of finite-time Lyapunov exponents in a random time-dependent potential. *Physical Review E* **66** (6), 066207.

[90] HUBER, G, PRADAS, M, PUMIR, A & WILKINSON, M 2018 Persistent stability of a chaotic system. *Physica A: Statistical Mechanics and its Applications* **492**, 517–523.

[91] KAPLAN, J & YORKE, J 1979 Chaotic behavior of multi-dimensional difference equations. In *Functional differential equations and approximation of fixed points, Lectures notes in Mathematics, Springer-Verlag*, pp. 204–227. Springer.

[92] FREDERIKSON, P, KAPLAN, J. L, YORKE, E. D & YORKE, J. A 1983 The Liapunov dimension of strange attractors. *J. Diff. Eqns.* **49**, 183.

[93] LEDRAPPIER, F & YOUNG, L.-S 1988 Dimension Formula for Random Transformations. *Commun. Math. Phys* **117**, 529–548.

[94] FALKOVICH, G, FOUXON, A & STEPANOV, M 2002 Acceleration of rain initiation by cloud turbulence. *Nature* **419**, 151.

[95] DEREVYANKO, S. A, FALKOVICH, G, TURITSYN, K & TURITSYN, S 2007 Lagrangian and Eulerian descriptions of inertial particles in random flows. *Journal of Turbulence* **8** (No. 16).

[96] KULKARNY, V. A & WHITE, B. S 1982 Focusing of waves in turbulent inhomogeneous media. *Physics of Fluids* **25** (10), 1770–1784.

[97] CHETRITE, R & TOUCHETTE, H 2015 Nonequilibrium Markov Processes Conditioned on Large Deviations. *Annales Henri Poincare* **16** (9), 2005–2057.

[98] TOUCHETTE, H 2018 Introduction to dynamical large deviations of Markov processes. *Physica A: Statistical Mechanics and its Applications* **504**, 5–19.

[99] MAJUMDAR, S. N 2007 Brownian functionals in physics and computer science. In *The Legacy Of Albert Einstein: A Collection of Essays in Celebration of the Year of Physics*, pp. 93–129. World Scientific.

[100] KAC, M 1949 On distributions of certain Wiener functionals. *Transactions of the American Mathematical Society* **65** (1), 1–13.

[101] EVANS, D. J, COHEN, E. G & MORRISS, G. P 1993 Probability of second law violations in shearing steady states. *Physical Review Letters* **71** (15), 2401.

[102] GALLAVOTTI, G & COHEN, E. G 1995 Dynamical ensembles in nonequilibrium statistical mechanics. *Physical Review Letters* **74** (14), 2694.

[103] KURCHAN, J 1998 Fluctuation theorem for stochastic dynamics. *Journal of Physics A: Mathematical and General* **31** (16), 3719.

[104] LEBOWITZ, J. L & SPOHN, H 1999 A Gallavotti-Cohen-type symmetry in the large deviation functional for stochastic dynamics. *Journal of Statistical Physics* **95** (1-2), 333–365.

[105] HARRIS, R. J & SCHÜTZ, G. M 2007 Fluctuation theorems for stochastic dynamics. *Journal of Statistical Mechanics: Theory and Experiment* **2007** (07), P07020.

[106] CHETRITE, R & GAWEDZKI, K 2008 Fluctuation relations for diffusion processes. *Communications in Mathematical Physics* **282** (2), 469–518.

[107] CHETRITE, R, FALKOVICH, G & GAWEDZKI, K 2008 Fluctuation relations in simple examples of non-equilibrium steady states. *Journal of Statistical Mechanics: Theory and Experiment* **2008** (08), P08005.

[108] SEIFERT, U 2012 Stochastic thermodynamics, fluctuation theorems and molecular machines. *Reports on Progress in Physics* **75** (12), 126001.

[109] WILKINSON, M, GUICHARDAZ, R, PRADAS, M & PUMIR, A 2015 Power-law distributions in noisy dynamical systems. *EPL* **111** (5), 50005.

[110] BENDER, C. M & ORSZAG, S. A 1978 *Advanced Mathematical Methods for Scientists and Engineers*. New York, USA: McGraw-Hill.

[111] ZINN-JUSTIN, J & JENTSCHURA, U. D 2004 Multi-instantons and exact results I: Conjectures, WKB expansions, and instanton interactions. *Annals of Physics* **313** (1), 197–267.

[112] DORIGONI, D 2014 An introduction to resurgence, trans-series and alien calculus. *arXiv preprint arXiv:1411.3585* .

[113] DUBEY, A, MEIBOHM, J, GUSTAVSSON, K & MEHLIG, B 2018 Fractal dimensions and trajectory crossings in correlated random walks. *Physical Review E* **98** (6), 062117.

[114] POSTON, T & STEWART, I 1978 *Catastrophe theory and its applications*. Pitman publishing.

[115] ARNOL'D, V. I 1984 *Catastrophe theory*. Springer.

[116] FALCONER, K 1990 Fractal Geometry: Mathematical Foundations and Applications. *The Mathematical Gazette* .

[117] HUNT, B. R & KALOSHIN, V. Y 1997 How projections affect the dimension spectrum of fractal measures. *Nonlinearity* .

[118] GUSTAVSSON, K & MEHLIG, B 2013 Distribution of velocity gradients and rate of caustic formation in turbulent aerosols at finite Kubo numbers. *Physical Review E* **87** (2), 023016.

[119] FALKOVICH, G & PUMIR, A 2007 Sling Effect in Collisions of Water Droplets in Turbulent Clouds. *J. Atmos. Sci.* **64**, 4497–4505.

[120] BERRY, M. V 1977 Focusing and twinkling: critical exponents from catastrophes in non-Gaussian random short waves. *Journal of Physics A: General Physics* **10** (12), 2061.

[121] RICE, S. O 1944 Mathematical analysis of random noise. *Bell System Technical Journal* **23** (3), 282–332.

[122] KAC, M 1948 On the average number of real roots of a random algebraic equation. *Proceedings of the London Mathematical Society* **2** (1), 390–408.

[123] HOWLETT, J, ABRAMOWITZ, M & STEGUN, I. A 1966 Handbook of Mathematical Functions. *The Mathematical Gazette* .

[124] GUSTAVSSON, K & MEHLIG, B 2013 Lyapunov Exponents for Particles Advected in Compressible Random Velocity Fields at Small and Large Kubo Numbers. *Journal of Statistical Physics* **153** (5), 813–827.

[125] MITRA, D 2019 Private communication .

[126] GIRIMAJI, S. S & POPE, S. B 1990 A diffusion model for velocity gradients in turbulence. *Physics of Fluids A* **2** (2), 242–256.

[127] TOUCHETTE, H & BECK, C 2006 Nonconcave entropies in multifractals and the thermodynamic formalism. *Journal of Statistical Physics* **125** (2), 455–471.

[128] FRISCH, U & PARISI, G 1980 On the singularity structure of fully developed turbulence. *New York Academy of Sciences, Annals* **357**, 359–367.

[129] DONSKER, M. D & VARADHAN, S. R. S 1983 Asymptotic evaluation of certain markov process expectations for large time. IV. *Communications on Pure and Applied Mathematics* **36** (2), 183–212.

[130] MEIBOHM, J, PISTONE, L, GUSTAVSSON, K & MEHLIG, B 2017 Relative velocities in bidisperse turbulent suspensions. *Physical Review E* **96** (6), 061102.

[131] MEIBOHM, J & MEHLIG, B 2019 Heavy particles in a persistent random flow with traps. *Phys. Rev. E* **100** (2), 23102.

[132] MEIBOHM, J, GUSTAVSSON, K, BEC, J & MEHLIG, B 2019 Fractal catastrophes. *arXiv:1905.08490* .

PART V

RESEARCH PAPERS

Paper A

https://doi.org/10.1103/PhysRevE.96.061102

Paper B

https://doi.org/10.1103/PhysRevE.100.023102

Paper C

https://arxiv.org/abs/1905.08490